MSc Thesis

Developing a double-wake vortex-panel method model capable of simulating dynamic stall with vortex generators for wind turbine design applications

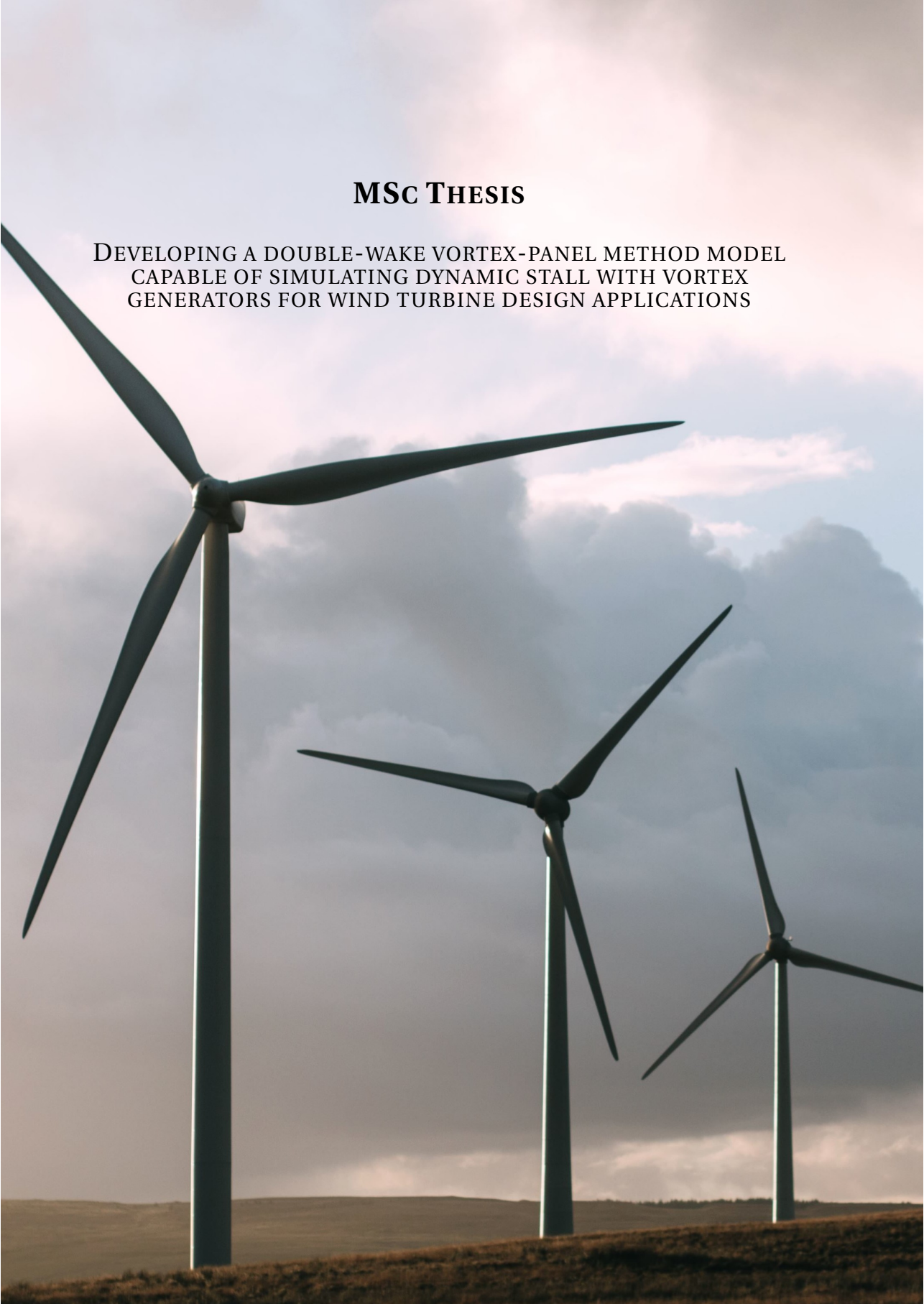

MSc Thesis

Developing a double-wake vortex-panel method model capable of simulating dynamic stall with vortex generators for wind turbine design applications

to obtain the degree of Master of Science in Aerospace Engineering at the Delft University of Technology, to be defended publicly on the 16th of September, 2022

by

Lukas Karolis Bajarūnas

This thesis has been approved by the

Promoter: prof. Dr. ir. Carlos Simão Ferreira
Co-promoter: prof. Dr. ir. Wei Yu

Composition of the promotion committee:

prof. Dr. ir. Carlos Simão Ferreira,	Delft University of Technology
prof. Dr. ir. Wei Yu,	Delft University of Technology
Independent members:	
prof. Dr. ir. Bas van Oudheusden,	Delft University of Technology

Keywords: Vortex Generators, Panel Method, Viscous-Inviscid Interaction, Dynamic Stall, Double Wake

ISBN 000-00-0000-000-0

An electronic version of this dissertation is available at
http://repository.tudelft.nl/.

ACKNOWLEDGEMENTS

The upcoming master's thesis is the culmination of all my effort to obtain my degree in Aerospace Engineering. This work encompasses numerous events in my life, remaining a constant in my life. While it has not always progressed quickly, I can't imagine how much harder the process would have been without the support I received.

I am incredibly grateful to Dr. Wei Yu for helping me navigate the entire time. Thank you for being so proactive and encouraging me to keep progressing; for always being available for our (bi-)weekly meetings, no matter what concerns I might have had. I am grateful for your patience, especially when I felt a loss in direction and struggled to progress for weeks. Your advice and effort have contributed significantly to the completeness of this work, and I will always appreciate it.

An equally heartfelt thank you to Dr. Carlos Simão Ferreira for always encouraging me to pursue my passion for this topic. I would not have had the courage to delve deeper into aerodynamics if it wasn't for your belief in my abilities. Your experience and insightful comments have made me reconsider my ideas and preconceptions on several occasions, yet built upon my knowledge every time. I would also like to thank you for being so understanding at the times when I struggled the most. Finally, above all, I am grateful for all the effort you have invested in me.

A special thanks to the people without whose work this thesis would not be possible. I want to express my great appreciation to Dr. Alessandro Zanon for the meetings we had in which you guided and advised me on navigating your code. It has been a fantastic opportunity to build upon your work and create something meaningful. I am also deeply thankful to Dr. Delphine De Tavernier, whose VG simulation model and experimental dataset were crucial for this work to reach its potential.

On a personal note, I want to thank the people in my life who have stuck with me throughout the process. My deepest and dearest thank you goes to my partner, the love of my life, Danielle Marie; thank you for being there for me every day as my number one supporter. I would like to express my sincere gratitude to my parents for giving me so many opportunities in my life; I would not be where I am today without the passion for the pursuit of knowledge you instilled in me. Many thanks to Diane and Chris for welcoming me into your family and home; I look back fondly on the time I spent with you. Finally, a thank you to the friends who were there for me during this time, especially those who helped proofread my drafts: Misa and my brother Kristupas.

Lastly, I want to thank everyone who helped me get this far in my academic career. Thank you to my teachers and professors, who spurred me to succeed in aerospace engineering. I am particularly grateful to the professors who gave me an opportunity to be a teaching assistant and whom I enjoyed teaching with throughout my master's degree.

SUMMARY

Vortex generators (VGs) are increasingly prominent in wind turbine applications for improving airfoil performance by limiting stall phenomena. With the increasing size of wind turbine blades, the loading from a dynamic stall is exceptionally influential on structural fatigue. While the design process often includes VGs at a later stage, a fast and efficient tool capable of simulating unsteady airfoils with VGs does not exist; this thesis focuses on developing such a tool.

Vortex-panel methods with strong viscous-inviscid coupling are the standard for a baseline airfoil design. For this purpose, many established programs exist, such as XFOIL; Such models output airfoil force coefficients and boundary layer (BL) variables by simulating an airfoil with a trailing-edge wake under steady conditions. Research in the field has expanded the breadth of applications for such models, with developments for unsteady conditions and better approximations of stalled conditions. A model developed by Zanon et al. [1] showed promise with increased model performance during a stall by adding a secondary wake-shedding location at the separation point. The model explicitly defines a separation location and works for steady and unsteady pitching cases.

VGs delay separation by introducing vortices perpendicular to the flow direction; these vortices increase the flow turbulence through the increased mixing. Within the BL variables, these changes manifest as a decrease in shape factor (H) and an increase in the coefficient of friction (C_f). Given the two-dimensional nature of vortex-panel methods, a direct method of simulating a VG through geometry is infeasible. Although several propositions for solving this conundrum exist (representation as a lateral force or vortex), Kerho and Kramer [2] achieved success through an artificial mixing source-term; The method chosen was VGFOIL[3], which adapted this formulation to create a semi-empirical term encompassing variable VG properties.

In order to assess the base model's viability for simulating dynamic stalls in airfoils, the model underwent a validation process for a NACA0015 airfoil. The need to adapt and update the code for future compatibility further necessitates the double-wake model validation. The inviscid and single-wake modules are in working order, and the double-wake steady lift coefficient shows good parity with the experimental data, improving over XFOIL. The unsteady simulation proved able to match the sharp drop in lift upon a reversal in direction, with less accuracy in a separated flow during the reattachment phase. The simulation timestep proved to be a critical input variable affecting the final result and its noise; an investigation defined the optimal timestep length as a product of the Reynolds Number and average panel length.

Evaluating the final model's performance requires data for an airfoil in clean and VG configurations; a recent dataset published by Tavernier et al.[4] spans variable inflow speed,

pitching unsteadiness, and VG dimensions and positions. The initial validation for the airfoil seeks to establish the baseline performance of the model for a clean configuration. The steady results indicated the double-wake model's shortcomings within the stall region and a decreased accuracy when forcing a leading edge transition. The model found good parity in the unsteady case, with disparities in lift slope and reattachment. Lower pitching unsteadiness and Reynolds number corresponded to increased performance, contrary to a forced transition case. A further timestep analysis pointed to the separation point movement as the source of the lift noise, significantly more present in the DU17DBD25 airfoil due to its thickness. The analysis affirmed the previously obtained relation for optimal timestep, and filtering achieved reduced noise.

Simulating VGs under dynamic stall conditions requires integrating the VG modeling methods into the double-wake model. As VGFOIL built upon XFOIL, the relative changes were isolated and extracted as the VG module. These changes consisted of adding an exponential mixing term to the equilibrium shear stress function at the VG location, with its magnitude derived from the BL variables and VG dimensions. Verification of the implementation confirmed expected changes in the BL variables.

Repeating simulations for the previous flow cases, for configurations including VGs, provided the necessary results to evaluate the model's viability; the evaluation considers the relative impact of the VG to account for inherent errors in the base double-wake model. The steady results captured the expected separation delay and an increase in maximum lift coefficient; however, the model consistently overpredicted these values across all VG configurations. The model's accuracy is similar to VGFOIL, significantly improving when the VG-induced mixing magnitude is lower. Throughout the unsteady results, the model accurately predicts the separation prevention qualities of VGs beyond the clean stall angle. The relative changes are generally consistent with those seen in the experimental data. These results prove that the model can simulate the relative changes in airfoil performance, despite the errors. The model's performance correlates heavily with the source-term magnitude, a critical value in predicting separation. In order to improve the model's performance and breadth of applicability, further research on the topic should consider source-term calibration for the double-wake model, quasi-steady BL formulation, VG-induced transition, and improved methods of calculating drag.

CONTENTS

1

INTRODUCTION

While wind turbines have been around for centuries, applied by humans to harness the energy of the wind, it was not until recently that their performance allowed for calculation through aerodynamic modeling. As the methods of simulation improved, so did the methods of wind turbine design. The increased capacity for new designs allowed for rotors with ever-increasing power coefficients, corresponding to higher energy outputs and efficiency. While changes in the rotor design and variable speed allow for maintaining optimal operating conditions, this increase in efficiency has primarily resulted from the growth of the swept area of the wind turbine [5]. The increased swept area means the turbine blades, which can now be over a hundred meters long, have been getting very large and heavy. As a result, the unsteady effects of the incoming wind have become highly impactful in terms of ultimate load and, more importantly, fatigue. Another way to increase the power coefficient is to operate at consistent higher wind speeds near the design point, another factor incentivizing offshore wind turbine development; in order to harness the more optimal operating conditions. Developments in the infrastructure for wind turbines and improvements in the measurements of wind speeds have facilitated the move offshore. While these higher wind speeds allow for much better power generation, they have also resulted in a compounded increase in loading and unsteadiness of the wind conditions. The increase in average wind speed and gusts is evident when comparing the data of an inland[6] measurement site to one slightly off the coast[7]. Within the same geographical region, the gusts experienced by the offshore site have been more frequent and higher in amplitude.

While these effects are an unavoidable consequence of the aforementioned developments in the field, the design process requires the consideration of their influence during the design phase. Separation is a significant inhibitor to wind turbine performance in terms of aerodynamic performance. As wind turbines continue increasing in size, so does the slenderness of the blade, while the attachment at the root section must retain its strength to withstand the ever-increasing loads. The blade must have a given cross-sectional area along its span to counteract the aerodynamic and centrifugal forces. As the thickness

increases to match the requirement for structural capability, the thickness to chord ratio increases proportionally. As a result, flow over the wind turbine blade is much more prone to separation. Engineers strive to limit this effect by applying active and passive devices acting as the separation control mechanism. This thesis will investigate the application of vortex generators on wind turbines.

While vortex generators by themselves have been a subject of study since the first proposal by Taylor in 1946 [8], the models created have mainly been in a steady flow. A rotating wind turbine blade potentially experiences substantial variation in the angle of attack over a single rotation due to the direction of the wind, with a non-negligible unsteadiness. A wind turbine would likely experience a dynamic stall within such a flow regime[9]; a dynamic stall occurs due to an accumulation of a vortex over an airfoil in a pitch-up motion causing increased lift and drag, which, when shed, causes a much more significant loss of lift than could be seen in a steady flow [10]. Kramer [11] first mentions the existence of such a phenomenon in 1932, but no further investigation followed due to a seeming lack of application for airfoils of that period. Carr et al. [12] analyzed an airfoil in a dynamic stall and found it begins with a flow reversal at the trailing edge. This reversal travels up the airfoil, eventually reaching the leading edge, causing a vortex of immense magnitude to shed, resulting in temporarily increased lift and drag followed by a subsequent drop in the lift up to flow reattachment. The periodic loading as a result of dynamic stall results in an increase of fatigue on wind turbine blades and reduces their lifespan [13]. With wind energy moving offshore, the development of new wind farms occurs with wind turbines constructed in ever larger grids. A study by Choudhry et al. [14] found that a dynamic stall occurred more often in wind turbines experiencing a flow of increased turbulence, leading to the conclusion that wind turbines in the middle of a wind farm are increasingly susceptible to increased periodic loading and thereby fatigue damage.

The development of vortex generator design occurs through simulation and testing on blades and blade sections. Especially in the early design phase, the process must examine the changes by simulating the outcome of every design. It would be infeasible to run extensive simulations for every setup at this design stage, as it would take too much time. Therefore, optimal vortex generator design in wind turbine blades requires a faster and more efficient tool. This tool must also consider all the phenomena the blade experiences without significant simplifications. The basis of the model will be a strong viscous-inviscid interaction double-wake panel model, which yields accurate results in stalled flow with considerably less resource usage.

1.1. THESIS OBJECTIVE

At this level of fidelity, a model that includes the phenomena of dynamic stall and vortex generators does not exist, and its development will be the aim of this work. While independent viscous-inviscid models already exist for simulating airfoils with vortex generators and simulating dynamic stall on an unsteady pitching airfoil, combining these models could provide some challenges. This thesis defines the main focus as:

> to capture the flow changes from the vortex generators in unsteady flow and integrate it with a double-wake panel model, yielding a robust and efficient

tool for use in wind turbine design that is capable of capturing dynamic stall phenomena and their prevention through vortex generators

In order to achieve this goal, the thesis is divided into several research objectives.

1. **State of the art in dynamic stall and VG modeling** Understanding the process of developing a model that includes both effects requires dissecting existing models of each purpose individually so that the intricacies of each can be understood. This objective yields the following research questions about this work's aim.
   - *What effects do vortex generators have on the flow, and how are they modeled in current tools?*
   - *How do vortex generators behave in unsteady flow?*
   - *How do current viscous-inviscid models take a dynamic stall into account?*
   - *Is there any experimental data for such cases that allows for model validation?*
2. **Implementation of flow changes due to vortex generators in a viscous-inviscid double-wake model** With an existing model capable of simulating dynamic stall, adding vortex generators by adapting integral boundary-layer relations achieves a model that accounts for their effect.
   - *What is the required change in the relations to include vortex generators?*
   - *Can the model effectively capture the unsteady behavior of vortex generators in a dynamic stall?*
   - *Do the results of the simulation from the code correspond to reality*
3. **Application of the code to investigate the performance of VGs on wind turbines** As this work aims to create a tool that would set a new standard for wind turbine blade simulation, the code must be usable, easy to read, and stable. The code will be applied to simulate a few cases to examine the influence of VGs on performance. These requirements of the code yield the following questions:
   - *What is the code's behavior with changes in spatial and temporal discretization?*
   - *Can the program be made into a tool for use by itself?*
   - *Can the program yield insights into VG performance on airfoils?*

1.2. RESEARCH APPROACH AND METHODOLOGY

The main aim of the research is to develop a model which can give results closely matching experimental data of an airfoil with vortex generators in a dynamic stall. This work builds upon existing models and concepts to unify the different modeling approaches into a single program. This program should be sufficiently understandable for use by other parties. The work is split into discrete stages to simplify this complicated process.

Understanding the approach for developing this tool begins with a literature review of the related topics; adding vortex generators to a viscous-inviscid interaction model requires

investigating them separately.

A strong viscous-inviscid interaction vortex-panel method fulfills the objective of creating a fast and accurate tool for airfoil simulation for design. Chapter 2 will examine the theory behind such models, delving into the inviscid and viscous aerodynamic formulations and their interaction. The chapter expands upon the existing formulation by introducing the concept of a secondary wake at the separation location, accompanied by a discussion of applicability. The purpose of the chapter is to provide the reader with the necessary background information, which forms the base of the final program.

While many devices can prevent or delay dynamic stall, the thesis will focus solely on vortex generators. Chapter 3 will introduce the breadth of vortex generator applications and their history to justify the need for their simulation. Furthermore, the chapter will examine the theory behind their effectiveness, examining the impact of the vortex generator on the boundary layer and its effect on separation delay. A summary of existing methods of modeling vortex generators will follow, with a brief analysis of the merits of each one.

First, the underlying viscous-inviscid interaction model must undergo verification and validation. In order to do this, the verification process begins by considering the governing equations and their underlying assumptions. Comparing the results obtained from this model to previously validated models allows for verifying the expected output. The model's validation occurs by comparing the parity of the simulation results to experimental data, with a detailed elaboration of the errors and their source. The initial validation of the model will be performed in Chapter 4 for a clean NACA0015 airfoil, an airfoil that the model previously simulated sufficiently well. The initial validation aims to investigate the variables affecting simulation error and establish the baseline performance of the model. As this project will repurpose an existing model, ensuring that it functions accurately for its new breadth of application is essential.

Given that the model forms its basis on existing theory, the results are obtained for increasing complexity in formulation, starting from its inviscid formulation. Validating each part of the model is achieved by comparing the simulation results to experimental results and the results of other models. While the ability to simulate the unsteady phenomena of a dynamic stall is the reason for using a double-wake model, it must also yield good results for steady conditions. The experimental data for this section must be measurements for the same airfoil in steady and unsteady conditions, for the same flow conditions, as this allows for the most straightforward comparison of the two.

Upon obtaining experimental data for an airfoil with vortex generators, a second validation proceeds for the new airfoil to evaluate the model's ability to simulate the airfoil without vortex generators in Chapter 5.

The robustness of the code will be tested for varying inputs throughout the process, given the importance of the code's stability when performing time-dependent simulations. As such, for both validations, an investigation into the code's performance for varying airfoil panel size and timestep will be undertaken. This sensitivity analysis ensures optimal code functionality and establishes a standardization that facilitates the comparison of results when simulating configurations with vortex generators.

With a validated double-wake viscous-inviscid interaction model, the implementation of the effects of VGs will proceed in Chapter 6 based on the VG modeling methods discussed in the literature study. Given the unsteady nature of dynamic flow phenomena, the unsteady phenomena of VGs must be considered. Implementing VG functionality in the double-wake model requires choosing an existing modeling method to represent the VG term in the governing equations. If the validation cases prove an unsteady formulation necessary, such an amendment must follow in the model. As the work aims to create a design tool, the program must be able to model the effects of changing dimensions of the VG.

In order to verify the resultant model, the simulation results for a simple case must be compared to the original VG implementation for the single-wake model. Physical experiments with vortex generators characterize them in terms of physical dimensions of length. As the model does not necessarily rely on the physical presence of the VG to disturb the flow at the location of the VG, the model must contain a relation between the VG dimensions and this flow disturbance. This relation ensures that simulated cases are identical and are valid for comparison. Verifying the implementation of VG functionality to the model follows similar reasoning as validating the model for an airfoil. While the double-wake and single-wake VG models need to be valid individually, verifying the boundary layer variables is sufficient upon implementing the VG module to the double-wake model. Confirming expected changes is sufficient to ensure the validity of implementation.

After vortex generator functionality implementation to a baseline validated model, the result is a model that can produce airflow results around an airfoil with given flow conditions and VG configurations. The model should be capable of predicting a dynamic stall and its prevention through vortex generators. The evaluation of the VG double-wake model is found in Chapter 7, with an analysis of results for identical cases as the clean configuration validation. Choosing identical flow cases highlights the errors present in the base formulation, allowing the final evaluation to account for these errors in the airfoil results with VGs. Lastly, this evaluation is performed for a broad range of vortex generator configurations, granting a broad look into the design capabilities of the program.

Experimental data with an airfoil in steady/unsteady stalled conditions allows for an evaluation of the model's overall performance. In order to compare physical flow with the simulations, a comparison has to be made objectively by evaluating the difference in key variables, such as the pressure coefficient distribution over the airfoil, the lift coefficient curve through a range of angles, and the separation prediction criteria. Except for the boundary layer variables, data for these values is commonly available, and due to its prevalence as a performance indicator, it is also possible to evaluate the current model's success compared to other existing models.

While designing a new airfoil is beyond the scope of this thesis, the resulting model should allow achieving this. The program will take flow conditions as input and output the performance of the airfoil based on the given VG setup. As the model can find an optimal VG setup for each flow case, generalizations can proceed from these results, taking the form of trends and relations between the different variables and lengths of

the VG setup. Obtaining conclusions about the VG design can also be compared against existing guidelines, which can either be confirmed or denied based on these results. The significance of the findings would result in increased efficiency in airfoil performance due to a more optimized VG design.

2

VISCOUS-INVISCID AIRFOIL MODEL

Understanding the process of flow has historically been undertaken through experimentation. The processes involved with experimentation are both expensive in resources and time. In the design of airfoils, these costs can be a significant barrier to the number of parameters tested and design iterations performed. Other ways of calculating this flow must be investigated to examine a wider berth of design combinations. A numerical solution to this problem proves to be a quick and effective alternative to physical experimentation, facilitating the process of airfoil design and preliminary calculations.

Existing methods of numerical flow solutions take one of two existing approaches: a full Reynolds-Averaged Navier-Stokes (RANS) solution or a viscous-inviscid interaction approach. While more expensive models such as DNS and LES exist, these are much too computationally expensive to consider for design applications. Solving the Navier-Stokes equations can also be very demanding, depending on the flow conditions, limiting its application to design tools. The calculation of unsteady processes encountered means that a very fine mesh could be required leading to higher costs of solving the problem.

As this project aims to develop a tool that can simulate an airfoil in a dynamic stall with vortex generators, a robust model is required. Given that the goal is to apply the findings in the field of wind turbine design, the model's ability to run quickly and accurately is vital. For this purpose, a viscous-inviscid interaction model is the chosen model.

The aerodynamic model is designed to compute the airfoil's velocity field and the resulting pressure on its surface. By achieving these, the user can extract the forces acting on the airfoil and extrapolate the findings to the design phase. The Navier-Stokes equations govern aerodynamic physics, and the solution of these yields the desired results. In the two-dimensional case, these equations consist of the mass continuity and momentum in the x- and y-directions.

Due to the complexity and non-linearity of these equations, solving them can take a tremendous amount of time and would not be desirable for quick computation. Several

simplifications and assumptions increase the speed of such a solution. While the flow near the airfoil is affected by the body and requires extensive computation, flow further away is not affected as much and allows for several simplifications to the continuity equations. The incompressibility assumption ignores the density in differential form while assuming the viscosity effects to be negligible in the flows of regions further away from the airfoil. An inviscid formulation also excludes the effects of the boundary layer forces on the flow field. These simplifications create a set of equations that are much less computationally expensive and can be solved quickly. The equations below are the simplified Navier-Stokes equation applicable to the outer flow. Removing the external body forces and viscosity effects leads to the equations below, with u and v representing the velocities of the flow in the x- and y-direction, respectively.

$$\text{Continuity equation:} \quad \frac{\partial(u)}{\partial x} + \frac{\partial(v)}{\partial y} = 0 \tag{2.1}$$

$$\text{Momentum in x-direction:} \quad \frac{\partial(u)}{\partial t} + u\frac{\partial(u)}{\partial x} + v\frac{\partial(u)}{\partial y} = -\frac{1}{\rho}\frac{\partial p}{\partial x} \tag{2.2}$$

$$\text{Momentum in y-direction:} \quad \frac{\partial(v)}{\partial t} + u\frac{\partial(v)}{\partial x} + v\frac{\partial(v)}{\partial y} = -\frac{1}{\rho}\frac{\partial p}{\partial x} \tag{2.3}$$

While this allows for the solution of the outer flow, the model must still consider the airfoil's body effects. The boundary layer, a region of flow where the velocity is affected by the airfoil surface, is calculated using the integral boundary-layer equations. The flow in the boundary layer consists of the laminar region at the leading edge, progressing into a turbulent flow as the instability of the flow grows as the fluid moves along the airfoil. The model includes the boundary layer effect through a Neumann boundary condition in the inviscid solver at the airfoil's surface. In the boundary layer, one cannot make the same assumptions as before, and the viscous effects and body forces must be included. The equations dictating the flow in the thin boundary-layer can be found in Section 2.2. This method is valid, as the boundary layer over the airfoil and the wake is sufficiently thin; however, this work focuses on modeling dynamic stall effects in unsteady flow. This condition is no longer valid in such a case, and Subsection 2.1.2 introduces the method to account for this disparity.

The velocity field, $\vec{u}_e$, can be taken as the contribution of the far stream velocity, the inviscid solution, and the viscous correction in that order. Thus the model defines this velocity field as:

$$\mathbf{q_e}(\vec{x};t) = \mathbf{q}_\infty(t) + \mathbf{q}_i(\vec{x};t) + \mathbf{q}_v(\vec{x};t) \tag{2.4}$$

2.1. INVISCID FLOW

In order to solve the inviscid flow, the vortex-panel method adapts the solution by including a secondary wake at the separation location. This solution approach assumes that this outer region is unaffected by the airfoil itself. As stated earlier, this consists of

excluding the viscosity's effects; the governing Navier-Stokes equations can thus exclude the resultant forces. The solution method used for the flow outside the airfoil's influence is taken from Katz and Plotkin [15], with inviscid, incompressible, and irrotational flow assumptions. These flow characteristics mean that the flow is governed only by the continuity equation and irrotationality requirement. The principle of a vortex-panel method is achieving a coherent flow field from an airfoil geometry through the superposition of numerous elementary solutions using Green's identity. The output of each elementary solution is a flow field resulting from that point. Therefore, splitting up the airfoil into panels allows for increasing detail in the solution with each additional panel. The velocity at an arbitrary point p is the sum of the velocities induced by every elementary solution.

Within a panel method, the elementary solutions used are: a source and vortex located at each panel, a vortex in the boundary layer portion of the near wake, and vortex points shed in the far wake. The boundary condition of flow speed normal to the airfoil's surface dictates the source term's strength and vorticity at each airfoil panel.

2.1.1. ELEMENTARY FLOW SOLUTIONS

The elementary flow defined in the wake is a vortex of strength Γ. This element only results in tangential flow, with the induced velocity defined as a function of the radial and angular position:

$$q_r = 0 \tag{2.5}$$

$$q_\theta = q_\theta(r,\theta) \tag{2.6}$$

Solving the guiding equations of the model requires integrating this elementary solution into the guiding equations. Equation 2.7 displays the amended continuity equation:

$$\frac{\partial q_r}{\partial r} + \frac{1}{r}\frac{\partial q_\theta}{\partial \theta} + \frac{q_r}{r} = 0 \tag{2.7}$$

From this equation, $\frac{\partial q_\theta}{\partial \theta} = 0$, and thus q_θ becomes a function of the radial distance, r, only. The condition for irrotational flow becomes:

$$\omega = -\frac{1}{2r}\left[\frac{\partial}{\partial r}\left(r q_\theta\right) - \frac{\partial}{\partial \theta}\left(q_r\right)\right] = 0 \tag{2.8}$$

Since, $q_r = 0$, it can be deduced that

$$\frac{\partial}{\partial r}\left(r q_\theta\right) = 0$$

.

This means that the tangential velocity is proportional to the reciprocal of the radial distance. In order to obtain the exact relation of velocity due to a vortex, the integral over

a constant radial position defines the total magnitude resulting from the vortex element. The circulation Γ is positive in the counterclockwise direction.

$$\Gamma = \oint \mathbf{q} \cdot d\mathbf{l} = \int_{2\pi}^{0} q_\theta \cdot r\, d\theta = 2\pi r q_\theta \tag{2.9}$$

Thus this elementary solution results in an induced velocity, at a distance r away, equal to:

$$q_r = 0 \tag{2.10}$$

$$q_\theta = \frac{\Gamma}{2\pi r} \tag{2.11}$$

The angle the vortex makes with an arbitrary point (x, y) dictates the direction of the resulting tangential velocity. Expressing this is in the more familiar Cartesian form, the equations can be reformulated for a vortex at position (x_0, y_0).

$$u = -\frac{\Gamma}{2\pi} \frac{y - y_0}{(y - y_0)^2 + (x - x_0)^2} \tag{2.12}$$

$$w = \frac{\Gamma}{2\pi} \frac{x - x_0}{(y - y_0)^2 + (x - x_0)^2} \tag{2.13}$$

One limitation of the current vortex description is the singularity that appears in the vortex center. As the distance is zero, the formula finds no result for the induced velocity. In order to overcome this singularity, the model assumes the vortex core to mimic the behavior of a real-life flow. This assumption manifests itself as a viscous core, where the viscous interaction limits the flow speed. This thesis will employ the Lamb ideal viscous vortex model. The vortex core size R_C is defined as proportional to the viscosity and time with $R_C \propto \sqrt{4\nu t}$. The relation is implemented into the previous two equations to yield the equation below, where $R = \sqrt{(x - x_0)^2 + (y - y_0)^2}$:

$$u = -\frac{\Gamma}{2\pi} \frac{y - y_0}{(y - y_0)^2 + (x - x_0)^2} \left(1 - e^{(-R^2/R_C^2)}\right) \tag{2.14}$$

$$w = \frac{\Gamma}{2\pi} \frac{x - x_0}{(y - y_0)^2 + (x - x_0)^2} \left(1 - e^{(-R^2/R_C^2)}\right) \tag{2.15}$$

DISTRIBUTED SOURCES AND VORTICES OVER A PANEL

While the previous section considered the resultant flow due to a point vortex, the panels that make up the airfoil's surface are lines that cannot reduce to a single point. Thus, each panel is assigned a midpoint at which a point vortex acts. The vorticity per unit length, γ, is distributed over the airfoil's surface; given the airfoil's discretization into panels, the

value is constant over a single panel. This assumption results in the following expression for the vorticity of a panel, where $(x_{k+1} - x_k)$ is the length of an arbitrary panel:

$$\Gamma = \gamma \times (x_{k+1} - x_k) \tag{2.16}$$

The velocity induced by a constant vorticity distribution can be expressed as:

$$u = -\frac{\gamma}{2\pi} \int_{x_k}^{x_{k+1}} \frac{y - y_0}{(x - x_0)^2 + (y - y_0)^2} dx \tag{2.17}$$

$$w = \frac{\gamma}{2\pi} \int_{x_k}^{x_{k+1}} \frac{x - x_0}{(x - x_0)^2 + (y - y_0)^2} dx \tag{2.18}$$

The influence of a source distribution over an airfoil is very similar, where a constant source distribution of strength σ will result in the following induced velocities:

$$u = \frac{\gamma}{2\pi} \int_{x_k}^{x_{k+1}} \frac{x - x_0}{(x - x_0)^2 + (y - y_0)^2} dx \tag{2.19}$$

$$w = \frac{\gamma}{2\pi} \int_{x_k}^{x_{k+1}} \frac{y - y_0}{(x - x_0)^2 + (y - y_0)^2} dx \tag{2.20}$$

2.1.2. PANEL MODEL SETUP

Panels of finite length represent the airfoil's surface with sufficient detail to capture its shape—the system's solution results in the strength of each elementary solution on the airfoil's panels. A panel method only requires the solution to be found at the N panels distributed over the surface for however many elementary solutions are chosen to represent the system.

Each panel consists of a source and vorticity. The influence of these points and the shed wake vortices results in a flow field around the airfoil. The governing conditions lead to the solution of the strengths of each of these elementary solutions. The source strengths over the panels are set to meet the boundary condition of no-penetration over the airfoil. Solving for the vorticity around the airfoil relies on the Kutta condition and Kelvin's theorem.

SINGLE WAKE

The single wake situation is a case of a double-wake method when the flow is completely attached to the airfoil. As mentioned previously, each of the panels has a given source distribution with the strength of a given point defined as σ_i. The vorticity distribution over the body, γ_b, is considered constant throughout the surface. In the near-wake, a panel represents the wake that will soon shed. This panel has a vorticity γ, an angle θ_W^Δ, and a magnitude of γ_w^Δ. The vorticity can be integrated over the surface to obtain a circulation of Γ_W^i. As this is an unsteady simulation, the strengths of these elementary

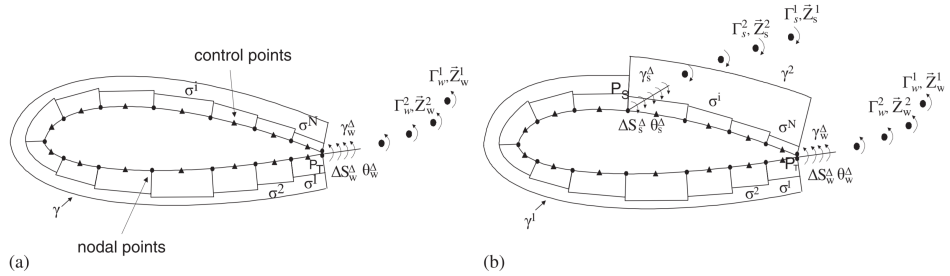

Figure 2.1: Setup of single-wake and double-wake solution, indicated by a) and b) respectively [16]

solutions are functions of time, and the airfoil sheds a wake at every timestep to satisfy Kelvin's theorem of circulation conservation. At a given timestep, there are $T-1$ shed wakes released by the airfoil in the flow field.

Following this discretization of the panels in this manner, there are N_p+2 unknowns. There is vorticity over the body, γ_b, source distributions over N_p panels, σ, and the circulation shed in the near wake, Γ_W. Given the unknowns, N_p+2 boundary conditions are required to find a unique solution to this problem. These are the no penetration at N_p panels, Kelvin's theorem, and the Kutta condition.

A superposition of the aforementioned elementary solutions at an arbitrary time, $t=m$, constructs the inviscid flow field as follows:

$$\begin{aligned}\mathbf{q}_i(\mathbf{x};t) = &\sum_{i=1}^{N}\frac{\sigma^i(t)}{2\pi}\int_{S_B^i}\frac{\mathbf{r}}{r^2}\mathrm{d}s(\mathbf{y}) + \frac{\gamma_b(t)}{2\pi}\sum_{i=1}^{N}\int_{S_B^i}\frac{\mathbf{r}\times\mathbf{k}}{r^2}\mathrm{d}s(\mathbf{y}) \\ &+ \frac{\gamma_w^{\Delta}(t)}{2\pi}\int_{\Delta S_w^{\Delta}(t)}\frac{\mathbf{r}\times\mathbf{k}}{r^2}\mathrm{d}s(\mathbf{y}) + \sum_{j=1}^{m-1}\frac{\Gamma_w^j}{2\pi}\frac{\left(\mathbf{x}-\mathbf{Z}_w^j(t)\right)\times\mathbf{k}}{\left|\mathbf{x}-\mathbf{Z}_w^j(t)\right|^2}\end{aligned} \tag{2.21}$$

σ is the strength of the source at every panel.
γ_b is the vorticity distribution over the body
γ_w is the vorticity distribution in the near wake
Γ_W is the shed point vortices in the wake

The strengths of the sources distributions at the panels are obtained from the boundary condition. The condition for no penetration requires the resultant velocity field to have no normal component at the airfoil's surface. For a reference frame fixed to the airfoil:

$$\mathbf{q_e}(t)\cdot\mathbf{n}(t) = 0 \tag{2.22}$$

The strength of the vorticity at the wake is found by applying Kelvin's theorem combined with the Kutta condition. The Kutta condition claims that "the flow leaves the sharp

trailing edge of an airfoil smoothly and the velocity there is finite." In unsteady flow, Basu and Hancock [17] interpret this condition as zero loading at the trailing edge and the near wake. To cause a smooth exit over the airfoil, the forces of the system should have equal forces on both sides of the trailing edge. This condition requires that $p^+ = p^-$, where p^+ and p^- refer to the pressures on the suction and pressure side, respectively. Applying the Bernoulli equation to the trailing edge:

$$\frac{\partial \phi^+}{\partial t} - \frac{\partial \phi^-}{\partial t} + \frac{\left(u_s^+\right)^2 - \left(u_s^-\right)^2}{2} + \frac{p^+ - p^-}{\rho} = 0 \Rightarrow \frac{\partial \phi^+}{\partial t} - \frac{\partial \phi^-}{\partial t} + \frac{\left(u_s^+\right)^2 - \left(u_s^-\right)^2}{2} = 0 \tag{2.23}$$

The condition of attached flow defines the change in circulation in time as follows:

$$\frac{\partial \phi^+}{\partial t} - \frac{\partial \phi^-}{\partial t} = \frac{\partial \Gamma}{\partial t} \tag{2.24}$$

Thus Bernoulli's equation defines the change in derivative of circulation:

$$-\frac{\partial \Gamma_B}{\partial t} = \frac{\left(u_s^+\right)^2 - \left(u_s^-\right)^2}{2} \tag{2.25}$$

Kelvin's theorem states that "the time rate of change of circulation around a closed curve consisting of the same fluid elements is zero"[15]. As the airfoil moves through a fluid and gains a circulation over its body Γ_B, the circulation shed in the wake, Γ_W, must be equal and opposite. If the model starts from a condition for which there already is circulation around the airfoil, the starting vortex accounts for the initial conditions.

$$\frac{D\Gamma}{Dt} = \frac{1}{\Delta t}(\Gamma_B + \Gamma_W) = 0 \tag{2.26}$$

$$\Gamma_B = \Gamma_W \tag{2.27}$$

For a development of the solution in time, the circulation contained in the near wake can be expressed from Kelvin's theorem as well:

$$\frac{D\Gamma}{Dt} = \gamma_W \Delta S_W^\Delta + \Delta \Gamma_B = 0 \tag{2.28}$$

$$\gamma_W \Delta S_W^\Delta = -\Delta \sum_{i+1}^{N} \Gamma_{B_i} \tag{2.29}$$

Expressing this term as non-time dependent, with a shed starting wake, the requirement for circulation conservation according to Kelvin's theorem at a time $t = m$ is:

$$\gamma_W^{\Delta}(t)\Delta S_W^{\Delta} + \sum_{j=1}^{m-1} \Gamma_w^j + \sum_{i+1}^{N} \Gamma_{B_i} = 0 \tag{2.30}$$

The length of the wake, ΔS_W^{Δ}, is used to represent the near wake vorticity. Riziotis and Voutsinas [16] use the trailing edge velocity multiplied by the timestep as a formula for this length. An average between the suction and pressure side defines the trailing edge velocity.

$$\Delta S_W^{\Delta} = \frac{\left(u^+ + u^-\right)}{2} \cdot \Delta t \tag{2.31}$$

By expressing the circulation in terms of the velocity at the trailing edge, $\gamma_W = u^+ - u^-$, the Kutta condition can be reformulated from Kelvin's theorem:

$$\gamma_W \Delta S_W^{\Delta} = -\Delta\Gamma_B \tag{2.32}$$

$$(u^+ - u^-) \cdot \frac{\left(u^+ + u^-\right)}{2} \cdot \Delta t = -\Delta\Gamma_B \tag{2.33}$$

$$\frac{\left(u^+\right)^2 - (u^-)^2}{2} = -\frac{\Delta\Gamma_B}{\Delta t} \tag{2.34}$$

Finally, one must obtain the orientation of the near wake surface. Basu and Hancock [17] assume the direction of emitted wakes to be aligned to either the lower or upper trailing edge, depending on the bound circulation. Zanon et al. [1] note that this formulation is incorrect when there is no change in circulation over time. Therefore, the orientation is taken to be the average direction between the two velocities on the upper and lower trailing edge panels.

DOUBLE WAKE

In order to account for the thick boundary layer, the model can shed an additional shear layer at the point of separation. This model aims to capture the characteristics of separated flow more accurately. Several formulations of a double-wake method have been developed in the past. For steady separated flow around an inclined plate, Sarpkaya [18] employed two shed wakes, one at the leading edge and one at the trailing edge, showing an improvement over a single wake model. Katz [19] improved upon this by applying it to a thin cambered airfoil. In his model, a predefined separation point designates the location of a shed wake, finding its location through experimentation. This method showed good agreement of the periodic behavior of wake shedding compared to physical flow visualizations. Extending the problem to a thick airfoil, Vezza and Galbraith [20] developed a panel method with a given separation point over the suction side. The results obtained from the model matched the experimental data closely. Modeling a dynamic stall with a double wake was demonstrated to be possible by Riziotis and Voutsinas [21], and then improved upon by strong coupling in a later work [16]. Marion et al. [22] showed

that a double-wake captures the deep stall flow considerably well when applying this method to fully stalled airfoils. Zanon et al. [1] found good agreement with experimental PIV measurements for use in vertical axis wind turbine simulation.

A double-wake model aims to better represent the characteristics of stalled flow by shedding vorticity at the separation point. While the general problem stays the same, inviscid flow is solved through the superposition of elementary solutions, and the degrees of freedom of the problem are altered. While in the single-wake model, the vorticity distribution over an airfoil is constant, the vorticity in a double-wake setup consists of two distributions. Distribution over the pressure side wrapping up to the pressure point represents the attached flow, and a distribution from the separation point until the trailing edge represents the separated flow over the airfoil. The second near-wake panel at the separation point behaves much like the trailing edge near-wake panel in the single-wake model. The new formulation of the inviscid contribution to the flow field represents these two changes.

$$\begin{aligned}\mathbf{q}^i(\mathbf{x};t) = &\sum_{i=1}^{N}\frac{\sigma^i(t)}{2\pi}\int_{S_B^i}\frac{\mathbf{r}}{r^2}\mathrm{d}s(\mathbf{y}) + \frac{\gamma_b^1(t)}{2\pi}\sum_{i=1}^{N_{P_S}-1}\int_{S_B^i}\frac{\mathbf{r}\times\mathbf{k}}{r^2}\mathrm{d}s(\mathbf{y})\\ &+\frac{\gamma_b^2(t)}{2\pi}\sum_{i=N_{P_S}}^{N}\int_{S_B^i}\frac{\mathbf{r}\times\mathbf{k}}{r^2}\mathrm{d}s(\mathbf{y}) + \sum_{p=w,s}\frac{\gamma_p^\Delta(t)}{2\pi}\int_{\Delta S_p^\Delta(t)}\frac{\mathbf{r}\times\mathbf{k}}{r^2}\mathrm{d}s(\mathbf{y})\\ &+\sum_{\substack{j=1\\p=w,s}}^{m-1}\frac{\Gamma_p^j}{2\pi}\frac{\left(\mathbf{x}-\mathbf{Z}_p^j(t)\right)\times\mathbf{k}}{\left|\mathbf{x}-\mathbf{Z}_p^j(t)\right|^2}\end{aligned} \tag{2.35}$$

The solution for the strengths of the elementary solutions follows similarly to the single-wake situation. The boundary condition for no penetration dictates the strengths of the source distributions on the airfoil panels. First, one must find the vorticity distribution over the airfoil and the strength of the shed circulation from the trailing edge and separation point. Applying the unsteady Kutta condition per Vezza et al.[20] and the Bernoulli equation over the separation point achieves this goal.

$$\left(\frac{p_a^+}{\rho}+\frac{(u^+)^2}{2}+\frac{\partial\phi^+}{\partial t}\right)-\left(\frac{p^-}{\rho}+\frac{(u^-)^2}{2}+\frac{\partial\phi^-}{\partial t}\right)=h^+-h^-=\Delta h \tag{2.36}$$

The exponents $^+$ and $^-$ indicate the values just before and after the separation point. The previous Kutta condition states that the forces are equivalent on either side and thus $p^+ - p^- = 0$. The velocity immediately after the separation point is zero as the flow leaves the airfoil. Thus the finalized equation for the separation point can be written as:

$$\frac{(u^+)_S^2}{2}=\frac{\partial}{\partial t}(\Delta\phi_S)+\Delta h \tag{2.37}$$

The Bernoulli equation for the trailing edge has already been treated in the single wake and can be expressed as:

$$\left(\frac{p^+}{\rho}+\frac{(u^+)^2}{2}+\frac{\partial\phi^+}{\partial t}\right)-\left(\frac{p^-}{\rho}+\frac{(u^-)^2}{2}+\frac{\partial\phi^-}{\partial t}\right)=h^+-h^-=\Delta h \tag{2.38}$$

Subsequently, applying the Kutta condition results in the following relation:

$$\frac{(u^+)_W^2-(u^-)_W^2}{2}=\frac{\partial}{\partial t}(\Delta\phi_W)+\Delta h \tag{2.39}$$

Equation 2.37 and Equation 2.39 are subtracted from each other, resulting in the relation for the vorticity shed in time.

$$\frac{\partial}{\partial t}(\Delta\phi_W)-\frac{\partial}{\partial t}(\Delta\phi_S)=\frac{(u^+)_W^2-(u^-)_W^2}{2}-\frac{(u^+)_S^2}{2} \tag{2.40}$$

$$\frac{\partial\Gamma_b}{\partial t}=\frac{(u^+)_W^2-(u^-)_W^2}{2}-\frac{(u^+)_S^2}{2} \tag{2.41}$$

As the vorticity at the separation point becomes the difference in velocity and the size of the near wake panel becomes the local velocity multiplied by the timestep, the relation is expressed in terms of the near wake panel.

$$\frac{\partial\Gamma_b}{\partial t}=\frac{(u^+)_W^2-(u^-)_W^2}{2}\frac{\partial t}{\partial t}-\frac{(u^+)_S^2}{2}\frac{\partial t}{\partial t} \tag{2.42}$$

$$\frac{\partial\Gamma_b}{\partial t}=\frac{\partial}{\partial t}\left(\gamma_W\Delta S_W^\Delta+\gamma_S\Delta S_S^\Delta\right) \tag{2.43}$$

2.2. VISCOUS FLOW

While the outer flow around the airfoil was considered inviscid, the same assumptions are no longer valid for the boundary layer close to the airfoil's surface. With fewer assumptions, the model must include more terms, and thus a more sophisticated equation must be solved. As the model at hand also aims to model the effects of dynamic flow, the model must have sufficient accuracy in such a flow regime. This work uses the approach from Drela and Giles [23] in their work on developing a viscous-inviscid interaction model. The solution consists of a two-equation integral formulation for both the laminar and turbulent flow section, with a closure term based on dissipation. The unsteady formulation has been developed based on the work of Riziotis and Voutsinas [16] and used to adapt the aforementioned steady equations.

The integral boundary-layer equations seek to obtain several values over the airfoil's surface to describe the flow. As the airfoil itself highly perturbs the flow, the governing equations seek to describe the relations of the flow compared to the inviscid case outside of the airfoil's influence. Within the flow regimes that this work considers, the relations consist of the variables provided in the nomenclature section.

In his paper from 1949, Thwaites [24] introduced a method of solution for the laminar boundary layer. The method relies on Prandtl's steady two-dimensional boundary-layer flow to solve for the aforementioned variables.

$$\frac{u\partial u}{\partial x} + \frac{v\partial v}{\partial y} = UU' + v\frac{\partial^2 u}{\partial y^2} \tag{2.44}$$

However, relying on a single equation to model the boundary-layer flow assumes a unique relation between the shape parameter and the local pressure gradient. Separated flow shows this not to be the case, and thus the model has to be adapted for use in this case. Defining the flow through two equations, Drela and Giles [23] rely on a standard formulation for the momentum and kinetic energy shape parameter equations. The two relations stem from the laws of conservation of mass and momentum.

$$\frac{\partial(\rho u_s)}{} + \frac{\partial(u_n}{\partial n} = 0 \tag{2.45}$$

$$\rho u_s \frac{\partial u_s}{\partial s} + \rho u_n \frac{\partial u_n}{\partial n} = \rho_e u_e \frac{du_e}{ds} + \frac{\partial \tau}{\partial n} \tag{2.46}$$

The first relation given by Drela can be obtained by integrating the momentum equation across the boundary layer.

$$\frac{s}{\theta}\frac{d\theta}{ds} = \frac{s}{\theta}\frac{C_f}{2} - \left(\frac{\delta^*}{\theta} + 2 - M_e^2\right)\frac{s}{u_e}\frac{du_e}{ds} \tag{2.47}$$

The second relation is the kinetic energy integral equation. By multiplying the momentum by velocity, a kinetic energy equation is obtained, and integrated across the boundary layer, resulting in:

$$\frac{s}{\theta^*}\frac{d\theta^*}{ds} = \frac{s}{\theta^*}2C_D - \left(\frac{2\delta^{**}}{\theta^*} + 3 - M_e^2\right)\frac{s}{u_e}\frac{du_e}{ds} \tag{2.48}$$

The relations developed are applicable for the laminar and turbulent boundary layer, with differing closure relations for each case. This method accurately simulates the entire boundary layer and has been relied on heavily for obtaining airfoil polars in the form of XFOIL[25]. Its application within a panel method has shown to be robust, and the numerical results obtained correlate well with experimental data.

When considering dynamical stall, an unsteady aerodynamic phenomenon, the applicability of using the two-equation model is limited. As the authors derive the governing relations derived with assumptions of steady flow, they could only apply them in pitching cases of low unsteadiness $\kappa < 0.05$. For broader model applicability, the model could consider the unsteady formulation of the boundary-layer equations. In their double-wake dynamic stall model, Voutsinas and Riziotis [21] derive the unsteady equations:

$$\frac{1}{\rho_f q_{f\tau}^2}\frac{\mathrm{d}}{\mathrm{d}t}\left(\rho_f q_{f\tau}\delta^*\right)+\frac{\mathrm{d}\theta}{\mathrm{d}s}+(2+H)\frac{\theta}{q_{f\tau}}\frac{\mathrm{d}q_{f\tau}}{\mathrm{d}s}+\frac{\theta}{\rho_f}\frac{\mathrm{d}\rho_f}{\mathrm{d}s}=\frac{C_f}{2} \tag{2.49}$$

$$\begin{aligned}&\frac{1}{\rho_f q_{f\tau}^3}\frac{\mathrm{d}}{\mathrm{d}t}\left(\rho_f q_{f\tau}^2\theta\right)+\frac{1}{\rho_f q_{f\tau}}\frac{\mathrm{d}}{\mathrm{d}t}\left(\rho_f\delta^*\right)+\frac{2}{q_{f\tau}^2}\frac{\mathrm{d}q_{f\tau}}{\mathrm{d}t}H^{**}\theta-\frac{H^*}{\rho_f q_{f\tau}^2}\frac{\mathrm{d}}{\mathrm{d}t}\left(\rho_f q_{f\tau}\delta^*\right)\\&-\frac{4\Omega}{q_{f\tau}}\Theta_n+\theta\frac{\mathrm{d}H^*}{\mathrm{d}s}+\left(2H^{**}+H^*(1-H)\right)\frac{\theta}{q_{f\tau}}\frac{\mathrm{d}q_{f\tau}}{\mathrm{d}s}=2C_D+\frac{2a}{q_f^2}\delta^*-H^*\frac{C_f}{2}\end{aligned} \tag{2.50}$$

Considering the previously made assumption of incompressibility in low-speed flows, the equations are adapted slightly with the derivative of density, and its derived terms, dropping out.

$$\frac{1}{q_{f\tau}^2}\frac{\mathrm{d}}{\mathrm{d}t}\left(q_{f\tau}\delta^*\right)+\frac{\mathrm{d}\theta}{\mathrm{d}s}+(2+H)\frac{\theta}{q_{f\tau}}\frac{\mathrm{d}q_{f\tau}}{\mathrm{d}s}=\frac{C_f}{2} \tag{2.51}$$

$$\begin{aligned}&\frac{1}{q_{f\tau}^3}\frac{\mathrm{d}}{\mathrm{d}t}\left(q_{f\tau}^2\theta\right)+\frac{1}{q_{f\tau}}\frac{\mathrm{d}}{\mathrm{d}t}\left(\delta^*\right)-\frac{H^*}{q_{f\tau}^2}\frac{\mathrm{d}}{\mathrm{d}t}\left(q_{f\tau}\delta^*\right)+\theta\frac{\mathrm{d}H^*}{\mathrm{d}s}+\left(H^*(1-H)\right)\frac{\theta}{q_{f\tau}}\frac{\mathrm{d}q_{f\tau}}{\mathrm{d}s}\\&=2C_D+\frac{2a}{q_f^2}\delta^*-H^*\frac{C_f}{2}\end{aligned} \tag{2.52}$$

While these equations are the extended from the steady boundary layer, they are only necessary for cases of high unsteadiness with $\kappa > 0.05$. While these equations are valid for all flows, they can be computationally expensive and should only apply in specific cases.

However, finding a solution to these equations requires a closure relation, as they are unsolvable in their current state. Due to the significantly different behaviors between laminar and turbulent flow, the relations used differ in the two flows.

2.2.1. LAMINAR BOUNDARY LAYER

For laminar flow, the solution for the two-equation method comes from the assumption of a given profile family. A profile family dictates the relation of the boundary-layer parameters and distance from the surface as a function of the shape factor. Within laminar flow, Drela [26] develops laminar closure relations based on the Falkner-Skan one-parameter profile family. In his work, Drela differentiates between the kinetic shape parameter H_k and the shape parameter H. For the foreseen applications of the model, the incompressible flow assumption dictates these be identical. The functions for the kinetic energy shape parameter H^*, skin friction coefficient C_f, and the dissipation coefficient C_D are given below:

$$H^* = \begin{cases} \frac{(H-4.35)^2}{90(H+1)} - 0.0278\frac{(H-4.35)^3}{H+1} + 1.528 - \frac{\left(H^2-4.35H\right)^2}{5000}, & \text{if } H < 4.35 \\ 0.015\frac{(H-4.35)^2}{H} + 1.528, & \text{if } H \geq 4.35 \end{cases} \tag{2.53}$$

$$C_f = \begin{cases} \left(0.0727\frac{(5.5-H)^3}{(H+1)} - 0.07\right)\frac{1}{Re_\theta}, & \text{if } H < 5.5 \\ \left(0.015\left(1 - \frac{1}{(H-4.5)}\right)^2 - 0.07\right)\frac{1}{Re_\theta}, & \text{if } H \geq 5.5 \end{cases} \tag{2.54}$$

$$\frac{2C_D}{H^*} = \begin{cases} \left(0.00205(4-H)^{5.5} + 0.207\right)\frac{1}{Re_\theta}, & \text{if } H < 4 \\ \left(\frac{(H-4)^2}{1+0.02(H-4)^2} - 0.0016 + 0.207\right)\frac{1}{Re_\theta}, & \text{if } H \geq 4 \end{cases} \tag{2.55}$$

The laminar flow also experiences the growth of instabilities as it continues over the airfoil. Once these instabilities grow to a critical value, a transition occurs, and the flow enters a turbulent regime. This process is detailed in the next section.

2.2.2. TURBULENT BOUNDARY LAYER

For the turbulent boundary layer, the closure relation is developed using the skin friction relation and a velocity profile formula. Due to its chaotic nature, the velocity profiles of turbulent flow are much harder to characterize. Swafford [27] found velocity profiles for turbulent separated boundary-layer flow in two dimensions through experiment. The resulting relation for skin friction is:

$$C_f = \begin{cases} 0.3e^{-1.33H}\left(\frac{\log(Re_\theta)}{2.3026}\right)^{-1.74-0.31H} \\ +0.00011\left(\tanh\left(4 - \frac{H}{0.875}\right) - 1\right), & \text{if } Re_\theta \geq e^3 \\ 0.3e^{-1.33H}\left(\frac{3}{2.3026}\right)^{-1.74-0.31H} \\ +0.00011\left(\tanh\left(4 - \frac{H}{0.875}\right) - 1\right), & \text{if } Re_\theta < e^3 \end{cases} \tag{2.56}$$

Therefore the velocity profile is:

$$\frac{u}{u_e} = \frac{u_\tau}{u_e}\frac{s}{0.09}\arctan\left(0.09y^+\right) + \left(1 - \frac{u_\tau}{u_e}\frac{s\pi}{0.18}\right)\tanh^{1/2}\left[a(\eta/\theta)^b\right] \tag{2.57}$$

where

$$\frac{u_\tau}{u_e} = \left|\frac{C_f}{2}\right|^{1/2}, \quad s = \frac{C_f}{|C_f|}, \quad y^+ = \frac{u_\tau}{\mu_e/\rho_e}\eta$$

The constants a and b are determined implicitly by substituting Equation 2.57 into the standard momentum and displacement thickness equations [23]. The energy thickness shape parameter can then be derived as:

$$H_0 = \begin{cases} 3 + \frac{400}{Re_\vartheta}, & \text{if } Re_\vartheta > 400 \\ 4, & \text{if } Re_\vartheta \leq 400 \end{cases} \tag{2.58}$$

$$Re_z = \begin{cases} Re_\vartheta, & \text{if } Re_\vartheta > 200 \\ 200, & \text{if } Re_\vartheta < 200 \end{cases} \tag{2.59}$$

$$H^* = \begin{cases} \left(0.5 - \frac{4}{Re_z}\right)\left(\frac{H_0 - H}{H_0 - 1}\right)^2 \frac{1.5}{H+0.5} + 1.5 + \frac{4}{Re_z}, & \text{if } H < H_0 \\ (H - H_0)^2 \left(\frac{0.007\log(Re_z)}{\left(H - H_0 + \frac{1}{\log(Re_2)}\right)^2} + \frac{0.01499}{H}\right) + 1.5 + \frac{4}{Re_z}, & \text{if } H \geq H_0 \end{cases} \tag{2.60}$$

The equation for the skin friction coefficient only depends on the local boundary layer parameters. Since the dissipation coefficient is defined by the skin-friction coefficient and the same parameters, it would experience a quick response to changing flow conditions. This statement correlates well to the expected behavior found through experimentation. On the other hand, while the shear stress coefficient behaves similarly within this model, this is not a good representation of its behavior in real life. To account for this, Green et al. [28] develop a function for the shear-stress coefficient C_τ using a lag-entrainment method. The function defines the derivative of C_τ as the difference between it and the shear-stress equilibrium coefficient $C_{\tau_{EQ}}$. This method achieves the real-life phenomenon of gradual convergence. The new shear-lag rate equation is significantly more able to accurately capture the development of the shear stress coefficient:

$$\frac{\theta\left(3.15 + \frac{1.72}{H_k - 1}\right) + \delta^*}{C_\tau} \frac{dC_\tau}{d\xi} = 4.2\left(C_{\tau_{EQ}}^{\frac{1}{2}} - C_\tau^{\frac{1}{2}}\right) \tag{2.61}$$

$$C_{\tau_{EQ}} = \left(H^* \frac{0.015}{1 - U_s} \frac{(H_k - 1)^3}{H_k^2 H}\right) \tag{2.62}$$

and

$$U_s = \frac{H^*}{6}\left(\frac{4}{H} - 1\right) \tag{2.63}$$

These equations originate from the $G - \beta$ locus of equilibrium boundary layers. The formulation presented by Drela and Giles [23] defines the tunable values for the locus as $A = 6.7$ and $B = 0.75$. Van Rooij suggested an alteration to this in his paper on developing a better aerodynamic tool, RFOIL [29]. The suggestions are to use $A = 6.75$ and $B = 0.83$, leading to the new definition.

$$G = 6.75\sqrt{1 + 0.83\beta} \tag{2.64}$$

$$G = \frac{H_k - 1}{H_k} \frac{1}{\sqrt{0.5 C_f}} \tag{2.65}$$

$$\beta = -\frac{2}{C_f} \frac{\delta *}{u_e} \frac{du_e}{d\zeta} \tag{2.66}$$

The final flow regime is that of the released vortex wake sheets from the separation point and the trailing edge. As these sheets were assumed to be sufficiently thin, boundary-layer theory can be applied. The flow in the wake is fully turbulent; thus, most of the relations derived in this section are applicable due to similar flow conditions. The governing condition is that due to its nature and location, it does not experience skin friction, and thus C_f must be set to zero.

2.3. PREDICTION OF THE SEPARATION AND REATTACHMENT

As the current model relies on inviscid calculations for the general flow behavior, the viscous boundary layer defines the boundary condition at the airfoil surface. Within the boundary layer calculation, the prediction of the separation point is crucial as this location dictates the position of the second shed wake. Within the viscous calculation, there are two modes of flow, laminar and turbulent, which can experience separation with different behavior. As such, multiple methods are required to predict the location of the separation point.

While current models can accurately predict the transition location with a clean configuration, adding a vortex generator can significantly alter this condition. Early bypass transition due to the vortex generator alters the boundary layer equations, which could reflect more accurately the performance of the airfoil. Several authors have also stressed the importance of accurate prediction in the past. Drela and Giles [25] attribute the success of their viscous-inviscid interaction model to the accurate prediction of the separation bubble behavior and location. Katz's [19] formulation of a double-wake method uses a predefined separation location, and he notes in his work that finding the exact location would lead to better results. In the model proposed by Riziotis and Voutsinas [16], the location of the separation point dictates the separation wake shedding location, and thus the authors place great importance on the separation prediction model. As the process of dynamic stall includes separation and reattachment of flow, Sheng et al. [30] found that a better representation of the reattachment of flow leads to a more accurate performance of the Leishman-Beddoes model. This idea was further espoused by Zanon et al. [1], who applied the idea in a model for vertical axis wind turbines and found close agreement with experimental data and CFD simulation.

2.3.1. LAMINAR BOUNDARY LAYER

The laminar boundary layer is solved using Thwaites' single-parameter method [24]. From the solution of the boundary-layer equations, several resulting variables dictate the general behavior of the flow. The model defines the flow separation location as the point at which the skin friction coefficient reaches zero. At this point, the pressure along the

airfoil's chord increases, which causes the flow to move upwards and separate. This point indicates where the velocity profile will indicate backward flow, the criterion for which is as follows:

$$\left(\frac{\partial u}{\partial y}\right)_{y=0} = 0 \tag{2.67}$$

LAMINAR-TURBULENT TRANSITION

However, in some cases, the condition for flow separation in the laminar boundary layer is never reached. A lack of separation in the laminar portion of the boundary layer means that the flow would separate in turbulent flow, requiring the prediction of the laminar-turbulent transition point. The characteristics that describe laminar and turbulent flow are that laminar flow is highly predictable and ordered, while turbulent flow is unstable and chaotic. Following this thought, one could theorize that the transition point would occur when the instabilities in laminar flow grow to a critical point. This idea was developed in the work of J.L. van Ingen [31], who came up with the e^N method. The paper demonstrates a semi-empirical relation based on stability theory, which considers the velocity profile and Reynolds number, yielding a single parameter called the amplification factor, which, upon growing to a value of $e^{7.8}$, indicates transition on a flat plate.

Since its inception, this work has been applied and improved in numerous works. Drela and Giles applied this method within their viscous-inviscid interaction model by calculating the amplification factor and disturbance growth rates for the boundary layer parameters [23]. The model uses Falkner-Skan velocity profiles to solve the Orr-Sommerfeld equation for the spatial amplification factors at varying shape parameters, Reynolds numbers, and instability frequencies. Equation 2.68 gives the formula for the spatial amplification factor; when the value of $\tilde{n}$ is greater than 9, a laminar-turbulent transition occurs.

$$\tilde{n}(\xi) = \int_{\xi_0}^{\xi} \frac{\mathrm{d}\tilde{n}}{\mathrm{d}\xi} \mathrm{d}\xi \tag{2.68}$$

$$\frac{\mathrm{d}\bar{n}}{\mathrm{d}\xi}(H_k, \theta) = \frac{\mathrm{d}\tilde{n}}{\mathrm{d}Re_\theta}(H_k) \frac{m(H_k)+1}{2} \ell(H_k) \frac{1}{\theta} \tag{2.69}$$

In equation Equation 2.68, ξ_o indicates the point where the Reynolds number $\mathrm{Re}_\theta = Re_{\theta_0}$. The change from integration over the range of Reynolds numbers to a spatial integration allows for better representation of behavior in laminar separation bubbles. The relation for $\tilde{n}$ is solved as another boundary layer to ensure strong coupling to the rest of the system.

BYPASS TRANSITION DUE TO VORTEX GENERATORS

While transition point can be specified, because transition does not necessarily occur at the VG, it is crucial to develop a model which would allow for the prediction of the transition point with its influence taken into account. The vortex generator can induce

a roughness-based transition, which happens when the flow's critical roughness height is equal to the height of the vane, $h_{\text{VG}} = h^*_{crit}$ [32, p. 134]. The method introduced by Kerho and Kramer [2] evaluates whether the dimensions of the VG are sufficient to trigger a transition. If separation has not occurred at the location of the VG, the VG must be in a laminar flow regime and can thus induce transition. To determine whether the VG dimensions are sufficient to promote transition, the velocity of the boundary layer, U_{VG}, is calculated at the height of the VG on an airfoil in a clean case. The roughness-based Reynolds number represents the ability of the VG to trigger a transition and is calculated as:

$$\text{Re}_{h_{\text{VG}}} = \frac{U_{\text{VG}} \rho \text{h}_{\text{VG}}}{\mu} \tag{2.70}$$

If $\text{Re}_{h_{\text{VG}}}$ is higher than the critical Reynolds number Re_{cr}, a transition will occur at the location of the VG. While there is no clear consensus on the correct choice for this value, Klebanoff et al. [33] combines experimental data with previous research to come up with a generalized criterion of $\text{Re}_{cr} = 600$. This criteria is a reliable measure of transition in steady airfoils and is a reasonable assumption for the unsteady boundary layer. The velocity at the airfoil location influences roughness-based transition. When calculating the clean case, this velocity will depend on the history. The clean case and VG case must therefore be iterated simultaneously until a transition occurs to capture the behavior of the VG.

As a vortex generator works by increasing the mixing of the flow, it does not affect a laminar flow, which does not have mixing by definition. Ergin and White [34] do note that instabilities from the shed wakes by the VG can trigger transition below the critical Reynolds number due to the instability of the distorted wake flow. As the model only considers a single VG, this will not influence the formulation of the transition prediction. In the case of no transition, the program would assume there is no VG, and no recalculation is required. If the VG does promote transition, the model specifies this point in the boundary layer equations by changing the formulation.

2.3.2. TURBULENT BOUNDARY LAYER

When the flow in the boundary layer transitions from laminar to turbulent, a different method must be applied to evaluate separation. The idea remains the same, as the goal is to find a point at which there is a strong enough adverse pressure gradient to create zero surface friction and allow the flow to separate.

The change in equations requires a closure relation for turbulent flow after a laminar-turbulent transition. In one of the more well-known applications of viscous-inviscid interaction panel methods, XFOIL [25], the turbulence closure relation comes from the work of Green et al. [28], which uses a lag-entrainment method. Using these relations, Drela and Giles [23] can accurately predict thin separation bubbles in their panel method. Furthermore, applying it to the double-wake method, Riziotis and Voutsinas [16] show that this is an effective method of separation calculation.

Extending this to unsteady flow, Rott [35] found that the separation point did not behave

the same way it did in the steady case. There was no singularity at the point of zero skin friction and reverse flow, and the boundary layer equations were still applicable. Sears [36] and Moore [37] examined this problem further and concluded that the point of unsteady separation is the point at which there is zero velocity and shear in the boundary layer. While this point would yield a singularity, it is difficult to find as the speed of the separation point is not known in the unsteady case. For the case of a pitching airfoil, the separation point moves from the original position of the steady case based on the direction of the motion.

The work succeeding this literature study aims to simulate an airfoil in a dynamic stall with vortex generators, an inherently unsteady phenomenon. The prediction of turbulent separation developed with steady turbulent flows in mind cannot be entirely accurate for the unsteady case of dynamic stall. Gad-El-Hak [38, p. 158] mentions that a consensus on the exact definition for unsteady separation has not been reached, and several propositions still exist. Despard and Miller [39] found through experimentation that they could accurately predict the separation point by finding the point furthest from the trailing edge experiencing no flow reversal. This discovery confirmed Moore's hypothesis and is an improvement over the formulation of steady separation for unsteady flows. Despite this, highly unsteady flows are not considered due to the model's applications in wind energy. Nonetheless, this formulation allows for a wider variety of cases to be input.

Examining the case of a pitching airfoil, $C_f < 0$ has proven to have acceptable performance in predicting the separation point with an airfoil pitch-up motion. On the other hand, the flow reattachment when pitching down has been a more challenging phenomenon to capture. In the case of low Reynolds number flow, the model fails to predict this phenomenon after a deep stall has occurred. Zanon et al. [1] propose an improved criterion for flow reattachment based upon the position of laminar separation on the pitch-up motion. During this motion, there is a laminar separation point, after which the flow will no longer reattach. Thus, by checking whether the current laminar separation position in the pitch-down motion is upstream of the critical separation point, it is possible to deduce whether reattachment can occur.

2.4. VISCOUS-INVISCID COUPLING

While the previous section pertained to the solutions over the inviscid and viscous parts of the flow, the two solutions must be combined to form a single flow model over an airfoil. Current models combine this by coupling the output of the viscous solution to the inviscid solution by introducing a variable to represent the change of the outer flow due to the airfoil's presence, as the viscous boundary layer changes the velocity and momentum profiles as opposed to the inviscid case.

The basis of viscous-inviscid coupling comes from the analysis performed by Lighthill [40], who investigated the effects of the boundary layer. Lighthill recognizes an inviscid outer flow and introduces the idea that the boundary layer must somehow displace it. The integral boundary relations dictate this displacement thickness at any streamwise coordinate:

$$\delta_1 = \frac{1}{U}\int_0^\infty (U-u)dz \tag{2.71}$$

While the flow is said to displace by a certain amount, a logical conclusion could be to offset the airfoil geometry in the inviscid solution, but that has not turned out to be the most effective approach. Instead, as the flow is displaced, there must be a velocity that causes this outer flow to displace. As the viscous solution is infinitely thin, the inviscid solution defines the velocity field; thus, the viscous correction would be sufficient to take it into account. The coupling term of transpiration velocity can be obtained by taking the normal velocity at any point over the airfoil.

In the context of an inviscid flow, the velocity field at the airfoil surface can be defined as the limit of the normal coordinate going to zero. To express this in the viscous flow formulation, this appears when the normal coordinate at the length scale tends to infinity. As the two velocity fields are equal, the model includes the viscous calculations through the boundary condition expressed as:

$$(w)_{\text{inviscid}} = \lim_{n/\delta^* \to \infty} w(s,n) \tag{2.72}$$

To find the contribution of the viscous boundary layer, Lighthill integrates the normal velocity component of the flow over the normal coordinate. As the model assumes the boundary layer to be infinitely thin, one can integrate the equation to infinity.

$$w_{\text{transpiration}} = -\frac{dq}{dx}z + \frac{d}{dx}\int_0^\infty q_e(s) - w_s(s,z)dz \tag{2.73}$$

Finally, to find the transpiration velocity, the relation is evaluated at the airfoil's surface ($z = 0$). By considering the previously defined term for displacement thickness, the transpiration velocity can be defined as:

$$w = \frac{d}{dx}(q_e\delta) \tag{2.74}$$

Integrating this into the inviscid flow solution, the normal velocity at the airfoil's surface is no longer set to zero but the transpiration velocity. Achieving this, however, is not straightforward and requires calculation. While the transpiration velocity can be defined, it is a function of the flow, and one must recalculate it in every timestep. This term originates from the viscous boundary layer, a function of the outer flow that impacts the outer flow. Therefore, it is self-defining, and an iteration algorithm must be applied to model the system properly.

While one could express the transpiration velocity as a simple source distribution, this can lead to numerical instability. Overcoming this requires a strong coupling by making the boundary condition a function of the elementary solutions on the panels. A strong viscous-inviscid interaction overcomes the Goldstein singularity[41], which arises from

the non-linear character of the equations. Removing this non-linearity removes the singularity. However, a linear representation of the separation is not as accurate as the aforementioned method, and thus strong coupling is used.

2.5. METHOD OF SOLUTION

This project focuses on building upon an existing double-wake vortex-panel method authored by A. Zanon [1]. While the cited paper features a detailed account of the solution method, this section summarizes the work.

The present code is written in MATLAB with subroutines in FORTRAN and is designed to simulate a wide range of inputs for the flow conditions, geometries, and complex movements beyond the simple pitching of the airfoil. Unsteady flow is the main focus and function of the code, which it solves by coupling the inviscid potential flow solution to the boundary layer solution derived from the boundary conditions. The model achieves the solution through three solution loops; an inviscid loop, a viscous loop, and a time-marching loop.

On the first iteration, the velocity at every control point is calculated from the freestream velocity; if the simulation loads from a previously saved point, it sums the contribution of all the wake and surface velocities. The wake panels at the trailing edge and separation point initialize with an initial guess of their relative angle $(\theta_w, \theta_{\text{sp}})$ and length (l_w, l_{sp}), any subsequent timesteps take this initial guess to be the value of the previous timestep. With these values, the model constructs the linear solution matrices with the boundary conditions, and the system is solved using a Gaussian elimination algorithm, resulting in new values for the relative and length of each panel (θ, l). If the values for θ and l do not match the previous iteration, the calculation continues until it reaches convergence. Solving for this matrix constitutes the "inviscid loop" of the model and tends to reach convergence very quickly.

The intermediate "viscous loop" part of the solution proceeds from the "inviscid loop" solution results, where the model initializes from the boundary layer thickness δ^* at the previous timestep. The boundary layer equations are solved over the airfoil and wake, and the solution checks for convergence upon reaching the criterion of matching edge velocities over the airfoil for the inviscid and viscous solutions. If the model does not converge, the new value for δ^* is chosen based on a relaxation formula to ensure stability and speed of the solution. The choice for this value takes into account the difference between the edge velocity of the boundary layer solution $u_{e,b}$ and the potential solution $u_{e,p}$, where K_{rx} is a constant chosen to guarantee faster convergence and a more stable solution.

$$\delta^{*n} = \delta^{*n-1}\left(1 + K_{rx}\frac{w_{e,b} - w_{e,p}}{w_{e,b}}\right) \tag{2.75}$$

Finally, the "time step loop" is the outer loop that continuously checks for convergence of the "inviscid loop"; the solution iterates for the inviscid and viscous parts until they reach parity. Once the two loops reach parity in their solutions, the program computes

the resultant aerodynamic forces and saves the simulation data for the current timestep in the directory. The wake panels beyond the prescribed limit become wake blobs with a vortex diameter that scales with the length of the wake panels. Once the boundary layer evaluates the flow for separation, all the vortex blobs convect with the velocity induced at their location, and the simulation progresses by a timestep.

3

VORTEX GENERATORS

Since the dawn of manned flight, the boundary layer has caused issues in performance in the form of separation and skin friction drag. Attempts to investigate and limit these effects have been ongoing since their discovery, and the first attempts are documented by Prandtl[42] along with the explanation of boundary-layer theory and development of separation criteria. He was the first to find a way to control the boundary layer through suction on the surface to delay separation.

With the first devices resulting from trial-and-error experimentation, performance enhancements from flow control devices were notable in their drag reduction, lift enhancement, and noise suppression. These arose primarily due to the flow control devices' success in delaying or preventing stall, achieved by the increased mixing due to the device itself or its ability to induce early laminar-turbulent transition. Improvements in lift performance, for example, can come at the cost of increased parasitic drag by the flow control device. Adding such devices to airfoils also allows for a much more comprehensive range of designs, making previously ineffective designs viable.

Controlling the flow is the process of achieving the desired changes in the boundary layer. Boundary layer control devices achieve these changes through an input of energy to the system or without, labeled as active and passive, respectively. Active boundary layer control was the first to appear in the field. From early experiments by Prandtl, he found that applying suction to the boundary layer increased the performance of the airfoil. Removing the low-energy flow at the bottom of the boundary layer decreased the drag experienced. Experiments with this idea were performed by Ackeret et al.[43], with promising results. Research also deemed air jets applied on the wing of an airplane successful, increasing the performance of the airfoil in terms of lift over drag. A benefit of active flow control inherently lies in its definition, as the system must expend energy to control the flow and can be turned on or off. A modern application of such a device was demonstrated by Amitay et al.[44] in the form of activatable jet actuators for suction on the boundary layer. Deployable vortex generators applied to helicopters improve

passive performance by retracting them when not needed[45]. Maestrello et al.[46] used boundary-layer heating to increase performance by varying the air's viscosity and density.

Contrary to active flow control devices, passive devices do not require energy to affect the boundary layer and usually rely on their geometry to achieve their purpose. Initial experimentation with this led to the development of the vortex generator by Taylor in 1946[8]. A vortex generator lies at the scale of the boundary layer and uses its property as a lifting surface to improve airfoil performance. Different design variations were introduced in the following years, as even though they all worked the same way, there was an endless possibility for design[47]. The advantage of passive devices is the simple and sturdy design with no moving parts. This immobility also means that the flow control is always there, even when it is unnecessary. In the case of fully attached flow at low angles of attack, a vortex generator only goes on to increase drag without benefiting the lift. The experiments of Schubauer and Spangenberg[47] detailed a few possible designs of flow control devices.

Despite multiple designs, vortex generators remain the most widely used and efficient form of passive flow control. A *vortex generator* is defined as a combination of vanes, a small flat plate, or an airfoil standing upright on the surface at an angle of attack to the flow. The purpose of a VG is to introduce a trailing vortex in the streamwise direction to the flow. The arrangement of such vanes forms one or more rows over the entire or a part of the airfoil span. The goal of the VG array is to influence the boundary layer flow; thus, the chordwise positioning of the VGs is a crucial design parameter that can differ drastically between the goals of a particular application. A guide to VG design by Pearcey[48] lists the possible layouts for vane-type generators. Here he attributes the success of a given VG design to the VG's ability to introduce a sufficient strength vortex at the desired location in the boundary layer. The arrangement of VGs can also impact the effectiveness of VGs in the form of counter- and co-rotating vortices. Neighboring vortices greatly influence the ability of the shed vortex to impact the flow through their induced velocity and interaction. Section 3.1 details the mechanism involved in this process and its influence on design.

Besides the relative VG positioning in VG configurations, the vane geometry has long been a close topic of study. The most critical design parameters lie in the height of the VG relative to the boundary layer $\frac{h}{\delta}$, the angle of attack with the incoming flow β_{VG}, the aspect ratio, and the area. An increase in the VG height positively influences the vortex shed's strength and increases the length it is present in the flow. However, it can lead to more significant parasitic drag due to the increased area. While most VG designs sized them to at least the size of the boundary layer, recent research has shown that submerged micro-VGs can exceed the performance of conventional designs in certain cases[50][51]. The height of the VG is a prominent factor in determining the optimal VG design, especially when considering the desired position of the vortex introduction to the flow. While the aspect ratio does not significantly impact the performance by itself, Pearcey[48] proposes the optimal value to be 2.5 from their experiments; Godard and Stanislas[49] give a lower bound of 2. As the angle of attack β increases, so does the skin friction and vortex strength[52] until around 18 deg, Godard and Stanislas[49] propose a design angle at 18 deg for optimum performance.

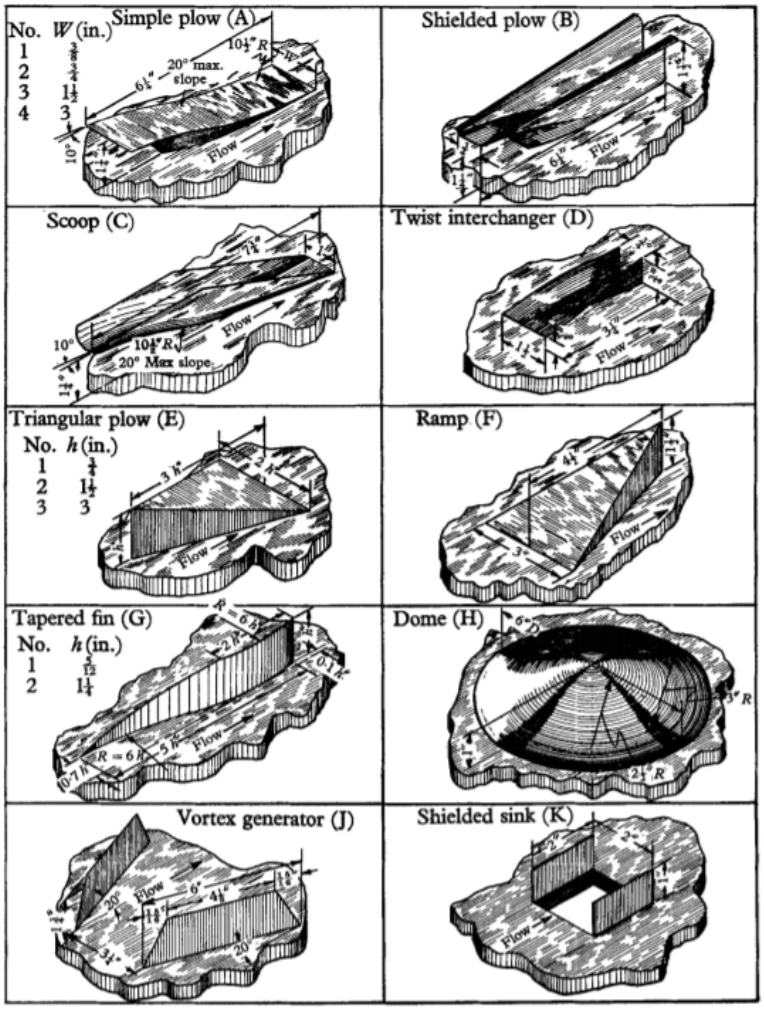

Figure 3.1: Passive control devices[47]

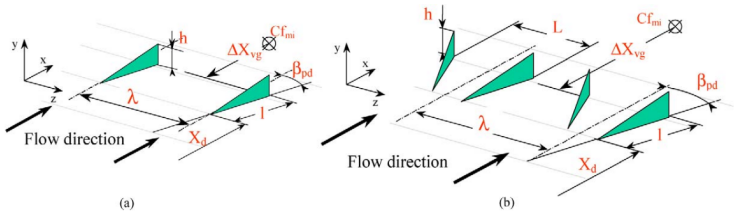

Figure 3.2: Geometry of (a) co-rotating passive devices, (b) counter-rotating passive devices[49]

3.1. EFFECTS OF VORTEX GENERATORS ON THE BOUNDARY LAYER

Research has long understood the applications of vortex generators in enhancing the airfoil performance; however, to truly understand the influence of design parameters, one must perform extensive computations. While aerodynamic simulations already exist for basic airfoils, these processes must include vortex generators. As these models work to achieve this goal, an understanding of the effects of VGs must first be established to ensure verification of accurate implementation.

The boundary layer is a region of flow where flow close to the wall has less momentum than the flow in the outer layer. At the extreme, at the wall itself, the flow has zero momentum and cannot overcome any pressure gradient. Interpolating between the outer flow with a given edge velocity U_e and zero velocity at the wall, shear between the layers and mixing must account for the momentum transfer from the faster moving layers of the surrounding flow to the slower moving layer near the wall. Shear as a flow property was discovered along with boundary-layer theory by Prandtl[42] in 1904. Schubauer and Spangenberg[47] performed the first study into the effect of mixing devices in the boundary layer in 1959. They recognized that flow mixing in the boundary layer alters its momentum profile, a mechanism found prominently in a turbulent flow. In this flow regime, the eddy viscosity can be over 100 times greater than the viscosity of the air at a laminar state. This viscosity affects the flow by energizing the layers near the wall, and the self-mixing turbulent flow can overcome more significant pressure gradients. Therefore, Schubauer and Spangenberg suggest artificially increasing the turbulent layer mixing, achieving better lift performance for an airfoil design. A vortex generator induces a vortex in the streamwise direction, promoting the mixing between the flow layers of varying velocities over the boundary layer. When placed correctly, this vortex introduces high energy flow to a region with lower mean energy. By re-energizing the lower layer, the flow near the airfoil's surface can cope with a more considerable pressure difference, resisting separation.

In order to examine the effect of this mixing on the boundary-layer, one must consider the Von-Karman momentum equation, previously defined in Equation 2.47. The assumption of incompressibility is made and a substitution is made for $C_f = \frac{\tau_w}{\frac{1}{2}\rho u_e^2}$ and $H = \frac{\delta*}{\theta}$.

$$\frac{d\theta}{dx} = \frac{\theta}{\rho u_e^2}\frac{dp}{dx}\left(\frac{\delta^*}{\theta} + 2\right) + \frac{\tau_w}{\rho u_e^2} \tag{3.1}$$

The first two terms represent the pressure gradient and wall friction effects. If this pressure gradient causes a force that slows down the flow, by the definition of $\delta*$, the displacement thickness will also decrease. The boundary layer analysis defines the impact of the vortex generators as a collection of changes in variables due to the induced mixing. Therefore, the values of interest are the displacement thickness $\delta*$, momentum thickness θ, shape factor H, and the skin friction coefficient C_f.

The introduction of mixing at the location of the vortex generator allows for a qualitative analysis of the equation. Over the VG, the added mixing occurs very rapidly and over a short distance. While a VG introduces mixing to an already turbulent flow, it is practical

to consider the case of laminar to turbulent transition, where a smooth flow suddenly experiences a large eddy viscosity and consequently mixing, a case comparable to the rapid introduction of mixing due to a VG. Over the airfoil, the momentum and displacement thickness grow alongside viscous forces in the boundary layer. The momentum thickness indicates the momentum lost at the surface of the airfoil due to the airfoil's body forces. When the flow reaches the laminar-turbulent transition point, the change in momentum thickness remains gradual, while the displacement thickness drops immediately. Due to the addition of mixing, this sudden change in the boundary layer occurs from the momentum loss over the boundary layer dispersing more evenly, as shown by Schubauer and Spangenberg[47]. The shape factor H, which represents the ratio of displacement thickness to momentum thickness, changes as a result. The case of VG-induced mixing experiences the same effects seen in a boundary layer transition. Therefore a VG should result in a sudden drop in the displacement thickness and an increase in momentum thickness.

While a qualitative analysis proves helpful in theoretical consideration, the performance of separation control is analyzed by Baldacchino[53]. An investigation into the effects of vortex-induced mixing considers the boundary-layer equations of momentum thickness θ and energy thickness $\theta*$. Combining these equations for the steady case with incompressible flow results in a combined equation:

$$\frac{\theta}{u_e}\frac{du_e}{dx} = \frac{1}{H-1}\left(\frac{C_f}{2} - \frac{2C_D}{H*}\right) \tag{3.2}$$

Dissipation is the measure of the local rate of conversion of kinetic energy to heat; it arises from the shear stresses acting on the fluid as it deforms at the shear strain rate $\frac{\partial u}{\partial n}$ [54].

$$\mathscr{D} \equiv \int_0^{n_e} \tau \frac{\partial u}{\partial n}\, \mathrm{d}n \tag{3.3}$$

The shear stresses have a laminar and turbulent contribution, resulting in an effective viscosity. Avoiding separation increases the ability of the flow to overcome pressure gradients, corresponding to a negative velocity gradient in this equation, thereby improving the performance of the airfoil. As separation occurs when the skin friction coefficient drops below zero (shown in Section 2.3), one should increase the coefficient of dissipation to minimize the left-hand side in Equation 3.2.

The conclusion from this relation thus confirms the postulation of the effect of mixing on the boundary layer given by Schubauer and Spangenberg[47]. In the case of separation, the adverse pressure gradient would be greater than the skin friction at the wall. When considering the momentum thickness difference over the transition point, the equation becomes a function of the dynamic pressure ratio, with the wall stress considered negligible.

$$\frac{\theta_2}{\theta_1} = \left(\frac{q_1}{q_2}\right)^{H/2+1} \tag{3.4}$$

This case assumes a constant shape factor for the sake of simplicity. The change in momentum comes only from the boundary layer experiencing a change in the dynamic pressure from q_1 to q_2. For a given jump in dynamic pressure, the only positive impact that mixing could have on the growth of the momentum thickness θ is to reduce the shape factor H. A decrease in the adverse pressure gradient can also reduce H; thus, one could conclude that the increased mixing of the fluid and the reduction of $\frac{dp}{dx}$ would have the same effect.

3.2. APPLICATIONS OF VORTEX GENERATORS

The previous section established the mathematical grounding for the effects of a VG. With the numerical background, the established predictions on the boundary layer changes can be applied to experimental situations and validated. While the boundary layer parameters have been the focus of the VG analysis so far, it is more helpful to look at them in the scope of an increase in performance. Within the context of power production in a wind turbine, this results in higher lift coefficients C_L and lower drag coefficients C_D. Achieving delayed separation and dynamic stall through vortex generators confirms the usefulness of VGs.

In their initial work, Schubauer and Spangenberg[47] experimented with the effect of added mixing by comparing the separation point in a clean airfoil case with different setups of mixing devices. They found that the results followed their reasoning in the numerical calculations, and the enhanced mixing had the same effect as a reduced adverse pressure gradient. The increased mixing resulted in delayed separation over the airfoil, with the effectiveness dictated by the induced parasitic drag and mixing in the flow. In an experimental setup of an airfoil experiencing early boundary layer transition leading to separation, Bragg et al.[55] found that the application of vortex generators as the mixing device could increase the lift while decreasing the drag. The work of Lin et al.[56] investigates the effect of different mixing devices, where they found that vortex generators submerged in the boundary layer were effective at controlling flow separation. In another investigation into submerged boundary layer vortex generators, Kerho et al.[57] found that optimized dimensions of the VG could yield up to a 38% reduction of drag coefficient at a given angle. By isolating the problem into a flow field over an airfoil with an adverse pressure gradient, Jenkins et al.[58] apply vortex generators to a flow undergoing separation and note the separation prevention properties of VGs.

While the previous section discussed the effects of separation, the discussion of VG applications in wind turbines must also consider the performance of vortex generators for unsteady flow. The field of wind energy sees vortex generators used broadly in delaying, lessening the impact of, or even preventing a dynamic stall from forming. While the application of VGs has been around since their development[8], an experiment by Carr and Mcalister[59] found that a VG placed at $(x/c) = 0.2$ delayed static stall, yet had no significant impact on the development of dynamic stall. However, a slat at the leading edge could limit dynamic stall phenomena. A dynamic stall occurs due to the shedding of the dynamic stall vortex from the leading edge as an adverse pressure gradient travels upwards from the trailing edge. An experiment by Choudhry et al.[60] found that counter-

rotating VGs could reduce the strength of the dynamic stall vortex (DSV). The author attributes this reduction to the vortices induced by VGs breaking up the large DSV. A study by Mai et al.[61] applied leading-edge vortex generators to helicopter blades and found better performance leading to lower fuel consumption and higher cruise speeds. Pape et al.[45] developed this concept and found that when comparing the results of the different parameters, an increase in the height of VGs resulted in a lower hysteresis of the lift. The taller VG increases the mixing experienced by the boundary layer, keeping it consistent over a blade rotation and breaking up the DSV more effectively.

3.3. INFLUENCE OF VG ON MIXING

The previous sections discussed the application of vortex generators to airfoils and wind turbine blades. The placement of VGs on the airfoil successfully controlled the undesirable phenomena present in wind turbine aerodynamics. VGs also increased the static stall angle and maximum lift coefficient through increased mixing in the boundary layer. While the consequences of increased mixing are known, it is a result of the vortex created by the control device. The trailing edge shed vortex also prevents dynamic stall by breaking down the dynamic stall vortex on the suction side of the airfoil. Therefore, to properly implement the VG into the model, the magnitude of its effects must be accurately considered.

As the flow progresses over the vortex generator vane, the VG sheds a vortex with a strength of Γ. As the vortex travels along the surface and increases mixing, an equal reaction from the boundary layer viscous forces causes the vorticity to dissipate, characterized by a decay rate λ_{VG}. In a three-dimensional flow field, the VG-shed vortex also has a direction of travel in the plane of the airfoil's surface and interacts with vortices shed by parallel vortex generators. These parameters affect the magnitude of VG-induced mixing imparted on the flow, and each effect is significant enough to prompt individual analysis to understand cumulative VG performance.

In the initial attempts to calculate vortex generator effectiveness at delaying separation, Pearcey[48] utilized the vortex movement direction in the design, modeled by an analysis by Jones[62]. As the vortices travel along the airfoil, they induce a vorticity layer of opposite sign at the wall. This layer gains a vertical velocity, eventually moving the shed vortex to infinity. With the introduction of more than one VG vane, the behavior can change in exceptional cases. Due to adjacent vanes in a counter-rotating array, the vortices will first move downward before traveling away infinitely in the direction normal to the airfoil's surface. The vortex shed by the adjacent vane first induces a downward velocity, causing it to move closer to the wall and away from the neighboring vortex, where the influence from the induced vorticity at the wall will act the same as in the single vortex case. In a co-rotating configuration, the initial induced velocity is upwards, and the vortices proceed to infinity quicker. In his first considerations, Pearcey[48] proposed to limit this interaction by increasing the spacing between vanes in co-rotating VGs. Keeping the vortex as close as possible to the surface for the longest chordwise distance is very important to increase the effectiveness of mixing. Godard and Stanislas[49], and Pauley and Eaton[52] found that harnessing the neighboring vortex influence by decreasing the spacing resulted in a more optimal VG design.

While inter-vane-pair spacing is an essential aspect of the design, it is impossible to consider it in two dimensions. However, Jones[62] developed a function to include the influence of the path in the mixing term. Gould[63] built upon this idea to create a metric that measures the effect of VG-induced vortex path in evaluating VG effectiveness. This metric allows for relating the VG dimensions to the added mixing.

At its core, a vortex generator is merely a lifting surface in the boundary layer of the airfoil that induces flow mixing by exerting a tip vortex. Wendt and Biesiadny[64] and Wendt and Reichert[65] conducted extensive parametric studies to determine the behavior of the VG due to its dimensions. The work examined the initial vortex circulation and decay and how it related to the geometry of the VG and the flow conditions. The authors experimentally determined that the magnitude of the shed vorticity Γ correlated with the Mach number Ma, the VG angle of attack β_{VG}, and the ratio of the height of the vane to the height of the boundary layer $\frac{h}{\delta}$. They found the shed tip vortex to have a magnitude based on Prandtl's circulation about a finite wing, where $k_1 - k_4$ were determined based on a regression on the results obtained from the current VG setup.

$$\Gamma = \frac{k_1 \beta_{VG} u_e c}{1 + \frac{k_2}{AR}} tanh\left(k_3 \left(\frac{h}{\delta}\right)^{k_4}\right) \tag{3.5}$$

Dudek[66] applied this formulation for the VG magnitude to a Navier-Stokes computational model in several different flow cases. Comparing the results to fully-resolved computations and experimental data found that they generally agreed well, apart from the VG near-field. While this method can be accurate for some cases, its basis in the Prandtl equation does not account well for the physics. The improvement of the resulting circulation is based on experimental curve fitting, correlating the aforementioned variables by empirical coefficients.

To improve on this method, Poole et al.[67] hypothesized that lifting line theory could predict the vortex generator aerodynamics due to the simplicity of their design. While requiring slightly more computation, this directly considers the physics of vortex generators. The flow traveling along the boundary layer has a defined velocity profile that will cause it to experience a force upon reaching the VG. The lifting line theory is applied based on the method of Glauert[68]. Generally, the geometry of vortex generators tends to have a low aspect ratio; thus, Polhamus's theory[69] must supplement the lifting line theory by including the vortex that rolls up along the length of the VG. By averaging the velocity profile over the boundary layer, due to the requirement of uniform velocity, Poole et al. expressed the final circulation as a sum of lifting line theory and Polhamus' suction method.

$$\Gamma_{tot}(\theta) = \frac{4h\mu\beta_{VG} U_{VG} sin\theta}{\mu + sin\theta} + \frac{1}{2} U_{VG} l\pi \left(cos\beta_{VG}\right)\left(sin^2\beta_{VG}\right) \tag{3.6}$$

A subsequent validation against experimental data showed parity and a much lower standard error, which the authors found to be three times smaller than Wendt et al.[64]. A review into bound-circulation-based methods performed by Hansen et al.[70] confirmed

the belief that this was a valid calculation method. After proposal and validation, a vortex generator's circulation distribution could accurately yield its shed vortex's strength.

To observe the effects of vortices in turbulent boundary layers, Westphal et al.[71] experimented on a single vortex's spatial and temporal development. They found that the vortex core grew and deformed, resulting in the decay of vorticity over the chord. Kelvin's theorem states that the circulation around a closed curve in an inviscid fluid must be conserved. If this were true, the circulation of the vortices would remain the same as they convected downstream. Due to the viscous formulation, the vortex experiences a no-slip condition at the airfoil surface. The contribution of the wall shear stress along with interference between the neighboring vortices reduces the angular momentum of the vortices. Wendt et al.[72] investigated the decay of vortices for a counter-rotating VG setup. Starting from an initial decay rate, as the vortices moved upwards due to the induced vorticity layer, the decay rate decreased as well. In their review, Ashill et al.[73] concluded that the rate of change of vorticity is therefore proportional to Equation 3.7 with K as a determinable constant.

$$\frac{d\Gamma}{dx} = -KC_f \frac{\Gamma}{h_{\text{VG}}} \tag{3.7}$$

Lögdberg et al.[74] built upon the models of Pearcey[48] and Jones[62] to include this effect of decay. With the circulation set as an exponential function, the authors experimentally obtained the decay rate coefficients. This pseudo-viscous model adhered much closer to experimental results than Jones' original model. Manolesos and Voutsinas[75] apply this model to a three-dimensional separated flow, where it shows a close fit to the collected data.

3.3.1. UNSTEADY BEHAVIOR OF VORTEX GENERATORS

While vortex generators can prevent unsteady phenomena such as a dynamic stall, the discussion of the physics involved has so far pertained only to the steady case. The unsteady behavior must be analyzed to fully understand and accurately calculate the performance of vortex generators in a dynamic stall. Just like an airfoil experiences a change in flow and loading due to a step in angle or flow speed, so does the lifting surface of the VG. The flow conditions at the VG are vital when considering their effect during unsteady pitching. As the work aims to apply the outcome within the field of wind energy, it does not consider highly unsteady flows with $\kappa >> 0.05$. The viscous-inviscid formulation described in Chapter 2 also relies on this assumption to define the separation criterion.

Vortex generators are designed to be at the height of, or submerged in, the boundary layer. The analysis of their behavior is therefore completely confined within this environment. In a pitching motion of an airfoil, the leading edge moves laterally to the flow, leading to an induced velocity and resulting in changes to the boundary layer variables. While the entire airfoil would be moving in a given direction, including the VG, this velocity manifests only in the solution of the boundary layer. Ericsson and Reding[76][77] expand on this idea and conduct a thorough treatment of unsteady airfoil phenomena.

The current chapter found three measurements that quantify the effect of VGs: the strength of the shed vortex Γ, the rate of decay λ_{VG}, and the movement of shed vortices relative to the wall. With the analysis of the problem in two dimensions, a change to the VG effectiveness can only occur in the boundary layer. Thus, the model can characterize the unsteadiness experienced by the vortex generator through the changes in the velocity and momentum profiles of the integral boundary relations resulting from pitching and gusts.

The previous section found the flow velocity at the location to be a critical factor in determining the shed vortex's magnitude; the experimental analysis performed by Wendt et al.[64] and prediction based on the lifting line theory developed by Poole et al.[67] confirmed this. An unsteady viscous-inviscid model inherently considers the changing velocity profile due to the pitching airfoil with an unsteady boundary layer. With a flow condition of higher unsteadiness, calculating the vortex shed at the VG in steady conditions would capture the development of steady mixing but would not include expected phenomena such as lag. Capturing the transient behavior of the produced vorticity by the VG could be modeled similarly to an airfoil with a known incoming gust. Katz and Plotkin[15] treat a case of a flat plate in accelerating flow through a lumped vortex model. By drawing the parallel to the current situation, it is possible to include the effects of gusts with an iterating calculation of VG circulation. An intermediate approach to finding the transient performance without separate calculations is using the function developed by Wagner[78].

$$L' = \pi c \rho U_e^2 sin(\beta) \Phi(\tau) \tag{3.8}$$

where $\Phi(\tau)$ is Wagner's function that describes the development of this lift in time due to the unsteady flow, and can be expressed as:

$$\Phi(\tau) = 1 - 0.165e^{-0.041\tau} - 0.335e^{-0.32\tau} \tag{3.9}$$

This function's contribution can be evaluated in time from a series of steps in wind speed through the Duhamel integral. The evaluation of the aerodynamic characteristics of a vortex generator found that lifting line theory described it well. Given the proportionality of lift to the circulation, the Wagner function could describe the magnitude of the shed vortices in time by relating their magnitude to the changing flow velocity at the VG location.

Beyond the strength of the vortex, they also display properties of decay and direction. As the airfoil rotates, the viscous boundary layer rotates along with it. While the path the vortices take could change, this effect is deemed negligible due to the slight expected movement. Additionally, for a conventional setup with more than a single vane, the path is dictated mainly by the neighboring vortex[62]. In the steady case, the decay of the vortices relates directly to the skin friction coefficient and height. As the skin friction remains a parameter of the viscous-inviscid model, the development can be considered quasi-steady.

3.4. MODELLING VORTEX GENERATORS

The applications and benefits of incorporating vortex generators have been stated earlier in this work. Due to their widespread application in wind turbines for those reasons, vortex generators must be taken into account in the aerodynamic analysis at every step of the way for an accurate model. It is desirable to come up with an airfoil design that works well by itself and can harness the usefulness of VGs effectively. As the design process is iterative, one must balance the model's accuracy and efficiency to yield the best results at the lowest cost.

Vortex generators can most easily be included in the calculation by creating a flat plate protrusion at each VG element location. A CFD simulation of this type must be fully three-dimensional to account for both the shape and the forces exerted by the VG. With this method, the results obtained can closely match the experimental data[79]. Despite this, running a long and accurate numerical simulation is not conducive to the purpose of design. A more intuitive method must be applied to make accurate calculations.

Including a vortex generator in the flow without its geometry involves changing the flow relations to account for its effect. The first such model was developed by Bender et al.[80] and worked by representing the vortex generator as a lateral force. The lateral force was discretized over the mesh in the covered domain, acting as a source term. A force in the flow results in a gain of angular momentum, creating a vortex akin to the one created by a VG. Prandtl's lifting line theory dictates the magnitude of these forces based on the flow conditions. Jirasek[81] proposed an improvement to this model with regards to the positioning of this force. While the lift force can create the equivalent circulation due to the VG, this circulation can also be added to the flow directly[82]. Törnblom and Johansson[83] proposed modeling the increased mixing due to the shed vortices indirectly, achieving viable results. The mixing effect was modeled statistically through an approximation of the shed vortices within the Reynolds stress transport equations and showed the ability to mimic the significant flow features of VGs. The methods of VG modeling in CFD range from high fidelity, in the case of full geometry inclusion, to low fidelity and give insight into possibilities for modeling in a viscous-inviscid formulation.

As described earlier, a vortex generator releases a vortex in the streamwise direction, increasing the mixing in the boundary layer to energize the flow. In order to capture this phenomenon, the model must achieve the induced mixing at the location of the VG; Kerho and Kramer[2] propose a model based on this idea. Incorporating the VG on the airfoil surface is achieved through modifying the code by changing the stress transport equation. The shear stress term in boundary layer relations represents the stresses caused by the viscous interaction of turbulent flow. Previous research identified the mixing process as a result of the eddy viscosity of the turbulent flow. By combining these concepts, a modification to the shear stress term directly affects the flow mixing, thereby mimicking the behavior of VGs appropriately.

At the position of the VG, the rate of mixing is increased to a given value by a step, where it decreases exponentially downstream, corresponding to the decay rate. Daniele et al.[84] argued that this is not the best representation for vortex behavior and suggested a sine-exponential increment. They found good agreement with experimental results

and increased stability of the solver at higher angles of attacks. While a step increment is likely to cause issues with numerical stability, it has a better grounding in the physics of vortex generators. A smooth step function with strength $\sigma_{0_{VG}}$ and decay rate λ_{VG} is thus proposed by De Tavernier et al.[3] to represent VG influence better.

The VG sheds a vortex with a given magnitude, direction, and decay rate. The model aims to simplify these three variables into a function describing the evolution of mixing over the airfoil's surface. A numerical solution to evaluate the magnitude and decay of the mixing would require a significant amount of resources; thus current understanding of vortex generator performance has mainly been experimental. A numerical investigation by Shan et al.[85] describes energy and pressure fluctuations introduced into the flow by a vortex generator. Despite this, a generalization of the equations does not exist yet. The vortex strength decay can be measured and made into a relation between the VG measurements for a given setup; The work by Lögdberg et al.[74] features an example of this approach.

Within applications of this model, the shear stress term has been picked based on experimental data[2], a single VG setup of a single row of co-rotating VGs with an aspect ratio $AR = 4$, angle of attack $\beta_{VG} = 20°$, and spanwise spacing of heights. Calibrating the model to a single setup severely limits the breadth of application for their code. To account for different VG dimensions and types, de Tavernier et al.[3] proposed an engineering model based on an extensive experimental data set. They found that the average errors in lift coefficient and stall angle are limited, with good performance predicting steady separation delay. This model's benefit is its application to an extensively calibrated model with known limitations, XFOIL[25].

One can verify the effectiveness of any vortex generator model by examining for expected changes in the boundary layer variables. According to the theory supplemented by numerous experiments, at the location of the VG: the displacement thickness $\delta*$ must decrease, while momentum thickness θ and skin friction C_f must increase. Kerho and Kramer[2] verify this behavior by plotting the shape factor $H = \frac{\delta*}{\theta}$ and C_f against the chordwise coordinate, shown in Figure 3.3.

The authors validated the model by comparing the lift and drag polars obtained through the modified XFOIL code to experimental data for airfoil configurations with and without vortex generators. For a flat plate, the model performed well, accurately representing the $C_L vs. C_D$ curve with vortex generators. The model could predict the increase in the maximum lift coefficient; however, it underpredicted the drag slightly at lower angles of attack. Kerho and Kramer[2] note that this behavior is likely due to how the model includes VGs in the boundary layer relations. With this implementation, Daniele et al.[84] found no increase in drag at zero angle of attack. The error in drag signifies a requirement for a term to include the parasitic drag not captured by the increased mixing. For the case of an airfoil with thickness, the lift curve slope matched well, despite the slight underprediction in $C_{L_{max}}$. Together with the failure to capture the sudden drop in the lift coefficient at the stall point, these differences result from the viscous-inviscid interaction model in use, not the VG implementation method. While several methods for modeling VGs exist, including VGs through an artificial mixing term shows the most promise given

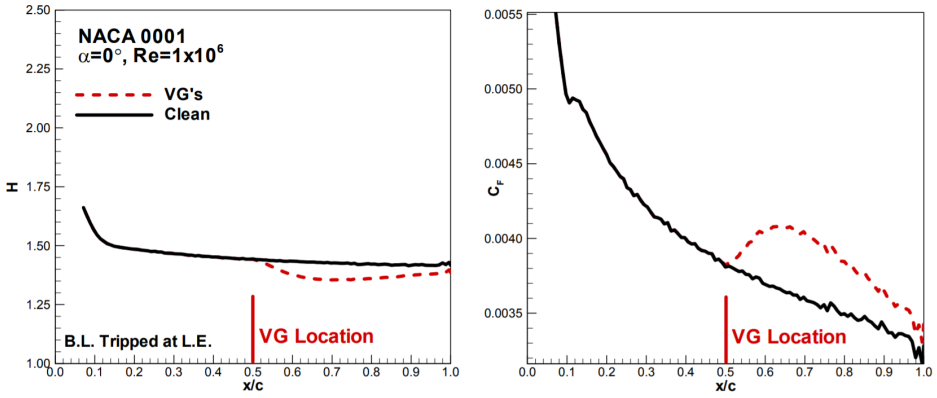

Figure 3.3: Effect of vortex generators on the shape factor and skin friction for a turbulent boundary-layer[2]

the limitation of the base viscous-inviscid interaction model. The results from associated papers show that the inclusion of this term achieves the desired changes in the boundary layer and allows for fast and relatively accurate simulation of VGs.

4

BASELINE VALIDATION OF THE EXISTING DOUBLE-WAKE MODEL

The following chapter investigates the accuracy of the baseline code written by Alessandro Zanon [1]. The program is a vortex panel method tool for calculating flow over an airfoil in a vertical axis wind turbine. It features functionality to accurately approximate rapid flow separation (dynamic stall) and subsequent reattachment. The code features an unsteady formulation for the inviscid solution for the airfoil and its surroundings and adds a secondary wake panel at the location of flow separation. While these additions allow for a more accurate flow prediction, they also introduce instability and potential errors to otherwise well validated steady single-wake panel methods such as XFOIL.

Running the code for several test cases, it became clear that the results obtained differed from the expected outcome in specific situations. The code tends to stop working or give nonsensical results if the timestep is set too low or high. While this is reasonable for any unsteady vortex panel method due to the characteristics of its formulation, the results also appear to be heavily dependent on the size of the chosen timestep. Therefore, this chapter will investigate the performance of each aspect of the code. Alleviating existing errors in the solution process, results, or stability through code alteration will also be explored.

4.1. SETUP

As mentioned before, a change in timestep can significantly alter the final results of a simulation, specifically when the angle of attack is in the stall region. Timestep choice is not the only factor that is capable of doing so. Thus, one must perform a sensitivity analysis for a few key variables to better understand their impact on the solution. Running the code for identical situations involving the same inflow conditions, angle of attack, and airfoil will achieve the necessary variation for a sensitivity analysis. Small changes in the solution method will be applied, and their influence on the overall solution will be

isolated.

Furthermore, to understand which part of the code these changes affect, the code will be validated step-by-step, starting from the most straightforward inviscid-only formulation, before slowly building up to an unsteady double-wake model experiencing dynamic stall. Starting from the earliest stage is crucial to ensure that the code operates reliably at its core and that its foundation can be trusted.

Validating the code in this situation involves comparing various outputs taken from the code. In a steady inviscid model, the timestep length should not affect the state the model converges to; thus, one should pick an output variable corresponding to the airfoil steady state. Reasonably, this leads to the coefficient of lift, a resultant value from the contribution of every panel on the airfoil and wake vortex blob. Upon enabling the boundary layer, further analysis of the model's performance can proceed by examining the boundary layer variables. A direct output of the boundary layer solver; these variables best indicate the model's performance. The validation will analyze the pressure coefficient (C_P) distribution in the absence of this data. The resulting parameters, such as the stall or laminar/turbulent transition locations, would indicate whether the current solution corresponds to reality.

4.1.1. VALIDATION DATA

Validation of the model will compare the results obtained from the program to other simulations and experimental data. While the model strives to recreate real-life flow conditions, no experimental data exists for comparison at its basic formulation of inviscid flow. The validation will have to take results from other validated simulations. XFOIL is chosen for this purpose, as its wide application shows the model to be reliable in its inviscid formulation.

The validation of the double-wake code will use experimental data, and as the code specializes in stalled flow simulation, the primary criterion is the ability of the model to predict deep stall. As the Zanon double-wake model seeks to improve the accuracy of existing models, it is stringent to evaluate how much the model improves accuracy over existing models. In a paper by Riziotis et al. [16], the authors validated their steady and unsteady models against experimental data obtained by Galbraith et al.[86]. The experimental data is collected for a NACA0015 airfoil at a Reynolds number of Re = 1,500,000 and a Mach number of Ma = 0.12. A steady and unsteady case with experimental data and data from another simulation makes this an excellent validation case.

The model will first be run in its basic form at every validation stage to check whether the obtained results correspond to the validation data. If the results are accurate, the validation will proceed with a further check if more data is available. If at any point, the results diverge from expected values or start to vary greatly depending on the input parameters, a sensitivity analysis will begin. Each variable will result in possible values centered around the expected optimal input. An aggregation of the results based on these input ranges in a table will yield a clear and concise information reference.

4.2. INVISCID MODEL VALIDATION

The aerodynamic model relies on the inviscid simulation of the airfoil to obtain its output values. Sources, sinks, and vortices over the airfoil body and in the wake induce velocities that sum up to the total airflow over the airfoil's surface. Boundary conditions relating to the physical problem are set, with no flow penetration through the airfoil's surface and conservation of circulation over a given volume. With the addition of these boundary conditions, solving the system of equations results in the magnitudes of the aforementioned sources, sinks, and vortices. When solving the aerodynamic problem with the viscous layer included, these relations build the base of the solution, and the equations resulting from this solution remain in the solution matrix. Model functionality is ensured by running the program without the viscous boundary layer for a range of angles of attack to collect a polar for the lift coefficient C_L.

4.2.1. STEADY C_L CURVE

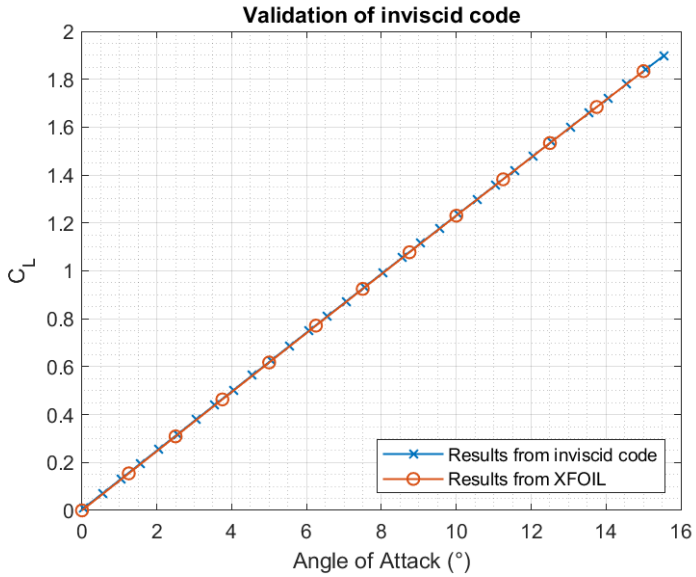

Figure 4.1: C_L vs. α for a steady airfoil in inviscid flow

The inviscid model validation examines the steady lift coefficient, as it is a derived value stemming from the entire solution. The lift coefficients of the current simulation and XFOIL are compared, as experimental data does not exist. As seen in Figure 4.1, the curves match perfectly throughout the entire range of angles of attack, indicating that the inviscid model is functioning correctly. The upper boundary of $\alpha = 16°$ signifies the stall angle, past which the results would not make any sense. The lack of a boundary layer in an inviscid model limits the comparisons between the two to the total vorticity (lift coefficient).

As XFOIL does not allow for unsteady simulation, the unsteady formulation of the inviscid code cannot be validated. Experimental data cannot be obtained for comparison, as an inviscid flow regime is non-physical. The unsteady performance of the code will have to be validated along with the boundary layer, as one can then compare the results to other programs and collected measurements from wind tunnel tests.

4.3. SINGLE WAKE VISCOUS-INVISCID INTERACTION MODEL VALIDATION

The validation proceeds to the viscous-inviscid mode with a validated inviscid formulation of the model. While solving for the viscous boundary layer gives results that represent real-life conditions much more accurately, it also introduces new possibilities for errors in the solution of the boundary layer, the coupling between the inviscid and viscous solution, and possible changes in the behavior of the inviscid code.

Single-wake viscous-inviscid models have seen relatively widespread use in the past few decades, and there is plenty of data to compare the results obtained from the current model. The double wake model builds upon the single wake formulation by introducing a change in vorticity over the stalled area and a shed wake from the separation point. By validating the single-wake part of the model first, one can assume the boundary layer solver to be working as intended, providing consistent output for a given input. If this aspect can be confirmed to be accurate, then a source of error resulting in a different output can be safely attributed to the given input and not to the performance of the BL solver.

Once more, the primary source of comparison will be the thoroughly validated program, XFOIL. The complete code simulates a two-dimensional airfoil in steady flow with an input Reynolds number. Typical for a viscous-inviscid interaction panel method, the code outputs both the inviscid and viscous solution results. Each of these can be compared individually to the results obtained from the current code to ensure similarity. The solution method between the two codes is very similar; however, not identical. While the general shape of the lift curve and the BL parameters should correspond closely, the formulation of the present code uses different simplifications in the discretization of the wake. At this level, results will be within a margin of error from experimental results, and any divergence from XFOIL's results does not necessarily imply a wrong model formulation.

4.3.1. CONVERGED STEADY RESULTS

The results to validate the single-wake model were obtained by reaching a converged solution for several given angles of attack in steady conditions. The simulation runs for unsteady conditions; however, it reaches a converged steady solution corresponding to the flow state given enough time. The range of angles in this comparison was chosen within the attached flow region, as the double-wake formulation cannot be turned off. Staying within the attached region ensures that only the trailing edge sheds a wake vortex, and a single vorticity distribution over the airfoil exists. The first step of validation is to compare the results from the current run to those obtained from experiments, XFOIL, and

the single-wake results from Riziotis and Voutsinas [16]. The observed variable, in this case, is the variation of C_L vs. angle of attack α. The experimental data originates from the report by Galbraith et al. [86]. It features a NACA0015 airfoil with a transition strip attached to the leading edge. Ensuring valid conclusions requires simulations according to these specifications in XFOIL and the current program.

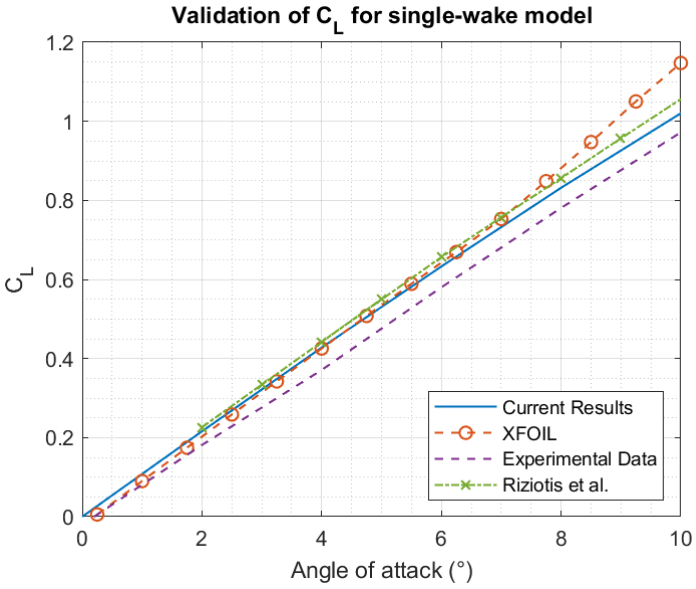

Figure 4.2: C_L vs α for a steady airfoil in attached viscous flow ($Re = 1.5 \times 10^6$, Ma = 0.12)

Figure 4.2 shows a plot of the C_L vs. α curve for the single-wake results from various sources. In the graph, the lift coefficient closely matches that of XFOIL until around $\alpha = 6°$. Every simulation overestimates the lift for the entire attached region compared to the experimental results. Beyond that point, the current model diverges from the results of XFOIL, verging closer to experimental results. The slope for the lift coefficient in XFOIL changes at around $\alpha = 7°$; however, this seems to be an artifact of the program's solution method and not physical, as the experimental results do not experience such a shift. One aspect to note is that both experimental data and XFOIL appear to predict a negative lift coefficient for $\alpha = 0°$. In XFOIL, this results from tripping the boundary layer at the leading edge.

The lift coefficient predicted by the current code is slightly smaller than that obtained by Riziotis and Voutsinas or XFOIL and closer to experimental results. This disparity is due to a difference in simplification used when discretizing the wake, resulting in a smaller predicted velocity at the TE, which thereby causes increased diffusion on the suction side, leading to a thicker boundary layer [1]. The boundary layer solution can be compared with the one from XFOIL to verify this statement, with particular attention drawn to the displacement thickness. BL variable analysis is also performed to ensure that the solution

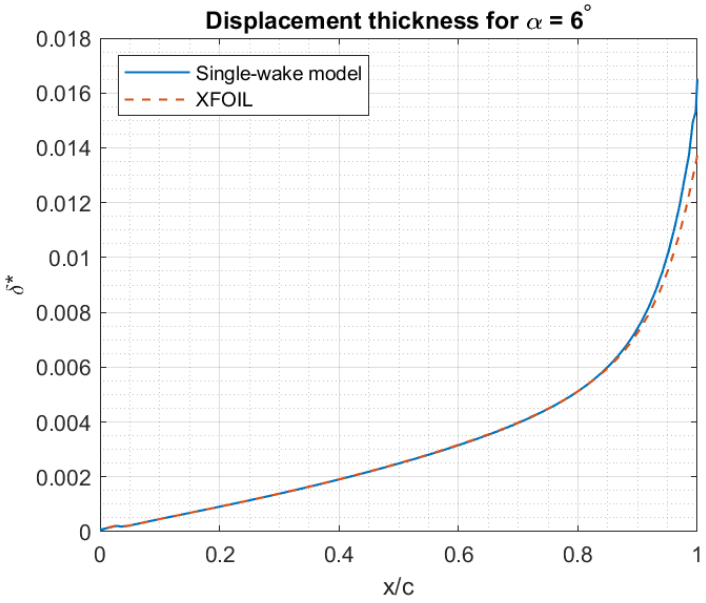

Figure 4.3: Displacement thickness variation over the chord for airfoil at $\alpha = 6°$

obtained does not merely result in the same C_L by coincidence.

4.3.2. BL PARAMETER COMPARISON

The analysis begins with selecting two angles of attack from the lift curve, one with a closely matching solution and one which gives seemingly different results. At $\alpha = 6°$, the lift coefficients predicted by XFOIL and the current run match closely, mirrored by Riziotis and Voutsinas's results. At $\alpha = 10°$, the solution differs significantly. BL parameter comparison at the chosen angle will give insight into the difference between XFOIL and the current code.

A leading edge transition is set ten nodes from the start of the boundary layer. A pitching airfoil changes the starting position resulting in a varying transition location; however, the point is always close to the leading edge. In the results from XFOIL visualized in Figure 4.3, the transition point is set to the same position for both simulations. The result is a graph of displacement thickness whose values are almost identical, apart from the slight difference at the trailing edge. This difference results from the aforementioned lower trailing edge velocity resulting from the wake discretization simplification. This difference, however, is not significant enough to impact the force calculation at $\alpha = 6°$.

Plotting the displacement thickness for an airfoil at $\alpha = 10°$ reveals the difference to be substantially different at the trailing edge. Defining displacement thickness as $\delta^* = \int_0^\delta \left(1 - \left(\rho u / \rho_e u_e\right)\right) \mathrm{d}\eta$, δ^* becomes integral function of the boundary layer edge velocity. The tangential velocity over the airfoil's top surface is plotted in Figure 4.5 to represent the discrepancy.

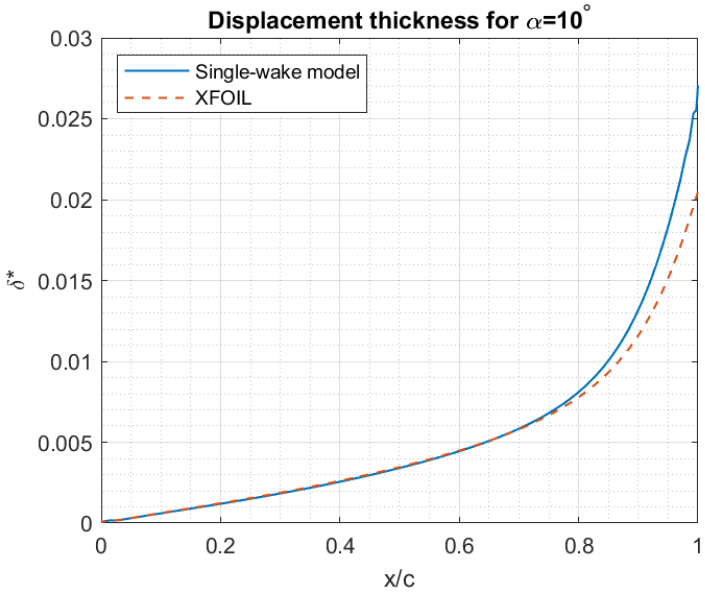

Figure 4.4: Displacement thickness variation over the chord for airfoil at $\alpha = 10°$

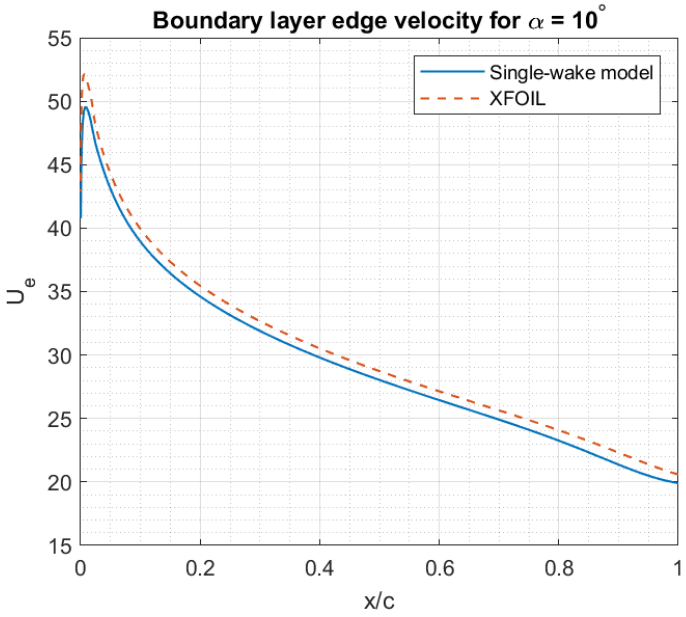

Figure 4.5: BL edge velocity variation over the chord for airfoil at $\alpha = 10°$

A lower velocity can be seen throughout the entire airfoil and not only at the edge. The offset makes sense, as a lower trailing velocity would also lower the velocity of all the air traveling over the top surface. Considering the Bernoulli equation used to calculate the force on the airfoil, a lower velocity leads to a higher pressure distribution on the top side. A decreased pressure difference between the suction and pressure side will thus result in a smaller lift force.

4.3.3. TIMESTEP VARIATION

Although these simulations are for steady flow and steady airfoil conditions, the simulation is unsteady and runs until convergence. A dependence on the chosen timestep was observed when looking at the converged value when running the simulation. The method of choosing the timestep aims to make the trailing panel approximately the size of the panels that make up the airfoil. Whereas geometrical coordinates define the airfoil's panel sizes, the trailing edge panel's length is defined as:

$$L_{TE} = (U_{up} + U_{low}) \times \frac{dt}{2} \tag{4.1}$$

For a given incoming wind speed, the velocity at the trailing edge will be approximately the same magnitude when the flow is attached. For picking an appropriate timestep size, one can make this assumption to simplify the process, resulting in $L_{TE} = U_{\infty} \times dt$. Here, the length of the trailing edge wake shed panel is linearly correlated to the size of the timestep. The resulting rule of thumb for picking the timestep size would be to divide the average panel size by the velocity.

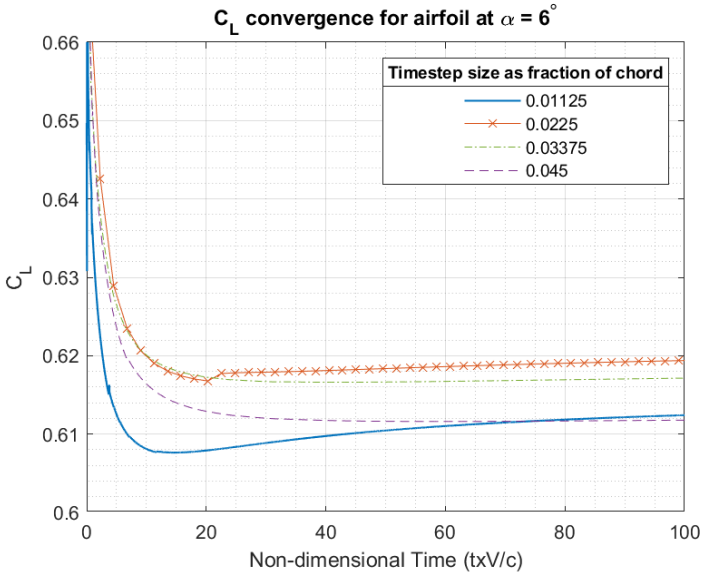

Figure 4.6: Convergence of C_L for airfoil at $\alpha = 6°$

Table 4.1: Table of converged values for airfoil at $\alpha = 6°$

Timestep Size	0.01125	0.0225	0.03375	0.045	Reference
Converged C_L	0.6132	0.6200	0.6174	0.6118	Experimental - 0.5760 XFOIL - 0.6512
TE Panel Length	0.0095	0.0191	0.0289	0.0383	Average Panel Size - 0.01

Figure 4.6 shows the convergence of the solution for the lift coefficient under the same flow conditions with varying timestep size, plotted against non-dimensionalized time. The graph shows a slight difference between the computed values at the different timesteps. Each simulation with a different timestep was initialized from the inviscid model after several thousand timesteps. As the timesteps themselves differed between the simulations, the total time the inviscid solution was allowed to converge for differs as well. The inviscid model is time deterministic, so less time to converge gives a lower C_L value. However, this does not change the solution, as the inviscid initialization aims to improve the stability and does not influence the viscous results. The final C_L value is recorded in Table 4.1, along with the trailing edge panel size. These values appear to be very close to each other at first sight; however, they follow a distinctive pattern. The lift coefficient reaches its maximum at a timestep of $dt = 0.0225(tV/c)$, with decreasing values at both larger and smaller timesteps. The existence of a maximum indicates the model converges to a value of C_L as the timestep magnitude changes. However, the difference between the results is relatively small; thus, the hypothesis cannot be confirmed without looking at more cases.

4.4. DOUBLE-WAKE STEADY VISCOUS-INVISCID INTERACTION MODEL

The double-wake model adds to the single-wake program by changing the formulation for the stall region in the inviscid solution. The functionality of this model remains the same before the airfoil enters a stall; once the separation of flow occurs, the system of equations changes. In the single-wake case, the vorticity distribution is constant over the entire airfoil. A double-wake model better predicts stalled flow by splitting the vorticity into two uniform distributions. One vorticity distribution accounts for attached flow on the pressure side and suction side before stall; The second vorticity distribution accounts for stalled flow from the suction side separation point to the trailing edge. Furthermore, a second wake is shed into the flow at the stall location through a stall panel.

4.4.1. CONVERGED RESULTS FOR STEADY AIRFOIL

This validation case is performed for the same validation data, extending from the first indication of a partial stall to a deep stall at $\alpha = 20°$. The experimental results were obtained by a pitch-up motion over a non-dimensional time (txV/c) of approximately 100. An airfoil pitched at this rate can be considered approximately static, giving a good range of results to compare.

In Figure 4.7, the code appears to capture the peak of lift at $\alpha = 14°$ quite well; however, it does not predict the sharpness of the subsequent C_L decline. Compared to XFOIL, it is

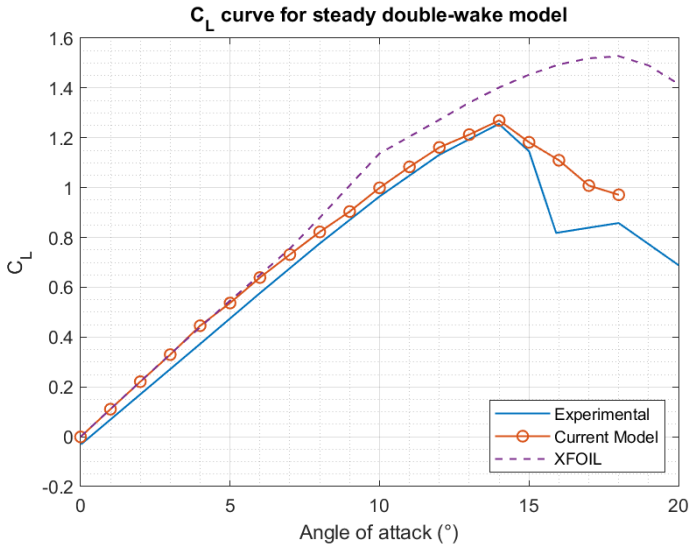

Figure 4.7: Plot of obtained C_L values over the entire range of angles of attack

clear that it performs much better at predicting the sharp drop-off in the lift at the stall point. The flow stays attached until the $\alpha = 14°$ mark, where the stall point suddenly moves up over the airfoil, and the lift drops off. While the simulation predicts the stall position at a reasonably accurate position, the code underestimates the effect of this stall and, as a result, overpredicts the lift.

While the airfoil is at a constant angle in the simulation, the model still simulates unsteady conditions. The previous case with an attached flow showed a dependence of the solution on the timestep. The solution converges well due to the definition of the trailing edge panel, as the relatively more stable flow conditions dictate the length and angle of the panel at the trailing edge. The velocity on both the upper and lower side of the airfoil differs only slightly from the upstream conditions. A constant solution is eventually reached with steady conditions and sufficient time.

With the introduction of the stall panel to the simulation, a steady solution becomes much less attainable. The stall panel's position, angle, and length are all defined by the flow at the stall location. Unlike the trailing edge, the flow of air over the midsection of the airfoil can be highly varying and is sensitive to boundary conditions. A strong feedback loop between the stall panel and changes in the flow develops, leaving no steady state to which the solution can converge. While this is visible to some extent with a light trailing edge stall, it is especially evident during a deep stall.

Taking the stall panel into account, choosing the timestep becomes slightly more complex. The timestep was previously chosen based on the freestream velocity U_∞, an acceptable estimate for the velocity at the trailing edge, and the length of the panel. However, these conditions are not the same at the stall position. For most thin airfoils, including the

NACA0015, the flow is faster by a small factor on the suction side of the airfoil, compared to U_∞. With traditional paneling methods emphasizing detail at the leading and trailing edges, a panel in the middle of the airfoil is generally longer than the panels on the trailing edge. The ratio of the panel sizes between the trailing edge and stall point would compensate for the difference in velocities between the points.

When the chosen timestep was small, the resultant stall panel length was also small. A shorter panel was considerably more susceptible to changes in the flow conditions. The resulting variation of the stall panel parameters manifested itself through an unnaturally large distribution of the calculated lift coefficient. On the other hand, when the timestep is too large, the stall panel remains stable, yet a reduction in temporal resolution results in a lack of formation of von Karman vortices. While the model gives much more consistent results, these results cannot be considered accurate given the absence of expected physical phenomena in the wake.

TIMESTEP VARIATION FOR RESULTS AT $\alpha = 14°$

Just as for the single-wake model, the double-wake model showed a clear dependence on the converged steady results based on the chosen timestep.

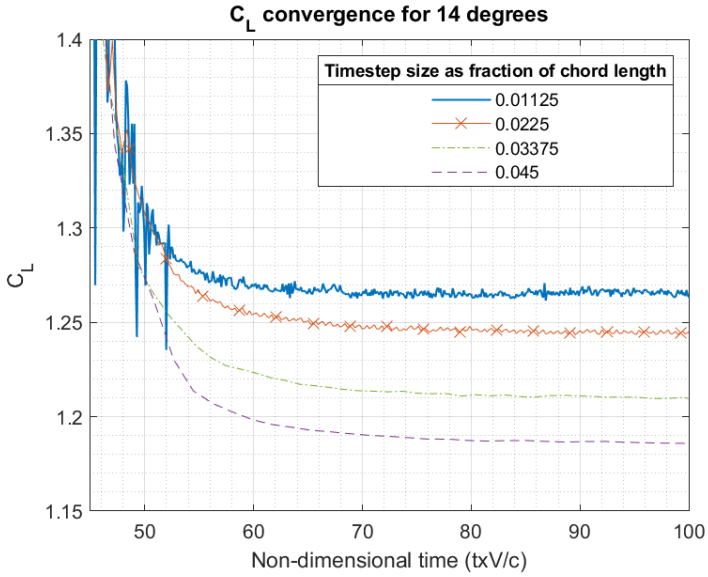

Figure 4.8: Convergence of C_L for airfoil at $\alpha = 14°$

The results in Figure 4.8 show the simulation's convergence to the steady value from the inviscid initialization. Similar to the single-wake model validation, the simulation was initialized for the first 4000 timesteps; however, the timestep difference resulted in a different starting time for each case. The initialization did not affect the converged value in the double-wake case either. In the stall region, switching from viscous to inviscid caused a sharp drop in the lift coefficient. The C_L curves are normalized to the same x-coordinate, highlighting the difference in the development of the value in time.

Table 4.2: Table of converged values for airfoil at $\alpha = 14°$

Timestep Size	0.01125	0.0225	0.03375	0.045	Reference
Converged C_L	1.2697	1.2455	1.2095	1.1852	Experimental - 1.256 XFOIL - 1.402
TE Panel Length	0.0046	0.0100	0.0156	0.0206	Average Panel Size - 0.01
Stall Panel Length	0.0054	0.0107	0.0161	0.0215	

Table 4.2 summarizes the exact differences between the simulations. The table lists the converged values of C_L and the length of the trailing edge and stall panels. The results indicate best adherence to the experimental data between timesteps $dt = 0.01125(tV/c)$ and $dt = 0.0225(tV/c)$. While both give results within a few percent of the experimental data, the trailing edge and stall panel size corresponding to the second timestep indicates a perfect match to the panel size of the airfoil's body. This change comes as a result of zero tangential velocity for part of the flow at the trailing edge and stall panel locations. Given this requirement for separated flow, the shed wake panel length is reduced by a factor of two in the double-wake case, leading to a different optimal timestep.

Unlike the results in the single-wake case, the graph shows a decreasing value of converged C_L with increasing timestep. Previously, it was concluded that a single optimal timestep gives the most accurate results, determined by going over a range of timesteps. Picking the timestep was proposed with two methods; finding a timestep as close as possible to the average C_L or continuously decreasing the timestep until the converged results show a peak. Whereas the differences between the results were definitively minor with an attached flow, the double-wake validation exposes a more significant difference between the timestep choice. While smaller or larger timesteps may give closer adherence to experimental data, it is not a consistent method of obtaining results. With that method, the timestep that coincides with ideal results for a given angle of attack may change as the angle changes. The increased noise seen in the results for the smallest timestep is consistent with previous deductions of increased stall panel instability with decreasing size. While the results fit well now, the possibility of increased noise in stalled cases casts doubt on the usefulness of these results. The largest timestep shows slight oscillation in the C_L value, indicating good stability, yet underpredicts the airfoil lift greatly. Choosing the timestep corresponding to the equal panel rule, a compromise between the two extremes is found, with minimal noise and a C_L closely matching the experimental value.

4.5. DOUBLE-WAKE UNSTEADY VISCOUS-INVISCID INTERACTION MODEL VALIDATION

Up to this point, the model has been validated for steady flow cases, converging to a single solution. The unsteady validation results are from an experiment performed on a NACA0015 airfoil at Re = 1,500,000, Ma = 0.12. The airfoil's angle of attack varies sinusoidally with an unsteadiness of $\kappa = 0.05$, a mean angle of attack $\alpha_0 = 11$ and an amplitude $\Delta\alpha = 8$. To verify the assumptions made about the selection of the timestep, this simulation was performed twice with a timestep size of $dt = 0.001s$ and $dt = 0.002s$,

corresponding to $dt = 0.0225(tV/c)$ and $dt = 0.045(tV/c)$ respectively.

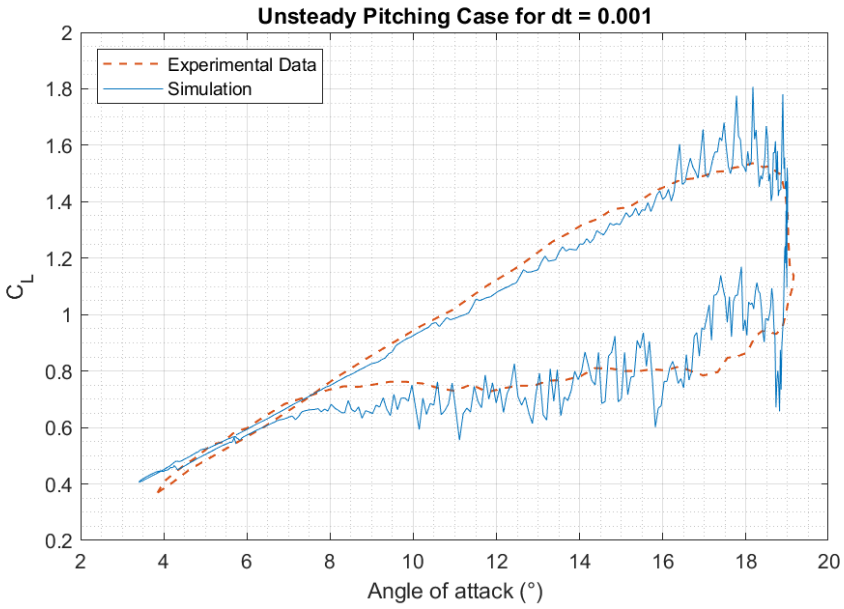

Figure 4.9: C_L results for pitching airfoil over a single cycle at $dt = 0.001s$ / $dt = 0.0225(tV/c)$

The two simulations do appear to give very close results to the experimental values. In both cases, the process of dynamic stall is captured considerably well. The lift curve slope is accurate, apart from slight underprediction in a partial stall, between $\alpha = 12°$ and $\alpha = 16°$. The leading edge vortex separation is predicted well in both lift coefficient and at the right angle of attack. Furthermore, the sharp drop exhibited by the experimental data is captured perfectly by both the smaller and larger timestep simulations.

While in the static case, the solution converged to the steady state, giving a constant trailing edge or stall panel length, in the unsteady case, this panel was continuously varying in length and orientation. As the goal of choosing the timestep was to bring it as close as possible to the average size of a panel on the airfoil, this was no longer a process that could be generalized. The most noticeable difference between the two simulations is the broader distribution of points for the simulation with the smaller timestep. While a perfectly sized panel gives results that correspond very well to experimental data, a panel that is too small tends to give chaotic results, which can be too small or too large.

In the simulation with $dt = 0.001s$, the results show closer adherence to the validation data. Throughout every part of the lift curve, the lift coefficient oscillates around the expected value with some uncertainty. While the results are not very precise, the accuracy appears to be relatively high, and one could deduce the general trend for the lift coefficient from the graph. In contrast, the $dt = 0.002s$ simulation results give a much more precise indication of the lift coefficient at any point. While the upwards motion and the leading

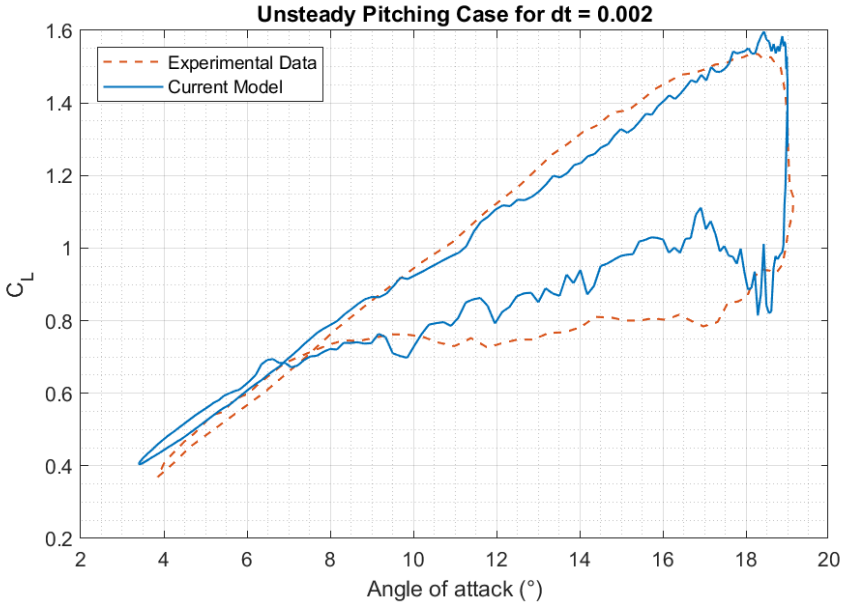

Figure 4.10: C_L results for pitching airfoil over a single cycle at $dt = 0.002s$ / $dt = 0.045(tV/c)$

edge vortex shedding appear to be modeled well, the simulation overpredicts the lift coefficient during the pitch-down motion and reattachment phase.

The conclusions provide further insight and confirm some of the propositions made about the timestep choice. It is also clear that timestep choice must follow a different procedure than the steady case, as now both the size of the trailing edge and stall panel varies over time. With a smaller timestep, the boundary layer is solved more often during the movement and gives results more closely corresponding to the experimental data. However, a smaller timestep also introduces instability to the solution as identified in the steady solution, where a strong feedback loop forms between the flow and stall panel resulting in significant variations in lift over a short period. A larger timestep ensures stability in the solution but is less accurate overall due to the loss of temporal resolution resulting in a non-physical solution. In some cases, when the timestep gets too large, the airfoil movement causes the boundary conditions of the boundary layer to change drastically. Significant changes in geometry between timesteps result in divergence of the boundary layer, and no solution can be output from the program. Therefore, the choice of timestep should be a trade-off between stability and accuracy, the result of a timestep too small and too large, respectively.

5

VALIDATION OF THE DOUBLE-WAKE MODEL FOR THE DU17DBD25 AIRFOIL

This thesis aims to implement the effect of vortex generators on the flow into the current working program. Thus a different dataset must be selected, which would allow for validation of the new portion of code. In order to get a thorough understanding of the capabilities and limitations of the code, it is essential to obtain both steady and unsteady results. The source of the experimental data is a recent paper authored by De Tavernier et al. [4]. This work investigates the effect of different types of vortex generators placed at varying chordwise locations on an airfoil's lift and drag characteristics. The resulting data consists of steady polars for the airfoil with and without VGs. It also contains different cases of an unsteady pitching airfoil with an attached and a stalled flow. This large and varying dataset will allow for the validation of the following:

1. Performance of mode for clean case, isolating limitations of the double-wake vortex-panel method
    - Attached flow
    - High angles of attack
    - Reattachment zone
2. Capability of simulating different types of VG setups
3. Ability to accurately simulate VG close to leading edge
4. Investigate the relation between unsteadiness and performance
5. Investigate the relation between Reynolds number and performance

5.1. EXPERIMENTAL SETUP

Evaluation of the performance of both the base double-wake model and the VG module will extensively use the results obtained from the aforementioned study. Therefore, it is imperative to briefly introduce the experiment's parameters and consider the origin of the results. While the paper published alongside the experimental data describes the experimental setup in more detail, the section below outlines the essential facts.

The experiment was conducted in the low-speed, low-turbulence (LTT) wind tunnel of the Delft University of Technology. With a maximum inflow speed of $100 ms^{-1}$, experiments can be performed for a chord-based Reynolds number up to Re = 3,500,000. Finally, a settling chamber that is 17.8 larger than the test area ensures steady flow, resulting in turbulence levels between 0.015% at $20 ms^{-1}$ and 0.070% at $75 ms^{-1}$. The wind tunnel test section is octagonal and has dimensions of $1.80m$,$1.25m$,and$2.60m$ for its width, height, and length[87].

As the experiment examines a broad range of variables that affect VG performance, it requires flow with a free and forced transition. In the latter case, a zig-zag tape forces transition at the $x/c = 0.05$ location near the airfoil's leading edge. Zig-zag tape is typical of such experimental setups, and its thickness measures at $t = 0.2mm$.

While the current chapter examines the ability of the model to replicate lift for a clean airfoil, the focus of this experiment is to investigate the capabilities of a VG setup to prevent a dynamic stall. The chordwise VG placement and two VG sizes constitute the dependent variables in this experiment, while the ratios of dimensions and angle to the flow are kept constant as a control. Baldacchino et al.[88] derive these dimensions through a VG dimension parameter study performed for thick airfoils, including DU17DBD25. The first VG setup (referred to as VG1) consists of two counter-rotating triangular vane-type vortex generators of height $h_{VG} = 6mm$, length $l_{VG} = 18mm$, and an angle of $\beta_{VG} = 15°$. The inter-vane distance of VG1 is $d_{VG} = 21mm$, and the inter-pair distance is $D_{VG} = 42mm$. The second VG setup (VG2) has the same shape; however, every dimension, excluding β_{VG}, has been scaled down by a factor of 1.5. An XFOIL simulation of the airfoil estimated the height of the boundary layer, which determined the height of the VG1 setup to match.

The authors obtained lift, drag, and moment coefficients through pressure measurements on the airfoil surface and the wake. A collection of 67 total pressure tubes and 16 static pressure tubes, called a wake rake, measures the pressure deficit in the wake, corresponding to the profile drag. Integrals of pressure measurements give the uncorrected lift, drag, and moment of the airfoil, which a wall-effect relation subsequently corrects for lift-interference, wake blockage, solid model blockage, and streamline curvature. The pressure measurements have a phase lag and amplitude loss for the cases with an unsteady pitching airfoil. An algorithm is applied to the experimental data and verified with a simple test case; the post-processing dramatically reduces the artifacts of dynamic pressure measurement. By removing these details in the transformation, the data loses its reference, and only the normal and tangential forces can be calculated.

Lastly, setting the airfoil to angles of attack in the range of $\alpha = -25°$ to $\alpha = 25°$ provides

the steady polars of the airfoil. The experiment defines dynamic pitching cases as an airfoil pitching sinusoidally around a mean angle of attack α_0, with an amplitude A, and frequency f:

$$\alpha(t) = \alpha_0 + A \cdot \sin(2\pi f t) \tag{5.1}$$

5.1.1. AIRFOIL GEOMETRY CHOICE

The airfoil chosen for validation of the model is the DU17DBD25 developed for Tulip Wind for use in wind-turbine applications; Figure 5.1 illustrates the coordinates of the test airfoil normalized to a chord of $c = 1m$. The airfoil design is a compromise between aerodynamic performance and structural integrity, capable of withstanding loads at the base of the wind turbine blade. Aerodynamically, the airfoil's design goal is a high power output in a wind turbine by maximizing the lift over drag slope.

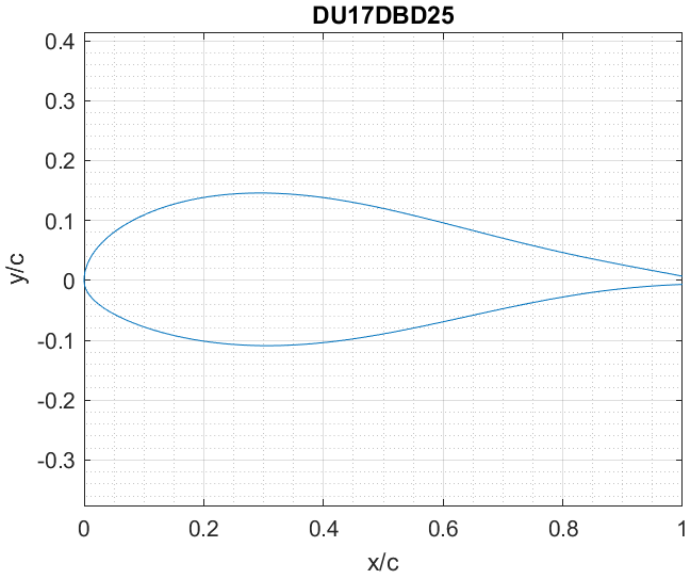

Figure 5.1: DU17DBD25 airfoil coordinates

The airfoil used in the experiments was a 3D-printed scale model with a chord of $c = 0.36m$. One important thing to note is that the model has a blunt edge of $\frac{t}{c} = 1.36\%$. While this is not a problem for physical measurements within a wind tunnel, vortex-panel methods cannot deal with a blunt edge without some modification to the boundary layer equations. As an example, to simulate blunt edges, XFOIL predicts where the upper and lower boundary layers would meet with a sharp edge and interpolates the velocity profile past the trailing edge [89]. While based on XFOIL, the current code cannot handle blunt edges, and the airfoil geometry must be modified to give any physical result.

While the gap at the trailing edge is relatively small, any changes in that area can tremen-

dously influence the solution. While the objective is to obtain a geometry with a closed gap, the changes must not affect the results unrealistically. With any change, however, it is expected that the predicted lift would decrease as a blunt edge tends to result in a significant increase in C_L within XFOIL [89]. Therefore, an approach similar to XFOIL's method of dealing with blunt edges is applied for the airfoil to stay reasonably the same. The gap in the airfoil was closed by extending the trailing edge sides to the point at which they meet, recreating the extrapolated shear layer method applied in XFOIL. Making the trailing edge shear layer physical keeps the geometry of the airfoil identical to a blunt edge case, with a smooth surface for the air to travel down the trailing edge and meet at a single point.

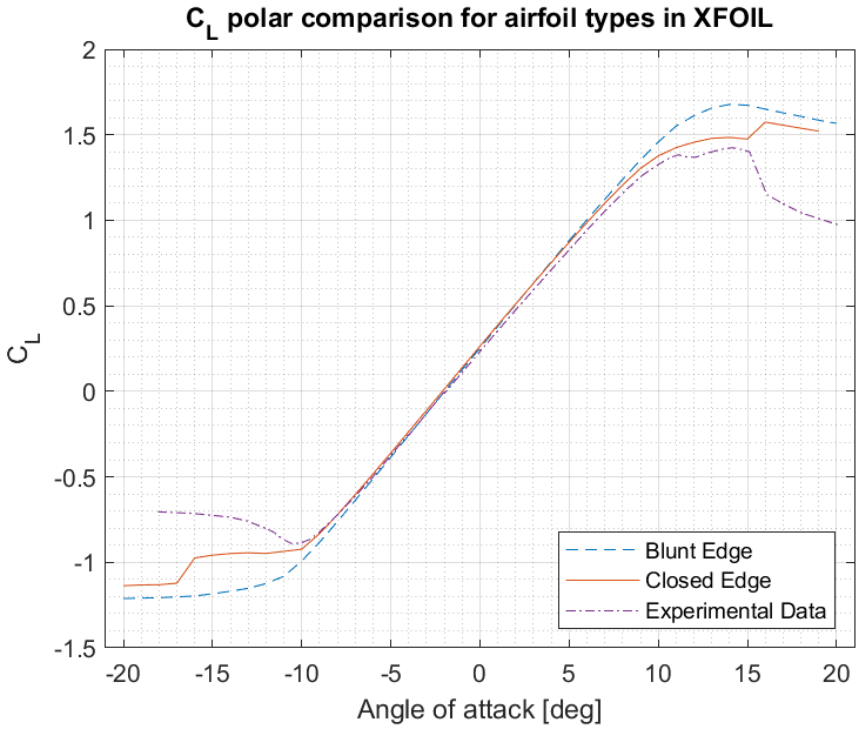

Figure 5.2: Comparison of lift coefficient of two different airfoil geometries in XFOIL

Figure 5.2 compares the lift coefficient of the blunt edge and sharp edge airfoils to the experimental data to understand the influence of this geometry change. Comparing the curves, it is clear that the two geometries yield the same results for attached flow at low angles of attack; however, the results diverge once the airfoil reaches an angle with partial flow separation. Here, the closed edge appears to better capture the real-life phenomena of the loss of lift near the stall point, with a substantial reduction in error.

Figure 5.3 compares the drag coefficient obtained in XFOIL from the blunt edge and sharp edge airfoils; the curves appear to be almost identical, with minor deviations towards

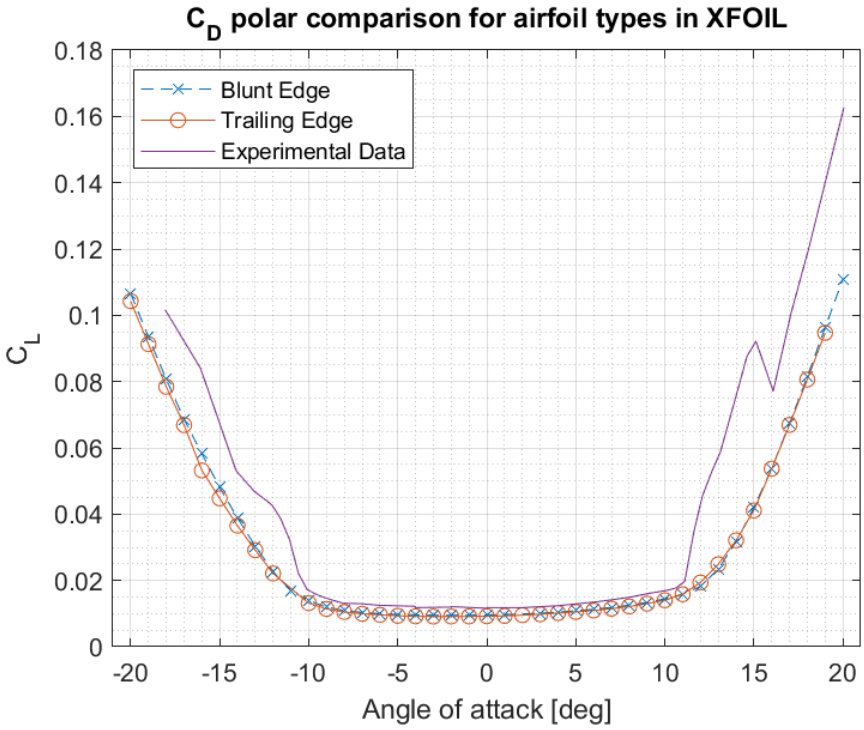

Figure 5.3: Comparison of drag coefficient of two different airfoil geometries in XFOIL

higher angles of attack. The difference between the XFOIL results and experimental data is much more significant than the difference between the two geometries, and so this difference resulting from the trailing edge geometry can be deemed inconsequential to the final results, as they are both underpredicting drag.

Looking at the results, while it is clear that there is a substantial difference in the lift coefficient resulting from the blunt edge, a sharp edge results in a lift coefficient resembling the experimental data much more closely. A better prediction of the lift coefficient indicates that the change in geometry is reasonable and physical. Furthermore, although the base double-wake model has no way of handling blunt edges, the XFOIL-based viscous-inviscid formulation suggests it will likely yield better results.

However, one crucial aspect to consider is that the airfoil increases in length by closing the gap in the trailing edge by interpolating the two edges. As the airfoil's upper and lower edges extend to meet, the airfoil chord increases to $c = 1.054m$. Despite the extended chord, the lift coefficient slope is identical to the blunt edge case, despite the two airfoils now having different lengths. The same resultant lift curve would imply that the closing of the trailing edge gap does not change the total lift at low angles of attack and that the added length insignificantly affects total lift.

With the current implementation of the model, the code can only simulate an airfoil with a unit chord, requiring x-coordinates that range $0 < x < 1$. The validation process also requires consistent results, corresponding to a consistent chord of $c = 1m$. With the addition of the sharp trailing edge, the coordinates would extend beyond the unit chord, and the airfoil must be scaled down to a chord of $c = 1m$ to ensure the model can initialize the geometry. As the airfoil cannot shrink in a single dimension without changing the airfoil characteristics, the y-axis must also scale with the same factor. Doing so changes the calculated lift by that same factor; however, the reduced chord should negate any difference in the calculated lift coefficient.

5.2. STEADY MODEL VALIDATION

With the unique geometry of the airfoil, the validation of the lift curve over steady conditions allows for an understanding of the capabilities of this program to model different airfoil designs. Furthermore, evaluating the difference between the obtained results to the experimental data will indicate the cases for which the model will underperform.

The steady curve was obtained experimentally by pitching through a range of angles of attack in a wind tunnel with a variety of flow conditions [4]. The extensive experimentation resulted in a coherent dataset; this validation will use it to evaluate the performance model in simulating this airfoil thoroughly. In the previous validation of the NACA0015 airfoil, there were only results available for a single Reynolds number with a forced transition. This validation process can therefore shed light on the relative accuracy of the model with a changing windspeed and transition criteria. For this process, the validation compares the following flow cases :

- Re = 1,000,000 Free Transition
- Re = 500,000 Free Transition
- Re = 1,000,000 Forced Transition

The model allows the flow to develop along the airfoil boundary with a free transition. As the velocity profile changes to satisfy the boundary conditions to end up with the solution, increasing instability in the flow triggers laminar/turbulent transition. An instability criterion calculated using the e^n method defines the location of the transition point. The transition location can be specified by node location or spanwise coordinate along the airfoil if a forced transition is required.

Figure 5.4 shows the steady lift curve for the base case of airfoil under Re = 1,000,000. The graph plots the lift curve from XFOIL alongside for comparison. The airfoil's C_L linearly increases until approximately $\alpha = 10°$ in either direction before stalling drastically and the lift dropping off at around $\alpha = 15°$. The model underpredicts the lift in the near-stall region, where the model becomes unsteady due to the iteration cycle of the stall panel. While the current model fails to capture that sharp drop in lift coefficient as seen in the experimental data, it performs better than XFOIL at estimating the lift drop-off. The model also appears to outperform XFOIL in both the positive and negative large angles of attack. The model's failure to predict a sudden stall was already noted in the NACA0015 validation case and appeared to hold for the DU17DBD25 airfoil.

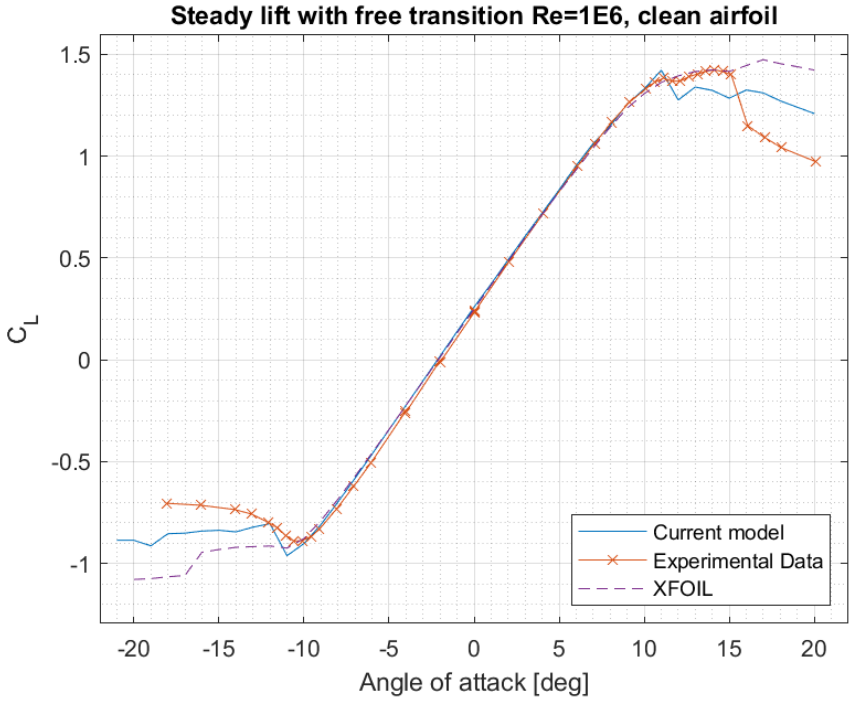

Figure 5.4: Steady lift curve for a DU17DB25 airfoil under free transition for Re = 1,000,000

Reducing the inflow speed by half lowers the Reynolds number to Re = 500,000, and Figure 5.5 represents the resultant lift coefficient curve. Here the same trend from the first curve can be observed, with a well-predicted lift until the near-stall region; the model's stalled region formulation causes a consistent underprediction in the lift coefficient compared to the experimental results. A sudden drop due to a stall fails to manifest beyond $\alpha = 14°$, and the curve slopes downward slightly instead. Compared to the previous graph, the model cannot capture the flow characteristics for slower flow well. This trend would imply that flow at a lower Reynolds number would be more challenging to simulate in the unsteady simulation and yield less accurate results.

With the transition of the boundary layer restricted to the front of the airfoil, Figure 5.6 shows a drastically different lift coefficient than the free transition case. This substantial difference means that any model would have difficulty simulating the substantial changes occurring in the solution of the flow. There is no stall of the airfoil in the traditional sense, with a sudden detachment of the suction side boundary layer; however, there are two sections of linear increase before and after approximately $\alpha = 7°$. While XFOIL manages to capture the general phenomena occurring at and beyond the non-traditional stall point, there is still a substantial error in the predicted lift coefficient, especially at large angles of attack. The current model fares better than XFOIL, as has been the case so far in every previous case; however, the simulation results still fall short of capturing the

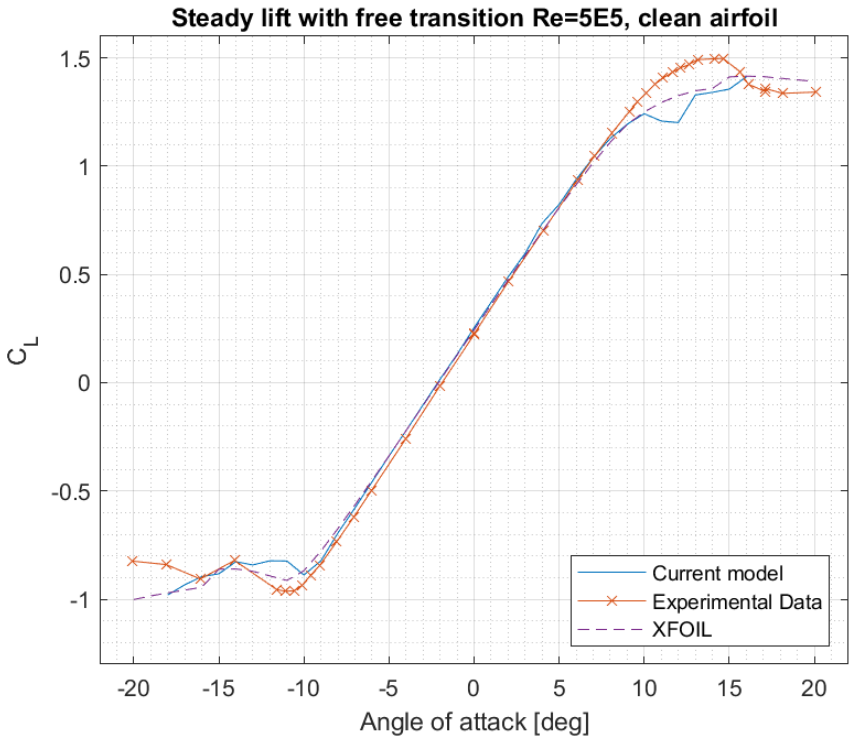

Figure 5.5: Steady lift curve for a DU17DB25 airfoil under free transition for Re = 500,000

complex shape of the experimental data curve.

5.2.1. UNSTEADY RESULTS FROM STEADY CASE

Just as before, while the steady simulation involves an airfoil at a constant inflow condition and angle of attack, the simulation must remain unsteady for the stall panel to converge to its final location. The converged solution is taken as the steady result for low angles of attack, as it is time invariant; however, closer to the stall angle, the stall panel solution becomes sensitive to the flow conditions and updates every timestep. The changes in the stall panel length, the circulation strength, the position on the airfoil, and its angle to the body cause sharp variations in the lift. As the solution to which the model converges is constantly changing, it does not diverge nor remain stable but can never reach total convergence either.

This particular airfoil geometry is particularly affected by this phenomenon due to the steep downward slope on the top side of the airfoil. The structural strength of the DU17DBD25 design lies in its thickness with a considerable camber, resulting in a substantial adverse pressure gradient. The quick advancement of the stall point over this area manifests itself in a highly mobile stall point which can oscillate over a range of positions

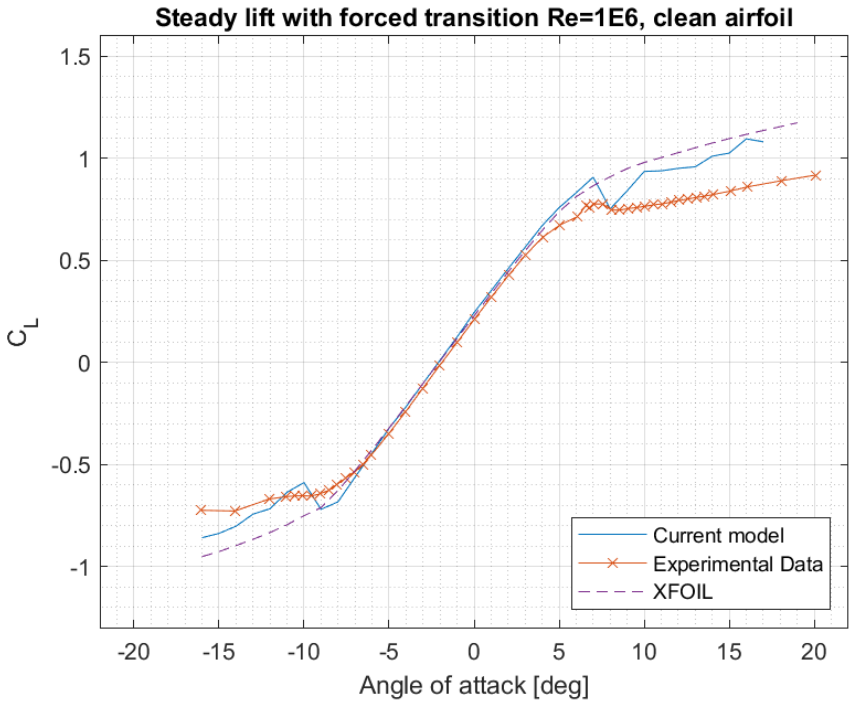

Figure 5.6: Steady lift curve for a DU17DB25 airfoil under forced transition for Re = 1,000,000

at a constant angle of attack.

While it is inherent to the solution method to experience some extent of oscillation in results, adjusting the timestep can control the magnitude of this oscillation. Whereas the initial validation identified that the timestep is related to the instability, validation on the DU17DBD25 airfoil shows that the stall panel is the primary cause of the instability, highlighted by the behavior in the near-stall conditions. The simulation is repeated for an airfoil at an angle of attack $\alpha = 14°$ for four increasing timestep sizes. While the NACA0015 validation highlighted these differences using the results' time development, the significant instability of the results for the smallest timestep results in a barely legible graph. Therefore, the investigation must take several approaches to assess the timestep-influenced instabilities in the solution.

Figure 5.7 visualizes the time development of the solution through a graph of lift coefficient versus non-dimensional time. The two extremes of timestep choice emphasize the effect of the timestep change. The curve with more noise corresponds to the simulation with a smallest timestep $dt = 0.001s$ ($dt = 0.015(tV/c)$), and the thicker stable line corresponds to the four times larger timestep $dt = 0.004s$ ($dt = 0.060(tV/c)$). The difference in timestep causes a variation in total simulation time; however, this does not affect the final result. Despite the noise in the results seen in the two extreme cases, both solutions

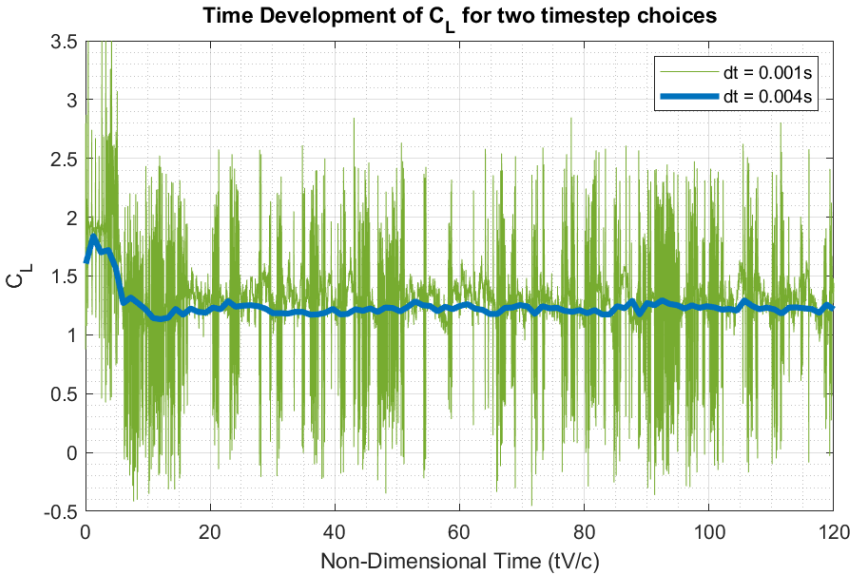

Figure 5.7: Time-Development of C_L for steady airfoil at $\alpha = 14°$ at two extremes of timestep choice

oscillate around a mean line. The differences are immediately visible from the axis scale, where the variation for the smaller timestep is significantly larger. When the stall panel position updates, the stall panel has to reach convergence in the new location, and the sudden movement results in unrealistic flow. The solution recovers after a few timesteps and continues towards convergence again. The effect of stall location recalculation is illustrated in Figure 5.8.

Seeing the large difference in C_L variation, the question of choosing the right timestep resurfaces. Whereas previously, a simple time average sufficed for the converged value, this is no longer possible. Taking the mean of C_L in time would include several instances of a non-physical solution and likely influence the final result. A noise of much lower magnitude in the NACA0015 case influences the timestep choice much less than in the current validation. A timestep that matched the defined stall panel criteria could be chosen, sized approximately the same as an average airfoil panel. Evaluating this criteria in Table 5.1, the optimal timestep appears to be between $dt = 0.001s$ and $dt = 0.0015s$. Since both of these timesteps result in the aforementioned noise in the solution, it is imperative to ensure a way to extract results in a meaningful manner despite the noise.

Timestep size	0.001	0.0015	0.002	0.004
Average stall panel size - 0.0106	0.0084	0.0126	0.0165	0.0322

Table 5.1: Table comparing the stall panel length for each timestep to the average airfoil body panel length

A correct solution should fulfill two more criteria besides a reasonable lift coefficient.

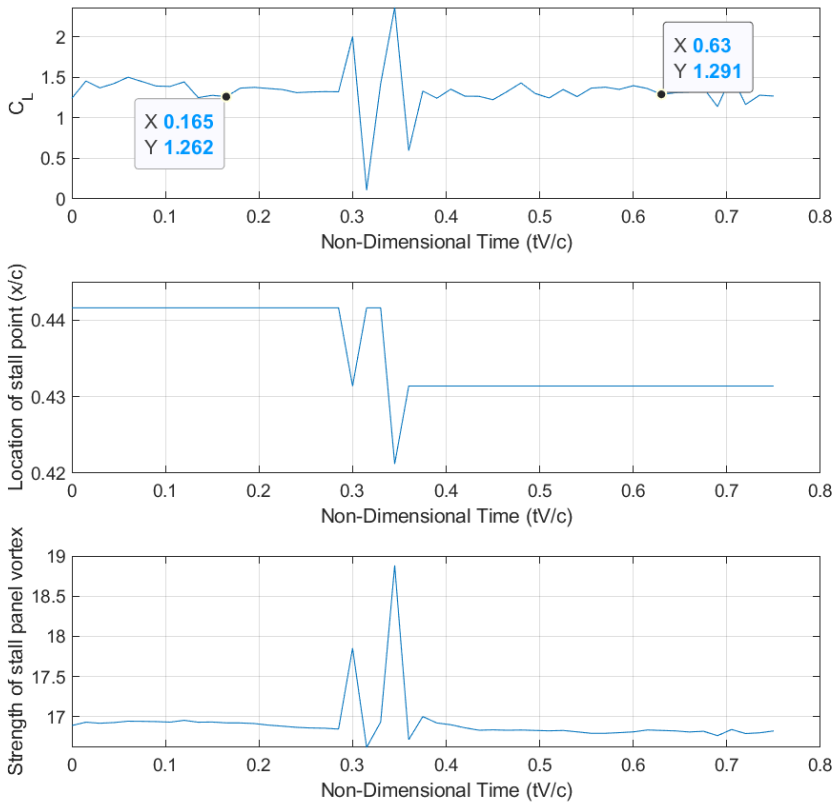

Figure 5.8: Stall panel location is recalculated during simulation of an airfoil at $\alpha = 14°$ with $dt = 0.001s$ / $dt = 0.015(tV/c)$

The boundary layer variables must have reasonable values; in this case, the pressure coefficient. The wake must also show physical phenomena expected of the airfoil. At $\alpha = 14°$, the airfoil has a significant portion of its chord in stalled conditions, which would result in discrete vortex clumps shedding from the airfoil composed of the individual vortex points shed by the stall and trailing edge panels. An increasing timestep size revealed that this phenomenon becomes less prominent. The vortex buildup is very apparent at low timesteps, as shown by a snapshot of the $dt = 0.001s$ simulation at an arbitrary point in Figure 5.9a. In contrast, the vortex shedding is completely missing in Figure 5.9b, where it appears the timestep is too large to allow for the phenomenon to show. This difference is likely the cause of a lower predicted lift coefficient, and its presence at the lower timesteps further reinforces their validity.

Finally, observing the pressure coefficient curve provides a final perspective on timestep

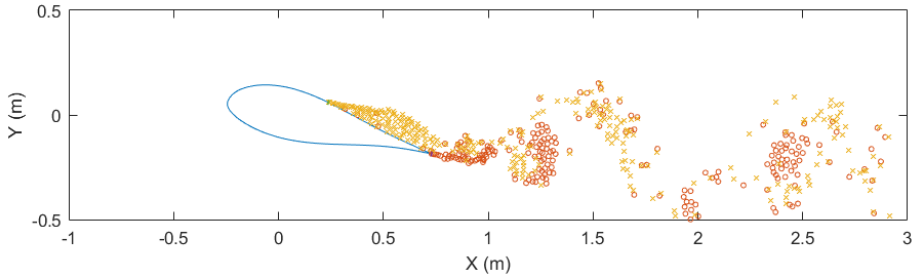

(a) $dt = 0.001s$ / $dt = 0.015(tV/c)$

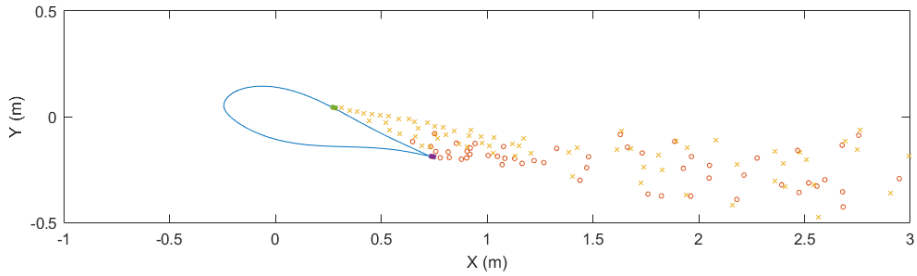

(b) $dt = 0.004s$ / $dt = 0.060(tV/c)$

Figure 5.9: Wake Vortex Development during simulation of an airfoil at $\alpha = 14°$, the circles and crosses represent those shed by the trailing edge and separation point respectively

choice.Figure 5.10 plots the pressure coefficient distribution for the two extremes of timestep choice; Figure 5.11 shows a plot for $dt = 0.0015s$, the optimal timestep based on the mathematical relation determined in the NACA0015 validation. The C_P curves from simulations of variable timestep all show an identical solution for the pressure side of the airfoil and the laminar portion of the suction side airfoil. After the transition, significant differences appear in the magnitude of the downwards slope, resulting from downwind interaction with the stalled flow. The simulations estimate the stall node close to one another, upon which a horizontal line indicates separated flow. The consistent development in C_P across the simulations up to separation indicates that the timestep does not affect the laminar or turbulent solution method; the difference can be attributed to the flow changes caused by the stall panel.

The dashed line in the figures represents the noise in the simulation with a 95% confidence interval, corresponding to two standard deviations. The simulation with timestep $dt = 0.004s$ lacked the necessary temporal resolution to represent the physical phenomena associated with a stalled flow. The lack of wake vortex interaction with the airfoil resulted in a C_P curve with little noise and a relatively flat shape. In contrast, a reduced timestep showed tremendous variation in C_p. While this is the case for both $dt = 0.001s$ and $dt = 0.0015s$, the confidence interval was much wider for the former. Lastly, the strong interaction between the small stall panel and the wake vortices result likely caused the mean value for $dt = 0.001s$ increases towards the trailing edge.

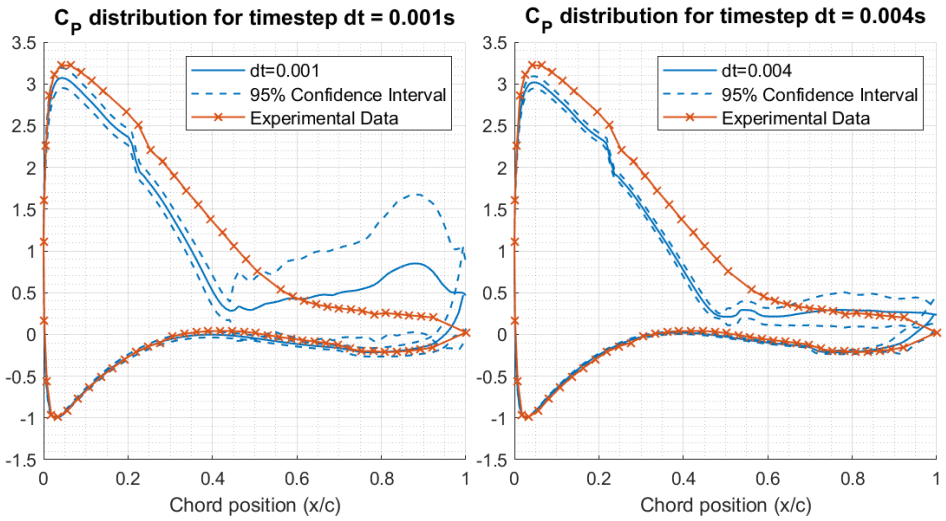

Figure 5.10: Pressure coefficient with 95% confidence interval shown in dashed lines for $dt = 0.001s$ and $dt = 0.004s$ for an airfoil at $\alpha = 14°$

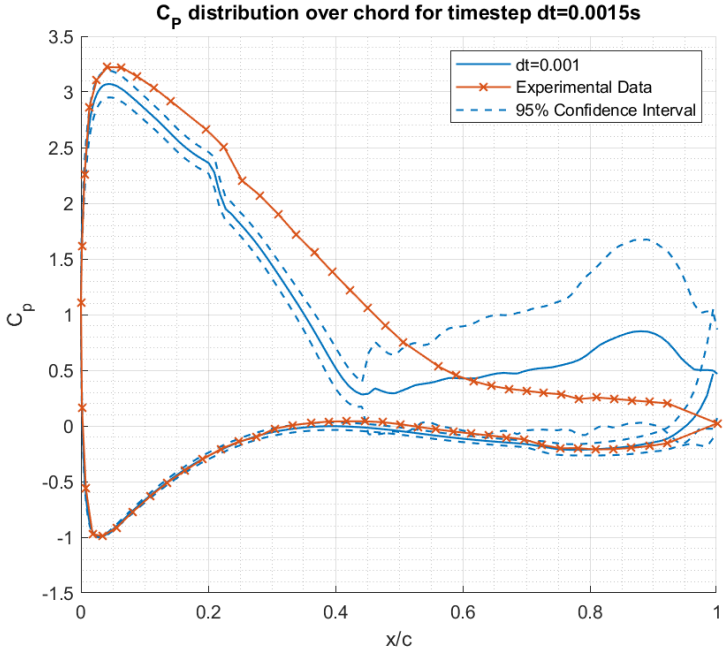

Figure 5.11: Pressure coefficient with 95% confidence interval shown in dashed lines for $dt = 0.0015s$ for an airfoil at $\alpha = 14°$

Table 5.2: Table of processed values of lift and drag coefficient at $\alpha = 14°$

	Arithmetic Mean	Normal Distribution	Filtered Arithmetic Mean	Filtered Normal Distribution	Filtered Voronoi Mean	Experimental Data
Lift coefficient (C_L)	1.3122	1.3055 ($\sigma = 0.0815$)	1.3113	1.3113 ($\sigma = 0.0815$)	1.2981	1.424
Drag coefficient (C_D)	0.0544	0.0544 ($\sigma = 0.0238$)	0.0587	0.0582 ($\sigma = 0.0214$)	0.0515	0.0781

Extrapolating on the previous findings of the NACA0015 validation reaffirms the choice of the timestep, and the working principles of the instability and the visual signs of either extreme are now better understood. When selecting the timestep based on average airfoil body panel size, it is vital to check whether the physical phenomena of flow separation seen in the real world are present in the simulation. However, a timestep too low also causes issues in the form of higher sensitivity, causing more extensive instability and leading to a more significant amount of noise in the data, adding to the effort required to filter it out. While this simulation is steady, a pitching airfoil might not allow enough time for the solution to converge. Thus despite appearing correct visually, it would not yield any meaningful results.

Based on this analysis, it appears that the $dt = 0.0015s$ provides a compromise between the two extremes. It has thus far been identified that any update to the stall panel position results in temporary noise in the data. Obtaining meaningful information from the simulation requires removing this noise or isolating the defining characteristics of the results. Applying the idea that the noise is predictable, a filter can exclude any values at the timestep of stall panel shift and temporarily after.

Using the scatter plot of the drag coefficient versus the lift coefficient is another approach, albeit with increased complexity. By taking a large sample of unsteady data, the goal is to find a single value to summarize the behavior of the airfoil under the given flow conditions. Figure 5.12 shows the scatter plot for $dt = 0.015s$. While filtering removes much of the outlier data, the distribution of these values still spreads wide. Therefore, it is insufficient to take a simple average of each of these values independently. A correlation between the lift and drag coefficients is observed in the scatter plot. It is clear that the two are related, and a point must exist at which both are correct simultaneously. The location of the highest point density is chosen as the solution, reasoning that the solution is oscillating around this center of convergence. A graphical method can be relied upon to obtain the lift and drag coefficients from this scatter plot.

Table 5.2 compares the results of both of these approaches to some basic methods. An arithmetical mean and a normal distribution are applied to both the filtered and unfiltered data to calculate the final value; the table also lists the graphical method results with the filtering applied. The final values differ very little, with the Voronoi method giving a slightly lower C_L and C_D. While the filtering removes much of the noise, the mean value obtained by the same method does not change, meaning the noise has no predilection for direction. While all of these methods underpredict the values of C_L and C_D, the values' consistency suggests the validity of any method. Given that the data filtering does not change the mean value, the reduced scattering provides better results for plotting and

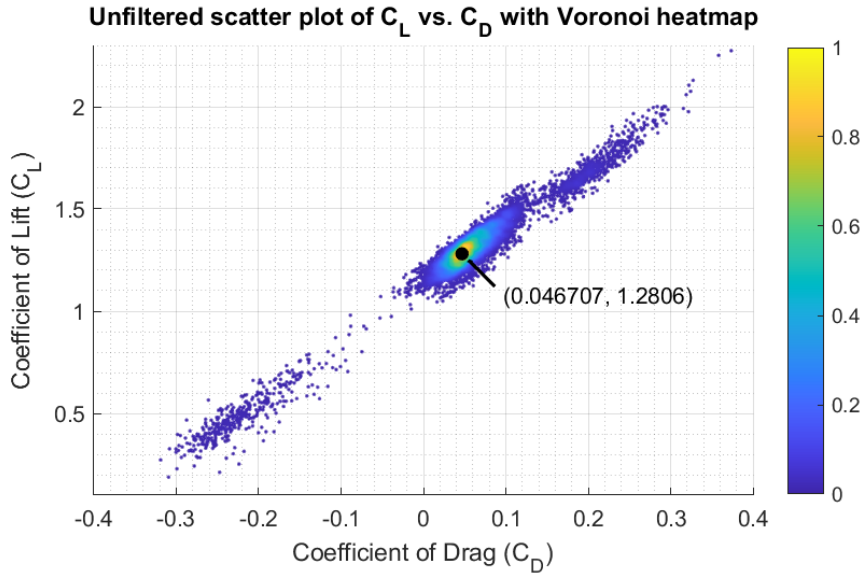

(a) Unfiltered results

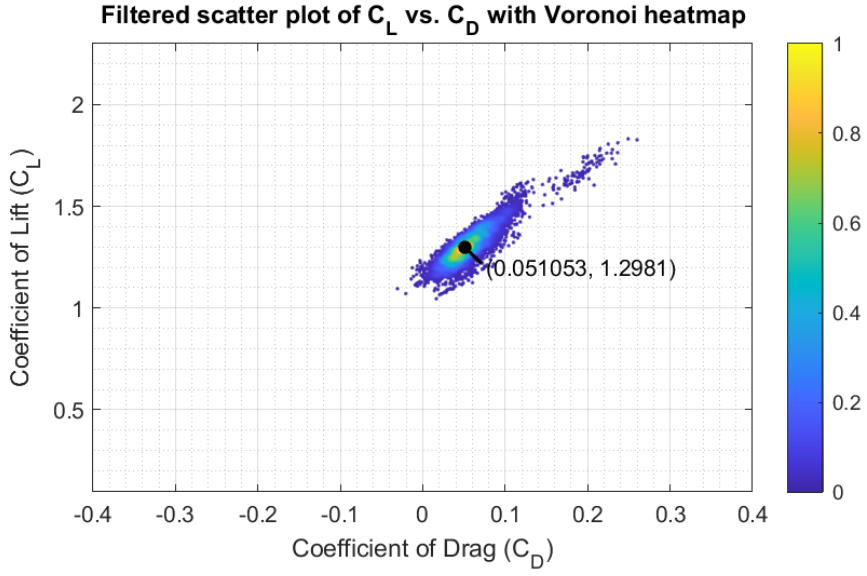

(b) Results filtered for sharp changes

.

Figure 5.12: Scatter Graph with Voronoi method for predicting the converged state of the solution at $\alpha = 14°$ with $dt = 0.0015s$

will be used in future pitching case graphs.

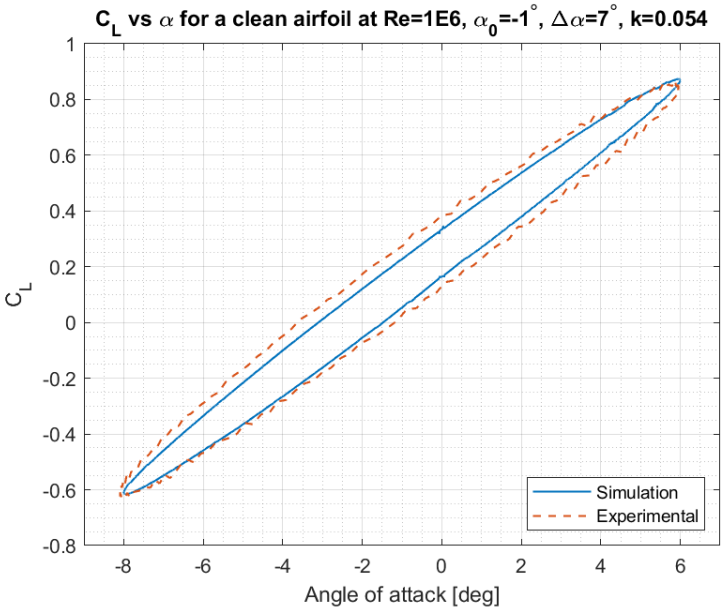

Figure 5.13: Results for C_L vs α obtained from the current program compared to experimental data, for $\alpha_0 = -1, \Delta\alpha = 7$,and $\kappa = 0.054$

5.3. UNSTEADY MODEL VALIDATION

With the steady performance of the model, in the simulation of the DU17DBD25 airfoil, complete and analyzed, the validation can proceed to the unsteady case. The dataset collected from the experiment performed by Tavernier et al. [4] includes variations in the reduced frequency of the movement, the Reynolds number, changes in the mean angle of attack, and the amplitude of its variation. For a valid comparison, the validation must consider the same cases for unsteady flow as for the steady results; Section 5.2 justifies the Reynolds number and transition choices. The model's shortcomings in each case should indicate the accuracy expected in the unsteady validation.

The experiment was performed with a model of chord length $c = 0.36m$, and the wind speed corresponding to Re = 1,000,000 was set to $U_\infty = 42ms^{-1}$. Thus an incompressibility assumption is reasonable, especially when the chord increases to $c = 1m$ and the simulation free-flow velocity equals to $U_\infty = 15ms^{-1}$. Whereas the NACA0015 validation included several timesteps, the sensitivity analysis findings obviate the need for simulations with variable timesteps. An optimal timestep is chosen based on the inflow speed $L_{TE}/L_{ST} = U_\infty \times dt$, where the length of the trailing edge and stall panels (L_{TE}/L_{ST}) match the length of adjacent airfoil body panels. The first case investigated was for an airfoil in a symmetrical pitching oscillation motion around a mean angle of attack of $\alpha_0 = -1°$, and amplitude of $\Delta\alpha = 7°$.

Figure 5.13 displays the curves for $C_L vs.\alpha$ from the current simulation results plotted

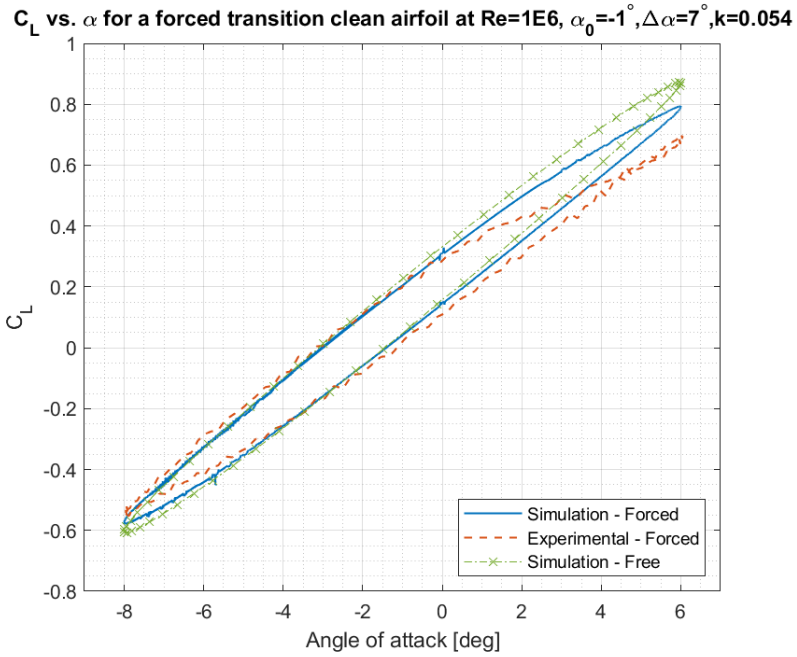

Figure 5.14: Results for C_L vs α obtained from the current program compared to experimental data, for $\alpha_0 = -1, \Delta\alpha = 7, \kappa = 0.054$, with forced transition at $x/c = 0.05$

against the experimental data. The two curves match reasonably well with the simulation representing reality quite accurately. Despite this, a slight difference in the width and slope of the hysteresis loop exists. When the airfoil is rotating clockwise, with the leading edge in an upwards motion, the model overpredicts the lift; the opposite is true for the counter-clockwise rotational motion, and the flow is underpredicted when the leading edge is moving downwards. The steeper slope and narrower width imply that the unsteadiness of the simulation is smaller than that of the experimental data, according to Theodersen's theory. An imperfect parity must be taken as a limitation of the model and considered when evaluating the results for simulation with vortex generators. Nonetheless, just as for the steady lift coefficient curve, the model matches experimental data sufficiently close, indicating it can likely predict VG-induced stall prevention.

Figure 5.14 plots the lift coefficient versus angle of attack for the experimental data for an airfoil under forced transition at $x/c = 0.05$, compared to the simulation results for free and forced transition. It is apparent immediately that the simulation fails to capture all the flow details, as the model overpredicts the lift coefficient at the higher angles of attack. However, by comparing it to the simulation with free transition, it can be noted that the solution is affected in the same direction. The experimental data showed that the lift coefficient curve forms an oval inclined shape that theory predicts for this type of movement for free transition. When the zig-zag tape triggers the transition, the lift coefficient above $\alpha = 0°$ changes in slope for the upward movement to converge with

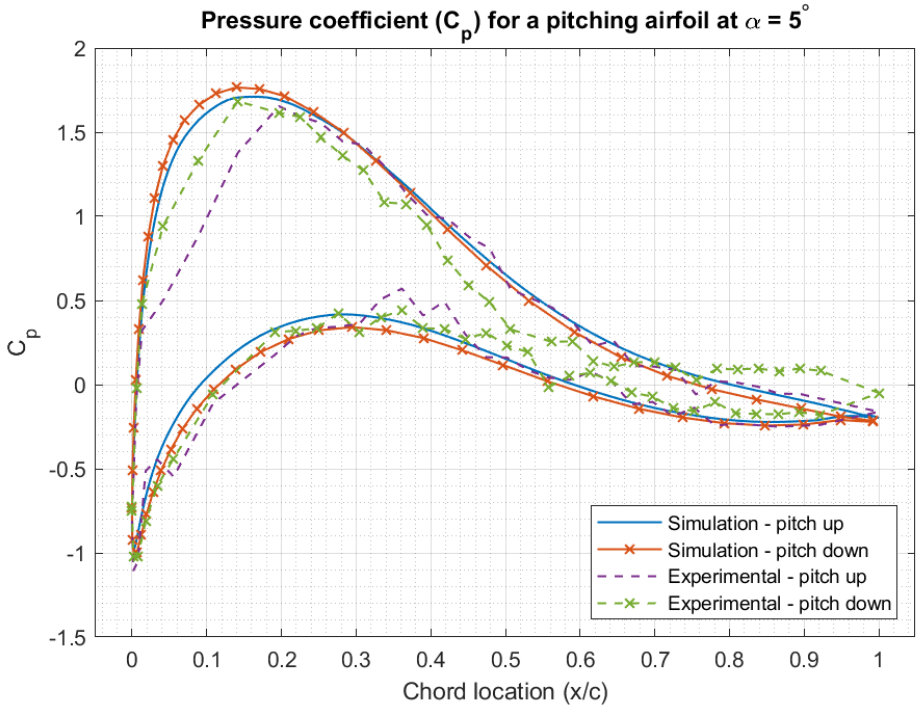

Figure 5.15: Pressure coefficient distribution for a pitching airfoil at $\alpha = 5°$

the lift in the downward motion. While the experimental data suggests a considerable reduction in C_L, the simulation indicates a similar trend when a forced transition occurs. The lift coefficient is approximately the same for the negative angles of attack yet drops a noticeable amount for the positive angles of attack. Based on this information, the pressure coefficient, C_p, must be examined to find the cause of the difference.

Figure 5.15 compares the simulation data to the experimental data for the pressure coefficient (C_p) distribution over the airfoil for the upwards and downwards tilting airfoil. The model captures the pressure distribution better on the upwards motion when the smaller pressure gradient promotes flow attachment. On the other hand, the model underestimates the effect of the increased pressure gradient on the downwards motion, thereby overestimating the lift. The flat section of the C_P in the pitch-down motion confirms the loss of lift, which originates from a partial flow separation near the trailing edge. With no enormous changes in the general shape of the C_P curve between the pitch-down and pitch-up case for the simulation, it can be concluded that the difference in the lift is a result of the pitching motion. A lack of partial stall in the pitch-down indicates the difference in the lift coefficient originates from the leading edge transition. Thus, while the code can reflect part of the expected change with a slight drop in the lift, it fails to capture the stall behavior in the forced transition boundary layer. Overall, the simulation struggles to predict the leading edge C_P shape and is less sensitive to flow separation.

Therefore, it is likely that an overestimation of the lift in forced transition cases will remain for the clean and VG cases.

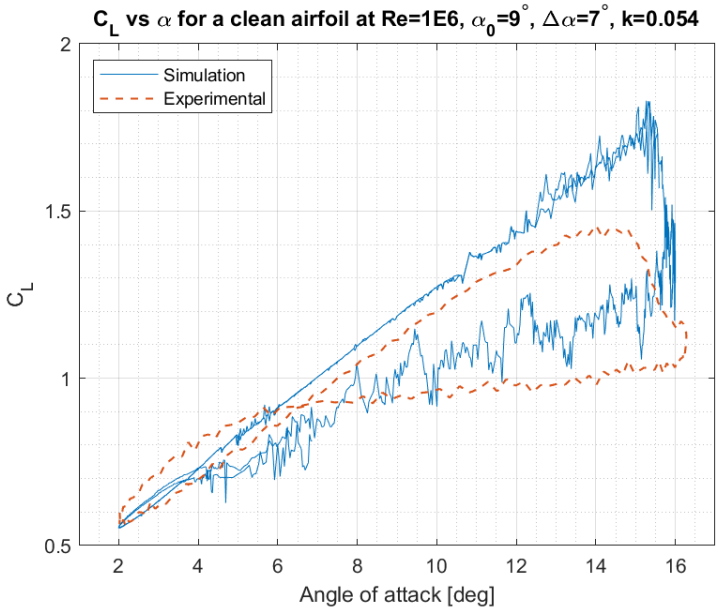

Figure 5.16: Results for C_L vs α obtained from the current program compared to experimental data, for $\alpha_0 = 9, \Delta\alpha = 7, \kappa = 0.054$

The results for an airfoil with an increased mean pitching angle and a constant amplitude and unsteadiness are plotted in Figure 5.16. Similar to the $\alpha_0 = -1°$ pitching case, the attached flow during the pitch-up motion of the airfoil overpredicts the lift by a small amount; however, this simulation indicates a different slope of the C_L curve as well. While the values are closer together for lower angles near zero, the difference increases with α. The most significant difference in C_L is in the shedding of the unsteady vortex that develops at the suction side of the airfoil, where the experimental data shows an earlier and more gradual decrease in the lift coefficient. The simulation predicts a later and much sharper drop in lift occurring at the maximum angle of $\alpha = 16°$. The earlier decrease in C_L in the experimental data indicates a dynamic stall vortex shedding while the airfoil was still pitching up. The current model did not recognize the airfoil's proclivity for complete flow separation. After separation of flow, the lift remains higher and slopes downwards much more than it should, staying separated until the very end of the pitch-down motion. In contrast, the experimental data indicates that the flow reattached at around $\alpha = 5°$, converging towards the regular hysteresis loop seen at lower angles of attack.

Whereas the previous pitching cases centered around $\alpha_0 = -1°$ showed minimal noise in C_L values, the large-scale dynamic separation of the flow yielded much less presentable results. The program recalculates the stall condition at every timestep, and the stall position shifts up if the C_f drops below zero in the boundary layer. Whereas the NACA0015

validation suggested this behavior, the relatively small peaks were attributed to wake vortex/body panel interaction. However, the geometry of the DU17DBD25 features a long section of negative slope on the upper side. A sizeable negative pressure gradient, seen in thicker airfoils, causes the point to move unpredictably to the sensitive nature of flow separation location calculation. The force calculation in post-processing includes a term referencing the value of change in pressure; a sudden change to this term over a timestep causes massive C_L spikes.

The analysis of this phenomenon for steady angles of attack found that a larger timestep resulted in significantly less response due to the change. The unsteady validation also showed smoother curves with an increased timestep. While a benefit of having a larger timestep exists, the timestep analysis proved that an optimal timestep exists for every inflow speed. Although increasing the timestep would reduce the noise, straying from the panel size-oriented optimal choice would give less accurate results. Therefore, a solution to the excessive noise in the results requires a different approach.

As the spike in pressure change happens with every update of stall position, it is possible to reduce the rate of occurrence by increasing the distance between panels in the region from the leading edge to the position of flow separation at a full stall. While this decreases the simulation's fidelity around the airfoil's half-chord point, the total accuracy of the simulation is not affected dramatically by the density of panels in this region. Applying this idea to the paneling method resulted in a less frequent occurrence of stall position shifting while also reducing the incidence of situations in which the stall position fluctuates back and forth under certain conditions. These findings suggest an airfoil paneling approach featuring a dense concentration of panels on the leading edge, increased panel size heading towards the center, and a slight increase in panel density towards the trailing edge. Notably, the aim remains to have the stall panel and the trailing edge panel be approximately the same size, at least within a certain margin; therefore, the panel cannot be shrunk too much towards the trailing edge.

The $\alpha_0 = 9$ pitching case was also simulated with a forced transition at $x/c = 0.05$, investigating the model's ability to account for this flow condition. For an attached flow, the model showed a shift in pressure distribution in the right direction, correcting the lift coefficient result. Figure 5.17 shows the results from the forced transition simulation; it is immediately apparent that the model struggles significantly to recreate the experimental lift curve for this case. While the graph roughly captures the curve's outline, the unconventional shape of the lift curve in the experimental data indicates that this is a highly complex case. With separated flow for the majority of the pitching motion and the $C_{L_{\max}}$ occurring at around $\alpha = 9°$, it is reasonable that the model would struggle to come close. An inability to predict this flow case is not a positive indication that the model can capture the phenomena in flow for forced transition at high angles of attack, for airfoil oscillations with high unsteadiness. These results could nonetheless prove to be somewhat valuable, as the simulation converged to a result and could prove helpful in an analysis of the relative impact of a vortex generator.

A reduction in the pitching motion unsteadiness from $\kappa = 0.054$ to $\kappa = 0.027$ is illustrated by a free transition $C_L vs. \alpha$ curve in Figure 5.18; α_0 and $\Delta\alpha$ are kept constant. In the

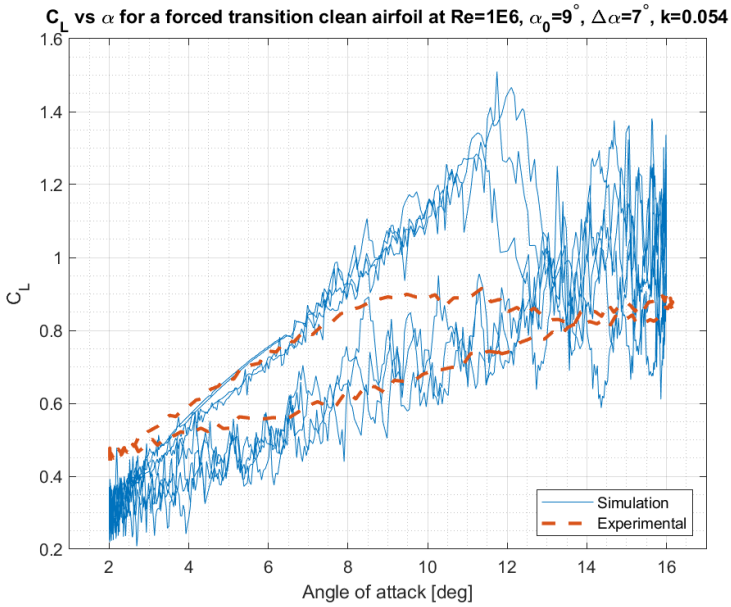

Figure 5.17: Results for C_L vs α obtained from the current program compared to experimental data, for $\alpha_0 = 9, \Delta\alpha = 7, \kappa = 0.054$, with forced transition at $x/c = 0.05$

case of a higher pitching unsteadiness, the model could not capture the early release of the dynamic stall vortex. The lower unsteadiness showed an increased parity with the experimental data, and the angle at which the experimental lift reached its peak matched perfectly with the location predicted by the model. Although the model was able to predict separation in the pitch-up motion, the sudden separation of the flow remained with a drastic drop in the lift from the stall angle onwards. The airfoil during the pitch-down motion shows improved performance as well, with the C_L in the separation region showing reasonable parity to the experimental data and the reattachment point predicted reasonably close. Despite this, the lift in the pitch-up motion remains overpredicted, and significant noise affects accurate readings near the maximum angle of $\alpha = 16°$. These findings indicate that the model can simulate unsteady phenomena in the quasi-steady range much better than a motion of higher unsteadiness.

Similar to the steady validation, the validation examines the results from an unsteady pitching case with a reduced Reynolds number of Re = 500,000. Figure 5.19 shows the plot of the lift hysteresis loop, where the mean pitching angle, amplitude, and unsteadiness remain at $\alpha_0 = 9, \Delta\alpha = 7, \kappa = 0.054$ for an apt comparison. One can immediately note the increased noise in the experimental data due to the pressure measurement method. Consistent with theory, the curve reaches a smaller $C_{L_{\max}}$, and the region of reattachment is shorter with the flow remaining attached for more prolonged periods per oscillation. Unlike the predicted outcome from the steady validation, the simulation results show significant parity with the experimental data. On the contrary, a lower Reynolds number

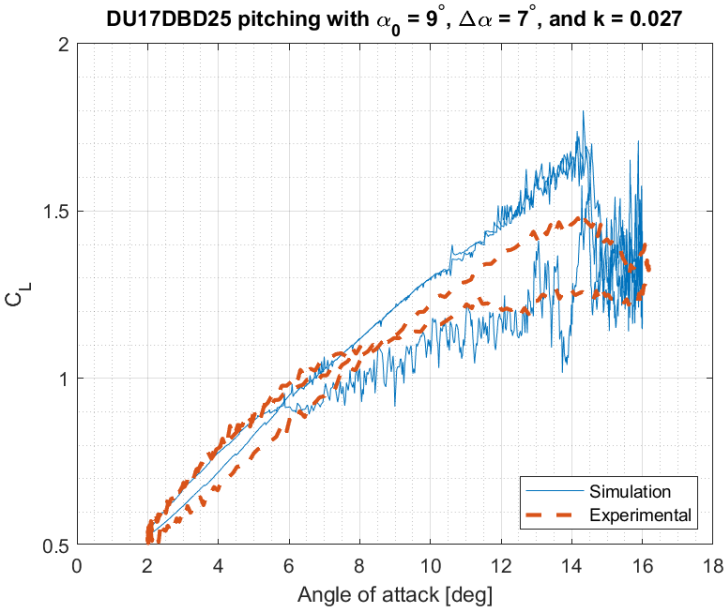

Figure 5.18: Results for C_L vs α obtained from the current program compared to experimental data, for $\alpha_0 = 9, \Delta\alpha = 7, \kappa = 0.027$

results in increased model performance, with a perfect capture of the maximum C_L and angle of stall α_S. The previously seen overprediction of the lift gradient disappears, and the lift reduction from a dynamic stall is captured perfectly. Despite this, reattachment of the flow still does not occur until the airfoil pitches down to $\alpha = 4°$.

Figure 5.20 shows the data for the simulation of an airfoil pitching around mean angle $\alpha_0 = -11$, with magnitude of oscillation $\Delta\alpha = 7$, and $\kappa = 0.054$. As the DU17DBD25 airfoil is not symmetric, unlike NACA0015, validation must be performed on the negative range of angles and the positive. Compared to the simulation performed for the positive angles, increasing the timestep found better agreement with the experimental data. With much less noise, a timestep three times larger than optimal was capable of approximating the reduction in C_L magnitude with a shedding dynamic stall vortex. However, in the interest of consistency, the validation analyzes the results of the timestep that fits the previously defined panel length criterion. While this introduces noise from the stall panel shifting in position, it is not as drastic as for the upper side; the absence of a significant negative pressure gradient did not require a re-paneling in the expected stall region. The lift curve slope for the attached flow region on the downward motion is matched perfectly by the simulation, however the model struggles more with the flow separation. Whereas the experimental data shows a gradual decrease in C_L magnitude, the simulation shows a rapid increase followed by a sharp drop. The graph shows the model capturing a stagnation of lift at the maximum angle of attack, albeit with a large variation in the value attributed to the noise resulting from complete flow separation. While the data

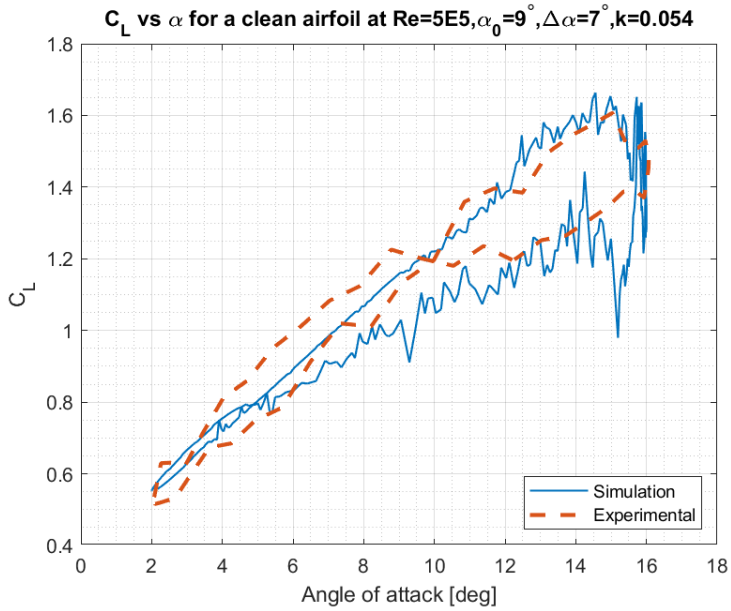

Figure 5.19: Results for C_L vs α obtained from the current program compared to experimental data with a reduced Reynolds number of Re = 500,000, for $\alpha_0 = 9, \Delta\alpha = 7, \kappa = 0.054$

indicates the lift slope flattens out after the separation point on the upwards movement, the model behaves as it did on the positive angles and predicts a slope for the separated part of the flow, indicating an inability to fully account for the reattachment of the flow, which also occurs much closer to the highest angle reached, later than experiments would indicate. While the simulation suggests the same errors present in the positive angles are also apparent in the negatives angles, better adherence to the lift slope should remain visible in the results with VGs.

Overall, the model indicates sufficient ability to capture the flow characteristics for unsteady oscillatory pitching motions of the DU17DBD25 airfoil. The model can predict the angle of a dynamic stall for highly unsteady cases within a small margin of error; when the unsteadiness of pitching is reduced, the model's results improve. The model nonetheless struggles with the reattachment of the flow and underpredicts the stall in that region consistently, with the flow not reattaching until reaching the end of the pitch-down movement. Forced transition at the leading edge affects the solution significantly, where the model cannot mirror the increased proclivity for flow separation present in the experimental data.

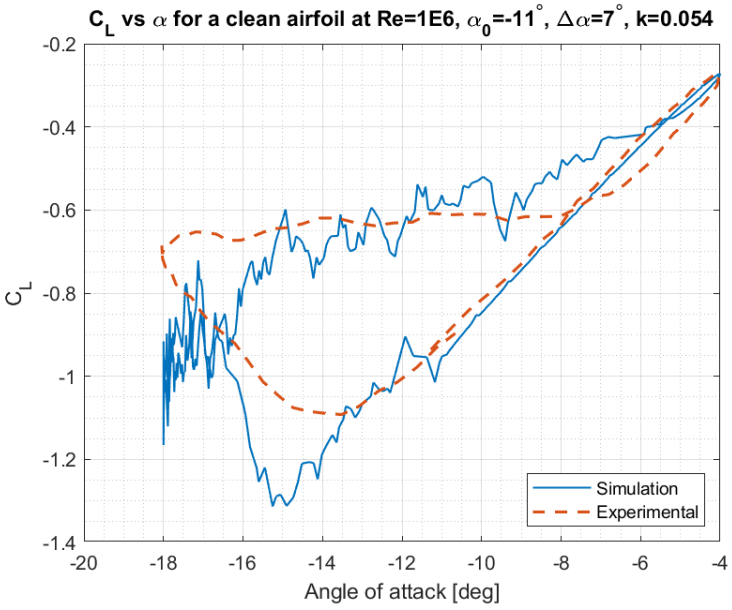

Figure 5.20: Results for C_L vs α obtained from the current program compared to experimental data, for $\alpha_0 = -11, \Delta\alpha = 7, \kappa = 0.054$

6

IMPLEMENTATION OF VORTEX GENERATORS TO MODEL

The previous chapters discussed the effects of vortex generators on the boundary layer flow and the methods of simulating them. The model was then validated for a base case to confirm it works as intended; validation continued for the cases corresponding to the new dataset with the DU17DBD25 airfoil. With the understanding that the model can simulate the new airfoil reasonably well, the next step requires the addition of VGs to the formulation. Conclusions are drawn from the simulation outcomes, investigating whether the approach gives sufficiently accurate results. This chapter will discuss the method chosen to simulate VGs and its implementation in the model.

6.1. BACKGROUND AND APPROACH

Extensive knowledge of the current model allows for choosing a method to simulate vortex generators. Section 3.4 listed and discussed the existing VG simulation methods and their strengths and limitations. A two-dimensional model cannot possibly represent the geometry of a three-dimensional VG, so the implementation must focus on its effects on the flow. Due to the nature of a vortex-panel method, the VG also cannot be represented by its equivalent lift force acting on the flow. Therefore, the method of choice must include the VG-induced mixing effect on the boundary layer. While several existing propositions to achieve this exist, the recent work of De Tavernier et al.[3] showed promise in a simple alteration to the XFOIL code, which is the basis of the program referenced in this thesis. While a shear source-term approach is simple in theory, the benefit of using the aforementioned work is the extensive calibration of its source-term magnitude function. Validation of the function on a large airfoil dataset allows the current report to focus on implementing and validating this code within the unsteady double-wake model and comparing its results to the experimental data.

The theory behind VGs and their effect on the flow are discussed more thoroughly in

Chapter 3, and this chapter will focus on source-term methods. A VG works by introducing a vortex to the flow, mixing it up. The associated boundary layer variables of shape factor (H), momentum thickness (θ), displacement thickness (δ^*), and skin friction coefficient (C_f) then change accordingly. Kerho and Kramer [2] initially proposed a method of simulating VGs through an artificial increase in mixing at the VG location, which showed promise in the results obtained. Instead of simulating the geometry, force, or vorticity introduced by the vortex generator, emulating the VG-induced shear source-term changes would result in identical changes to the BL parameters. However, it had its limitations in applicability based on its calibration for a single VG design and the simplified nature of the shear term addition. With this idea, De Tavernier et al. [3] developed a program that allows for broader applicability. A semi-empirical approach found a correlation between several variables and the airfoil lift.

The authors obtained the source-term strength $\sigma_{0_{\text{VG}}}$ and its decay rate λ_{VG} through calibration against a broad range of experimental measurements and high-fidelity numerical simulations. The chosen calibration data spanned a variety of VG configurations, airfoil shapes, and inflow conditions; as the model is based on XFOIL, evaluating the VG module's performance in unsteady flow is impossible. In order to calibrate the model, the authors first obtain airfoil performance for a range of $\sigma_{0_{\text{VG}}}$ and λ_{VG} values; then, they determine the required combination of source-term parameters to obtain the relative improvement seen in the reference data. This process intrinsically accounts for the base error of the model.

Research into BL effects of VGs indicated an exponential function as the best representation of its mixing effect; Figure 6.1 shows an example of such a function. It was found in the research that the strength $\sigma_{0_{\text{VG}}}$ and decay λ_{VG} of the shear source-term do not matter individually and that a correlation exists between the boundary layer changes and the integral of the exponential curve corresponding to the energy input per unit chord to the system by the VG. Thus the decay rate was set as a constant, and the solution process only involved solving for the strength term of the exponential function.

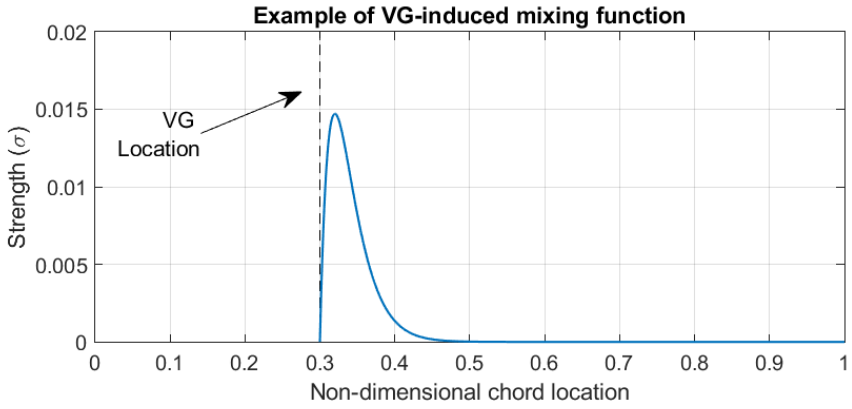

Figure 6.1: Example of exponential function starting at $x = 0.3$

The effect of the simulated vortex generator appeared to only change the flow parameters in terms of the source-term integral (I_{ST}); the relation to find this term was found based on several datasets using the following formula:

$$I_{ST} = C_0 \cdot \left(\frac{h^*_{VG}}{l^*_{VG}} \right)^{C_1} \cdot \left(l^*_{VG} \cdot \sin \beta_{VG} \right)^{C_2} \cdot (U_{VG})^{C_3} \tag{6.1}$$

where the semi-empirical coefficients are $C_0 = 0.0240$, $C_1 = 0.2754$, $C_2 = 0.4507$, and $C_3 = 0.2987$.

The source-term integral therefore depends on the non-dimensional parameters of the VG, where h^*_{VG} represents the VG height scaled by chord, l^*_{VG} denotes the VG length, and β_{VG} is the angle of the VG to the flow. While the previous three terms are inputs to the model, the final term depends on the boundary layer solution at the VG location, with the U_{VG} representing the BL flow velocity at the height of the VG. This velocity is found at the location of the VG using Swafford's velocity profile formulas [27], detailed in Appendix A. Relying on boundary layer variables to define the VG-induced mixing term means that the value of this term must be calculated within the boundary layer solution loop and repeated for every iteration. The definition of the source-term integral is:

$$I_{ST} = \int_{x_{\mathrm{VG}}}^{c} \left(\sigma_{0_{\mathrm{VG}}} (x - x_{\mathrm{VG}}) \cdot e^{-\lambda_{\mathrm{VG}} (x - x_{\mathrm{VG}})} \right) \mathrm{d}x \tag{6.2}$$

As the rest of the variables are known or assumed, the strength term $\sigma_{0_{\mathrm{VG}}}$ can be obtained inversely.

$$\sigma_{0_{\mathrm{VG}}} = \frac{2 / I_{ST}}{\lambda_{\mathrm{VG}} \cdot \int_0^1 e^{\lambda_{\mathrm{VG}} (x - x_{\mathrm{VG}})} \mathrm{d}\left(\frac{x}{c} \right)} \tag{6.3}$$

The strength and decay of the exponential function define the VG influence by the mixing induced at any streamwise airfoil coordinate. As the VG only affects the turbulent boundary layer, the associated closure equations must be modified to reflect that. Changes in the shear-stress coefficient would achieve the goal of increasing the mixing at the desired location. In the XFOIL formulation, which relies on turbulent flow theory by Green et al. [28], the shear-stress term C_τ is the instantaneous shear-stress coefficient, and the rate at which it changes is:

$$\frac{\delta}{C_\tau} \frac{\mathrm{d}C_\tau}{\mathrm{d}\xi} = 4.2 \left(C_{\tau_{\mathrm{EQ}}}^{1/2} - C_\tau^{1/2} \right) \tag{6.4}$$

This relation exists to simulate the lag in the flow shear-stress, as is observed in real-life conditions. Stresses in the boundary layer respond slowly to changing conditions; thus, adding the VG term directly to the C_τ would bypass this relation and potentially destabilize the solution. The term to change would therefore be the equilibrium shear-stress coefficient $C_{\tau eq}$, amended by adding the VG-induced mixing term S_{VG}:

$$\sqrt{C_{\tau_{EQ}}} = \sqrt{\frac{0.014851\,H^*\,(H-1)\left(H-1-\frac{18}{Re_\theta}\right)^2}{(1-U_s)\,H^3}} + S_{VG} \tag{6.5}$$

The equilibrium shear-stress coefficient is considered a fundamental closure term of boundary layer solvers and is often tuned to obtain better results, as seen in RFOIL[29]. Adding the VG influence at this location would not interfere with any of the preexisting and proven solution methods used in XFOIL, merely changing the constants to reflect the existence of a vortex generator at the location of higher shear stress. A sudden change in the equilibrium shear stress would allow the flow to respond naturally to the change and converge to a stable solution.

6.2. IMPLEMENTATION

While the existing double-wake model is similar in its base functionality to XFOIL[25] and VGFOIL[3], the previously described methods apply to steady, single-wake simulations. However, while the inviscid solver is unsteady, the boundary layer solver remains fully steady. A steady boundary layer requires no changes to achieve the same solver functionality with VGs as without them. VGFOIL works by implementing VG functionality to the base code by adding a dedicated module activated during the boundary layer solution at the location of transition and beyond. The same principle applies to the double-wake model, and an amendment of the boundary layer solution procedure can achieve the simulation of VGs.

As previously stated, the source-term equilibrium shear method for simulating VGs requires calculating the vortex strength based on the expected influence on the flow and the addition of that vortex term to the BL parameters. In the original paper, De Tavernier et al. [3] make changes to XFOIL in the boundary layer function to achieve this. The authors implement the VG influence by calculating the vortex strength at transition in function ***XBL*** and adding the vortex influence in function ***BLVAR***. The remaining changes in the code were made to the input and plotting functions, ensuring the full functionality of the application. As the current program does not contain inherent plotting functionality, the only additional changes must be in the specification of input variables for the VG specifications. The new variables that describe the VG location, length, height, and angle are added to the input file and propagated in the code through the required functions.

The model achieves the necessary boundary layer solution changes by introducing two new functions. The first function, ***VG_INIT***, calculates the strength of the exponential VG source-term; the second function, ***VG_CALC***, uses that amplitude to calculate the VG influence at any streamwise coordinate. The equilibrium shear-stress function takes this VG term as an input, which is added directly to the magnitude. With this term containing the entirety of the VG functionality, no further alterations are necessary for the solution method.

In real-life applications, a vortex generator only works by mixing up the turbulent flow and can trigger transition artificially by inducing instability in the flow. While Chapter 3

investigated the phenomenon of VG-induced transition, it is assumed for the time being that any vortex generator with a non-zero height in a laminar flow will trigger a transition. From earlier evidence, this assumption is valid for any vortex generator designed to increase the stall angle and maximum C_L. While studies show that micro-VGs effectively limit dynamic stall phenomena when placed on the leading edge, research suggests that the working mechanism is a 3D vortex interaction not present in a two-dimensional simulation. Given the inability to simulate micro-VG phenomena, vortex generators that cannot promote transition are beyond the scope of this tool. The initialization function ***VG_INIT*** runs at the node following the VG streamwise location. The model evaluates the laminar/boundary transition outside of the boundary layer solver; if the transition location is more aft than the VG location, the transition point moves to the VG location. Due to the calculation method of the function amplitude, the initialization function can only run at the VG location due to the inverse integration required to find the exponential function amplitude. The ***VG_CALC*** function calculates the VG added equilibrium shear-stress based on x-coordinate; it runs at each node following the VG location until separation or the trailing edge.

In the original code, the program iterates the airfoil boundary layer solution for a single angle of attack until convergence before outputting a result. The VG influence function depends on the BL parameters, so every iteration also prompts re-initialization until convergence. While the inviscid code of the current program is unsteady, the solution reaches convergence for every single timestep. Thus, the code behaves no differently than in the original VGFOIL implementation.

While the solution method remains the same, the unsteadiness of the simulation reintroduces an existing problem. In developing the original code, the author noticed a persistent issue of the program crashing in the first few timesteps. The initialization of the airfoil at a non-zero angle would result in an initial error that was too large for the convergence mechanism to deal with, and the BL solution would diverge, resulting in an inability to obtain viscous results. The instability upon initialization was especially apparent with a moving/pitching airfoil, such as the case of an airfoil pitching beyond the steady stall angle. In order to alleviate this, an inviscid simulation would first run to initialize the wake and significantly reduce the incidence of crashing. When simulating an airfoil with VGs, the activation of the boundary layer tends to crash the program more often. Swafford's turbulent velocity profile equations are highly sensitive to the input, and the values in the first few timesteps of BL activation cause the VG module to give an error. Building on past ideas, initialization of the boundary layer with a clean airfoil first showed a reduction in the number of crashes and gave consistent results to a simulation without a preliminary BL initialization.

6.3. VERIFICATION FOR $\alpha = 14°$

Before proceeding with the validation of the VG module, it is imperative to verify that the code performed as intended. While steady results are comparable to results obtained from VGFOIL, the differences in the solution method of XFOIL and the base code of the double-wake vortex-panel model would not necessarily give comparable data. To confirm the capability of the model to simulate VGs, the model must reflect the changes in BL

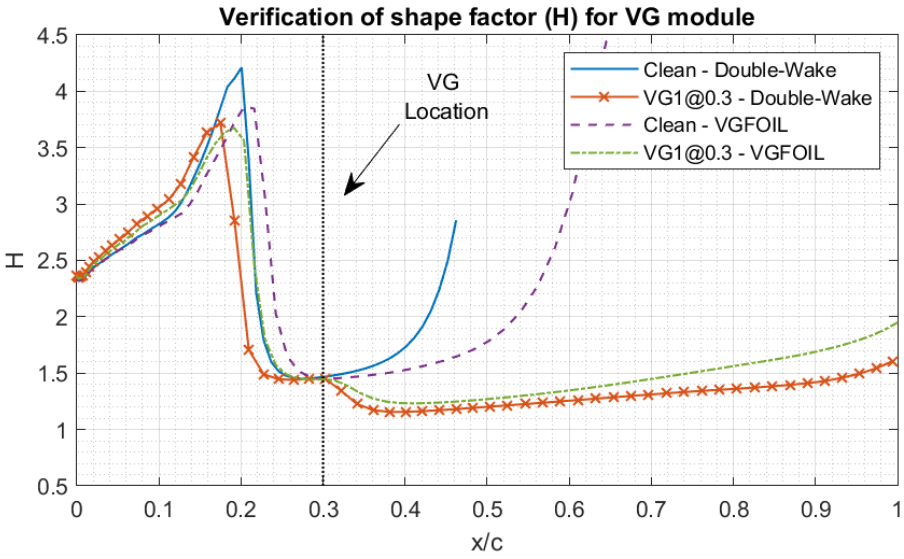

Figure 6.2: Comparison of shape factor between a clean airfoil and with vortex generators in current model and VGFOIL for airfoil at 14°

parameters that a VG would impact on the flow in real life. The model's performance cannot be fully validated this way, as BL variables are not measurable experimentally. The only purpose is to verify that they are affected in the right location and with the correct magnitude and direction.

The model can be verified by examining the changes in critical variables affected by the VG, introduced in Section 3.3 and Section 3.4. The variables in question are the shape factor H and the coefficient of friction C_f. While the momentum thickness θ and displacement thickness δ^* can also be observed, the shape factor is a derivative value, and correct trends in its behavior would signify sufficient accuracy of the former two variables.

The verification of the model examines results for the same DU17DBD25 airfoil at a steady angle of attack of $\alpha = 14°$ and Reynolds number Re = 1,000,000. At this angle, the experimental data and the model predicted accurately that the clean airfoil would undergo a partial stall on the suction side. The separation of flow appears in the data through the C_p measurements and the non-linearity of the C_L curve. In the experimental data, adding VGs to the airfoil delays stall overall, and this particular angle of attack would experience fully attached flow. For the model's verification, the results obtained should likewise show a delay of stall through the induced mixing of the VGs.

In Figure 6.2, the shape factor is plotted for the converged simulation of a clean airfoil and an airfoil with the $VG1$ setup, one of the two VG configurations in the experimental data. Whereas it is important to mention that $VG1$ is 1.5 times the size of $VG2$, the exact dimensions are not relevant for this example; further details can be found in the

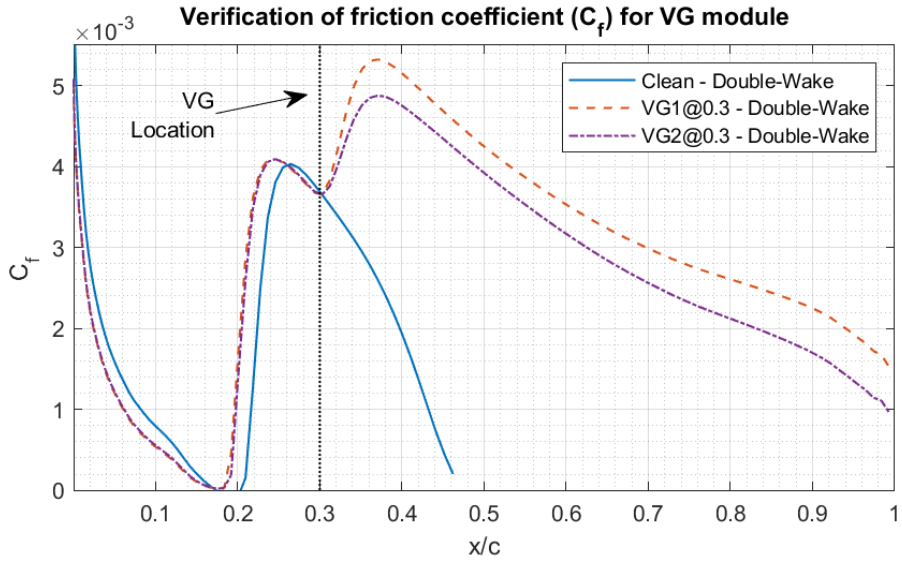

Figure 6.3: Comparison of coefficient of friction (C_f) from current model for airfoil at 14°

accompanying paper by De Tavernier et al.[4]. The curves in both setups indicate a steadily rising shape factor until a free laminar/turbulent transition causes a rapid drop to around $H = 1.5$. It is important to note that the curves have similar shapes but are at an offset to each other due to a difference in stagnation point caused by the separation of the flow in the clean case. After the drop, the shape factor of the clean setup continues rising until separation at approximately $(x/c) = 0.46$. In the other setup, the vortex generator at $(x/c) = 0.3$ causes another sharp drop, and a positive gradient maintains until the trailing edge. The results from the double-wake VG model appear to compare well to those obtained from VGFOIL. While the implementation of the VG module is identical, the partial stall experienced by the airfoil at this angle results in slight differences between them due to the single-wake/double-wake formulation. Despite this, the effect of VG addition is almost identical in each model; this effect manifests through separation prevention due to increased mixing beyond the VG location and an earlier laminar-turbulent transition resulting from it. As the separation criterion is defined by a negative C_f in turbulent flow, it is important to also examine that value.

The graphs depicting the friction coefficient C_f plotted against the streamwise coordinate for the upper side are seen in Figure 6.3. The plot only shows the geometrical upper side, as the values close to the stagnation point are of a much higher magnitude. The value of C_f decreases steadily until transition for both cases, before rising to a maximum and falling again. For a clean airfoil, this value continues dropping to below zero, upon which it exceeds the separation criterion of $C_f < 0$ in a turbulent flow. The vortex generator case shows a slowly falling value until the VG location at $(x/c) = 0.3$, where a sharp rise in C_f occurs. While the slope of the curve after the rise remains negative, it does not go below zero again, and therefore separation is not predicted by the current model. As previously

mentioned, the dimensions of $VG1$ are larger than that of $VG2$, and it would influence the flow with greater magnitude. The difference in magnitude can be seen in the figure above, as the curves are identical before the VG, whereupon the spike in C_f is larger for $VG1$. While Kerho and Kramer[2] suggest a step-like increase in C_f at the VG, the jump in the value at the VG in these results can be likened more to a transition-induced C_f jump. The parabolic increase in friction coefficient agrees with the results from their simulation shown in Figure 3.3. Due to differences in C_f formulation between XFOIL and the double-wake model, the verification process does not compare the two directly in this case. However, the behavior of the friction coefficient seen in the simulation once more corresponds well with the results presented by De Tavernier et al.[3]. Therefore, one can conclude that the implementation was successful, and more extensive result collection can continue for a broader range of cases.

7

EVALUATION OF THE DOUBLE-WAKE VORTEX-PANEL MODEL WITH VORTEX GENERATOR FUNCTIONALITY

With the vortex generator module implemented in the code, the program can run for the remaining cases in the dataset with VG data. The previous validation steps were performed for a previously validated model, expecting a specific outcome when performing the runs. The addition of VG simulation functionality brings the model into an unknown area, and one can only assess its performance relative to the validation outcomes. Therefore, gathering results from VGFOIL parallel to the double-wake VG simulation for identical cases allows for evaluation of the double-wake model's improvement over VGFOIL in the steady case. Furthermore, as the validation analyzed the performance of the double-wake vortex-panel model, the relative errors found in that chapter provide the reference for the analysis of the new results.

Previously in the validation steps, the choice of timestep was a vital variable that potentially gave significantly different results. The choice of timestep was investigated in the NACA0015 validation, relating it mathematically to the inflow speed. The validation performed for the clean DU17DBD25 airfoil confirmed that the rule also applies in this case. Finally, as the timestep choice was confirmed and a consistent timestep was used in the validation, using the same in obtaining the results with VGs ensures comparability. A consistent timestep is especially important when comparing identical unsteady cases with VGs and without them, as it will give the most accurate conditions for finding the relative impact of the VG module.

The airfoil in the experimental test setup from which the data originates spanned $c =$

$0.36m$. The vortex generators placed on the airfoil were both set to an angle of $\beta_{VG} = 15°$, and measured in at $h_1 = 6mm/l_1 = 18mm$ for $VG1$, and $h_2 = 4mm/l_2 = 12mm$ for $VG2$. Simulating VGs in the model requires scaling down the dimensions by a factor, the same factor applied to normalize the airfoil to a unit chord. A linear increase in VG dimensions is appropriate because the VG only acts on the boundary layer, which also scales with chord linearly.

While the dataset for the clean airfoil is extensive, experimental data for an airfoil with VGs is less varied; thus, the assessment of the program's performance will utilize all the available data. While the previous validation included performance analysis at different Reynolds numbers, data with VGs only exists for Re = 1,000,000. The dataset is also limited to two levels of pitching unsteadiness, which purposely match the previous validation values of $\kappa = 0.027$ and $\kappa = 0.054$. However, one benefit is the ability to move the VG between three streamwise locations at $(x/c) = 0.2, (x/c) = 0.3, (x/c) = 0.4$, allowing for broader analysis per flow case. Both forced and free transition cases provide insight into the model's capabilities. The experimental data used zig-zag tape at $(x/c) = 0.05$ to trip the boundary layer; thus, this is the location referred to when discussing forced transition. Finally, the dataset spans the same ranges of angles as before; A steady airfoil in the range of $-25° < \alpha < 25°$ and two unsteady pitching cases around mean angles of $\alpha_0 = -11°$ and $\alpha_0 = 9°$ with an amplitude of $\Delta\alpha = 7°$ for both. This chapter excludes the case of dynamic pitching with mean angle $\alpha_0 = 1°$ due to a lack of meaningful VG effects in this angle range.

7.1. STEADY RESULTS

Prior to the simulation results analysis, a summary of the trends in the experimental data with VGs is presented. Figure 7.1 shows the graph of lift coefficient plotted against the angle of attack for the DU17DBD25 airfoil with a variety of VG configurations. The difference in maximum C_L and the stall angle α_S are critical variables that determine the accuracy of the simulation. In the graph, every VG configuration achieves an increase in $C_{L_{MAX}}$ and stall angle; however, the optimal location appears to be somewhere around $(x/c) = 0.3$. The addition of VGs causes no change to the slope of the lift curve during attached flow, with stall being delayed or prevented with VGs at angles of attack in which the clean airfoil experiences entirely separated flow. It is also important to note that the sharp drop-off in lift increases in severity as C_L increases, which is essential to recreate in simulation results.

In previous cases, the lift coefficient for a given angle resulted from filtering the lift of a steady airfoil in an unsteady formulation. Observing the noise in the lift coefficient for a steady angle gave clues to the source of the phenomenon. Additionally, this allowed for eliminating the influence of the slow pitching motion retained by the wake vortices. Unfortunately, this was impossible for the entire range of angles with VGs enabled. Previously, the model initialized from an inviscid solution to increase the stability of convergence at higher angles of attack; it was prudent to do the same with VGs turned on. Section 6.2 introduced a development upon this idea, where an intermediate initialization of the boundary layer without VGs would follow the inviscid initialization. However, when reaching angles far beyond the deep stall of a clean airfoil, the boundary layer fails to

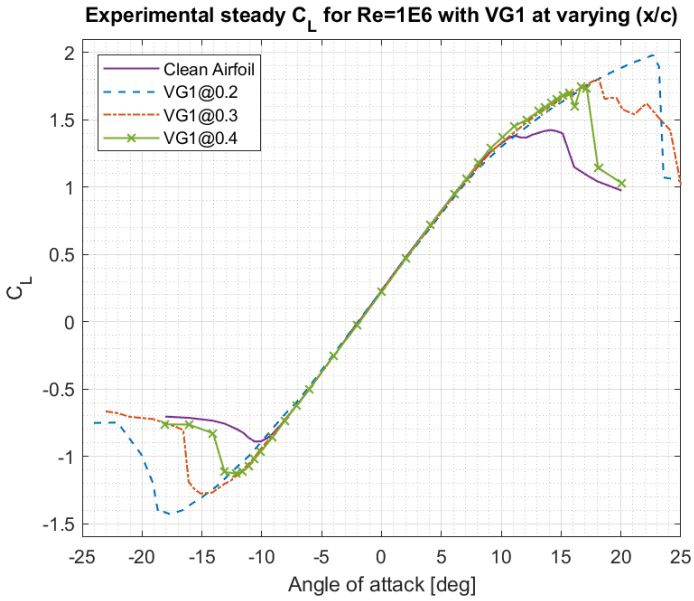

Figure 7.1: Comparing the effect of streamwise VG location on lift curve of steady DU17DBD25 airfoil

converge. Given the VG module's sensitivity to the input conditions, the model also fails to start from the inviscid initialization. Therefore, a pitching motion with step-like increases found good convergence at the highest angles of attack. To further limit the quasi-steady phenomena resulting from a pitching airfoil, the model trimmed the length of the wake behind the airfoil.

The first configuration is plotted in Figure 7.2, where the two continuous lines show a comparison between the simulation and experimental lift coefficient curve. It is clear that the slope of the graph is not affected by the VG, as the two curves are identical until approximately $\alpha \approx 8°$. Whereas the real-life airfoil partially stalls near the trailing edge, the flow in the simulation remains fully attached until a much larger angle. As was noted in the previous chapter, separation occurs when the coefficient of friction C_f becomes negative in a turbulent flow. Based on the graph, the mixing induced by the VG increases C_f more than the experimental data would suggest. While the $C_{L_{\max}}$ and stall angle α_S are both overestimated, the simulation shows a sharp drop lift past $\alpha = 23°$. Here, the separation point moves quickly up the airfoil from the trailing edge, and the airfoil goes into a deep stall. This behavior is particular to VGs in general and can is represented well by the model.

There is a slight difference in the results compared to the original implementation of the VG module in VGFOIL. While both models are vortex panel methods and solve the boundary layer like XFOIL, the difference arises in both extremes of angles of attack. The single-wake VGFOIL code has a smooth stall region, whereas the current model has a double-wake formulation, which is influenced dramatically by the VG module. The

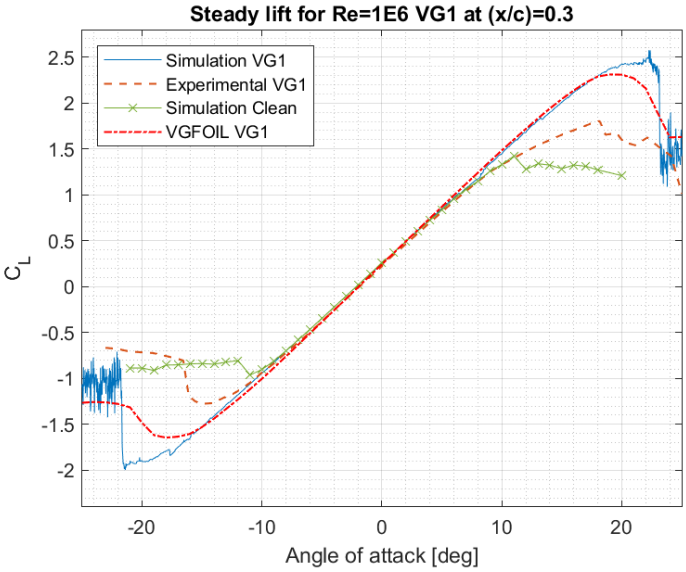

Figure 7.2: Evaluation of VG module with VG1 placed at $(x/c) = 0.3$

change in the separation calculation results in a later but more violent separation of the flow, leading to a better approximation of deep stall characteristics in the double-wake results.

The C_L of the clean configuration highlights the influence of the VG module on the lift curve. As expected, the slope of the points matches the other two curves identically until the clean airfoil begins to partially stall as it progresses beyond its $C_{L_{\max}}$ at $\alpha \approx 11°$. The VG simulation's divergence indicates that the VG's influence on the BL shear stress equilibrium is enough to delay stall when it would otherwise appear from the trailing edge. However, the current calibration of the VG source-term causes the function to overestimate the magnitude of its attachment promotion significantly.

In order to gain a deeper understanding of the vortex generator's influence on the BL, the validation continues with a simulation of the smaller vortex generator (VG2) with an identical flow case and streamwise placement. Restricting the changes to the VG dimensions allows one to isolate the impact that such a change might have. Figure 7.3 shows the experimental and simulation results for VG1 and VG2. The verification of the model showed that the smaller dimensions of VG2 resulted in a lower jump in the C_f value, a key variable in determining the separation point. While fully attached flow would give a linear increase in the lift with a higher angle of attack, this increase stagnates as the airfoil begins to stall. As observed from the graphs, the smaller C_f offset from VG2 means that separation occurs at a lower angle of attack, and the airfoil enters a deep stall a few degrees earlier than the larger VG1. While this difference is pronounced in the simulation results, it can only be seen in the experimental data past an angle of attack of $\alpha = 21°$. For the negative angles of attack, the trend of an earlier stall is also found and is

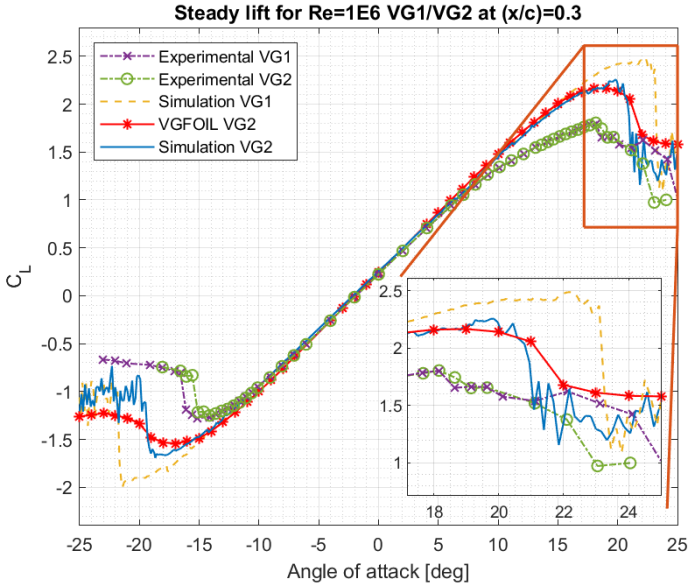

Figure 7.3: Evaluation of VG module with VG2 placed at $(x/c) = 0.3$

more noticeably reflected by the experimental data. In both simulation cases, once a stall begins with an enabled VG, the separation point travels rapidly towards the leading edge, and the flow separates. Whereas the VG1 case might still have almost entirely attached flow, the airfoil in the VG2 case is already stalling.

Whereas the experimental data shows little difference between the two VG setups, the double-wake results have a much more pronounced difference. The double-wake method and VGFOIL curves are almost identical, with the double-wake simulation indicating a sharper flow separation. However, while the experimental data and VGFOIL results show little difference between the lift for VG1 and VG2, the double-wake model gives significantly different results for the two configurations. An unparalleled change suggests that the initial data for which the VG source-term was tuned is insufficient in scope for the double-wake model. While the geometry of this airfoil is less typical, the lack of a difference between the VGFOIL results indicates that the formulation of the separation region is the cause of this change. The calibration of the term aimed to minimize the error on the VGFOIL results; the single-wake simplification does not take into account the current variables that dictate partial separation. While the authors of the method acknowledged that the model could benefit from being trained on more data[3], an improvement could be sought by recalibrating the term for the current model.

Lastly, the DU17DBD25 validation found that flow cases with a lower Reynolds Number had better adherence to experimental data. The simulation captured the flow phenomena better when it was undergoing more gradual changes, similar to an effect of a smaller VG when compared to a larger one. This improvement presents the hypothesis that with

less mixing introduced to the BL by the smaller exponential term resulting from the VG2 configuration, the model should remain more stable and achieve a relative improvement in the results.

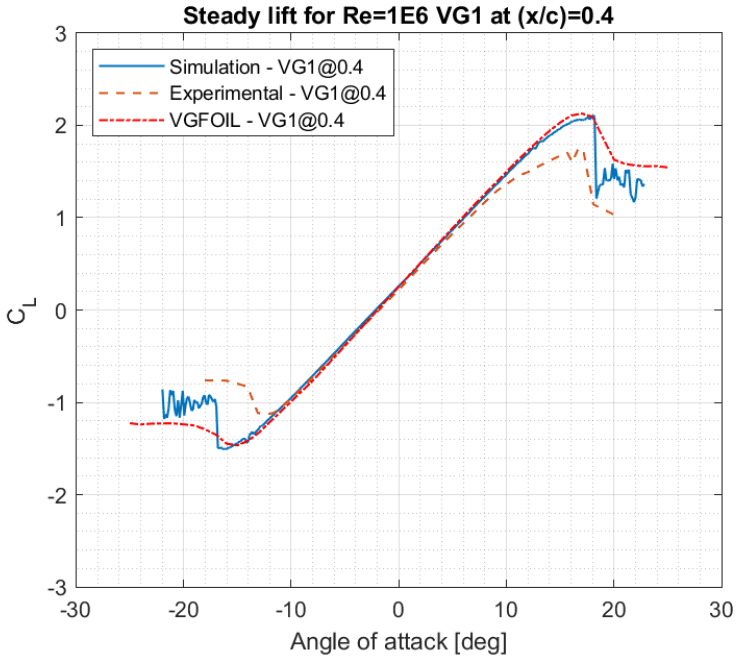

Figure 7.4: Evaluation of VG module with VG1 placed at $(x/c) = 0.4$

The model showed good adherence to the experimental data for the lift values obtained for cases with VG1 and VG2. Continuing the analysis, the effect of chordwise VG placement is evaluated through a simulation of VG1 placed at $(x/c) = 0.4$, and the resulting steady lift curve is plotted in Figure 7.4. Looking back to the experimental data plotted in Figure 7.1, the experimental data indicates an improvement in $C_{L_{\max}}$ and α_S for any VG setup, with increasing performance with VGs closer to the leading edge. Starting with the simple results for VG1 at $(x/c) = 0.4$, the stall characteristics of the curve are captured very well by the model, with a slight overprediction in magnitude for the positive angles and later stall for the negative angles. The simulation also performs better than VGFOIL, with almost identical results up to separation, at which the double-wake model predicts the sharp decrease in lift seen in the data.

Continuing the analysis of chordwise VG placement, a simulation runs for an airfoil with VG1 at $(x/c) = 0.2$. However, during the simulation the model encountered an error, which can be found in Figure 7.5 labeled as "Erroneous Results". Looking at the predictable and expected aspects, the double-wake model overestimates the lift coefficient for the negative and positive angles of attack. However, this is consistent with all the results gathered so far, with the overestimation resulting from the increased flow attachment

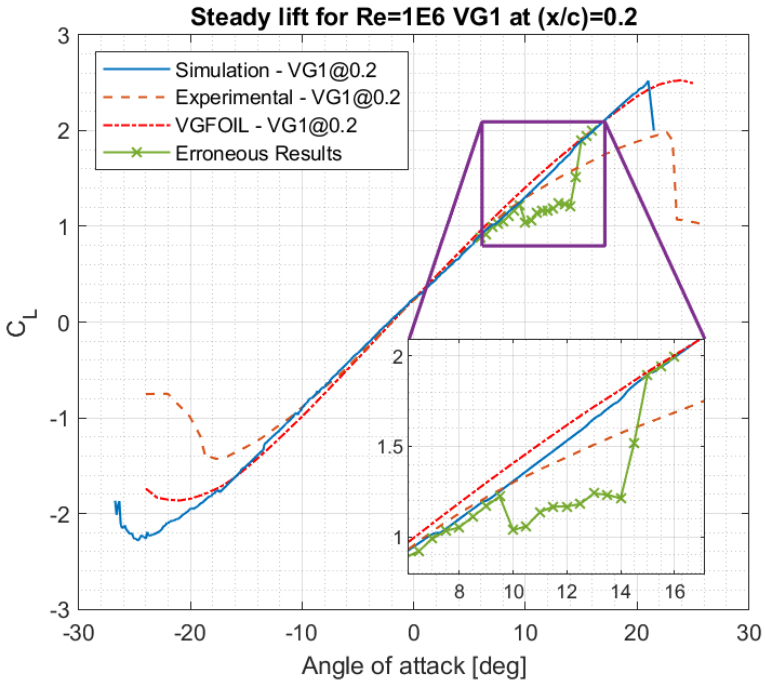

Figure 7.5: Evaluation of VG module with VG1 placed at $(x/c) = 0.2$

caused by the VG. Unlike the previous cases, which gave results beyond stall despite a large amount of noise, the close placement of the VG to the leading edge caused instantaneous crashing upon stall in the positive angles. The problem occurs as the onset of stall causes significant changes in the BL variables, preventing the VG function from converging in a single timestep.

The curve corresponding to the original implementation shows a drop in lift curve slope at $\alpha \approx 10°$, a partial airfoil stall. With the VG close to the leading edge, it forces a transition as instability is insufficient for it to occur before the VG location. The forced transition significantly inhibits the separation prevention capability of the VG, as the sum of both C_f increases is only equivalent to the C_f increase from laminar/turbulent transition. For this intermediate range of angles where the VG imparts a forced transition, the airfoil's lift stagnates and deviates from the VGFOIL curve. Once the transition point moves beyond $(x/c) = 0.2$, flow reattaches, and separation occurs again at the extreme. This intermittent separation is not present in the experimental data, indicating that the VG module diverges from optimal functionality when it forces transition at the VG location.

The $(x/c) = 0.2$ configuration unsteady validation identified this issue as a problem in the interaction between the laminar/turbulent transition and the VG; Figure 7.2.3 provides a detailed explanation of the issue and resolution. An amendment to the code resulted in the curve labelled "Simulation - VG@0.2", seen in Figure 7.5. The simulation improves its

prediction of lift coefficient in the intermediate angles, and flow does not separate where it did before. Nonetheless, the slope shifts slightly at this point, an effect of reduced VG mixing capability when too close to the transition point.

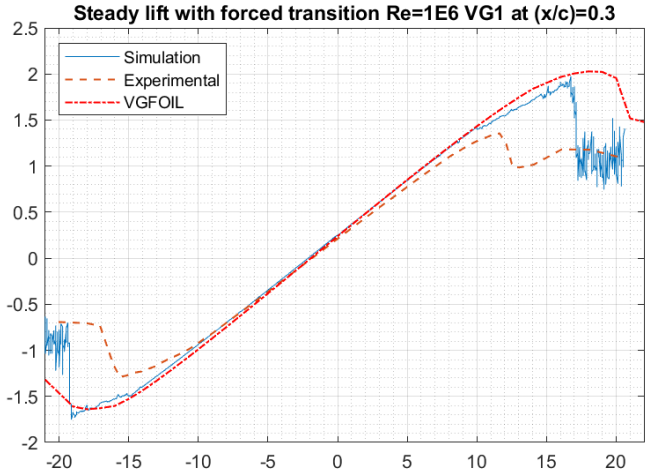

Figure 7.6: Steady lift results for VG1 at $(x/c) = 0.3$, with forced transition

The previous steady lift curves corresponding to free transition cases showed a notable improvement in maximum C_L and increased stall angle α_S with the addition of a VG to the BL layer. These improvements showed up in both the double-wake model results and the experimental data and came from the VG-induced mixing promoting better flow attachment. With the VG positioned slightly aft of the quarter-chord in a free transition configuration, the VG will act on the flow when it is already turbulent or trigger a transition. With forced transition at the leading edge, the coefficient of friction C_f can drop rapidly, causing flow separation before the VG location. A VG cannot impart mixing on separated flow, and a stalled airfoil experiences performance degradation through significantly reduced maximum C_L. The simulation captures the drop in lift resulting from this, and although an error remains in the precise values, the direction of the change is correct. While the negative angles of attack show little difference from VGFOIL in the angle of stall of $C_{L_{\max}}$, the positive angles agree much better with an earlier and more sudden drop in lift seen in the double-wake model.

7.2. UNSTEADY RESULTS

This thesis aimed to develop a model that included VG simulation capabilities in a double-wake vortex-panel method. The purpose of achieving this is to provide a design tool that can more accurately estimate airfoil performance without the need for more complex simulations such as CFD. In previous research introduced in Chapter 2, the first benefit of a double-wake method was the increased accuracy in the simulation of stalled flow on a steady airfoil. Integration of VGs to the model proved successful and would allow

for a more detailed steady design capability. While this is a meaningful outcome, the slight improvement over existing methods is not the paramount goal of this work. The capability of a double-wake vortex-panel model to capture dynamic stall phenomena and predict accurate lift values for attached, partially separated, and fully separated is unique for this type of model. As one of the primary vortex generator applications in wind energy is the reduction of dynamic stall-induced fatigue, the analysis of the VG module's performance in unsteady flow is essential.

The validation of the airfoil utilized a wide range of steady airfoil angles and varying amplitudes of unsteady pitching movements with varying inflow speeds. Whereas it was essential to ensure that the base model can run in all conditions, the VG only has a significant effect in near-stall conditions; thus, the validation only considers configurations that reach this criterion. Therefore, the overall objective is to develop a tool that can be used in airfoil design, as the tool has undergone thorough calibration for the final output values. As mentioned previously, the objective of the result analysis is to evaluate the model's performance in each case and decide whether it is sufficient to conclude anything. A vital aspect of this analysis is the change in results and accuracy with different inputs and variables, assessing the simulation's strengths, weaknesses, and potential sources of error. Thus the trend in results due to variable changes is highlighted as proof of concept.

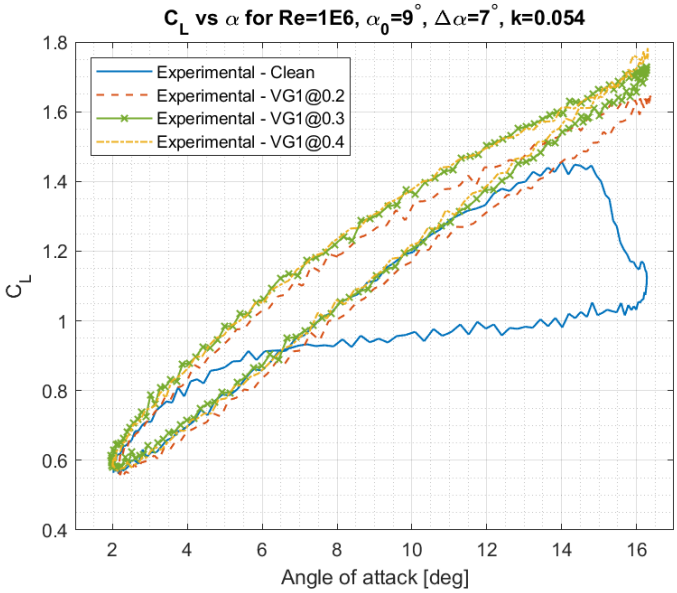

Figure 7.7: Experimental data comparison of C_L vs α curve for $\alpha_0 = 9°$,$\Delta\alpha = 7°$,and $\kappa = 0.054$

Just as for the steady results, the experimental results are plotted for comparison in Figure 7.7. The graph's purpose is to illustrate the influence of the addition of vortex generators and for reference to each other. Whereas there is a clear difference when compared to the lift of a clean airfoil, the streamwise placement of the VG has much less impact. Nonetheless, a partial stall occurs towards the higher angles of attack on

the downwards pitching movement. A decrease in lift slope due to partial separation is especially prominent in the VG placed closest to the leading edge, where the lift is affected even in the upwards motion in the clean stall angle range.

7.2.1. REFERENCE CONFIGURATION

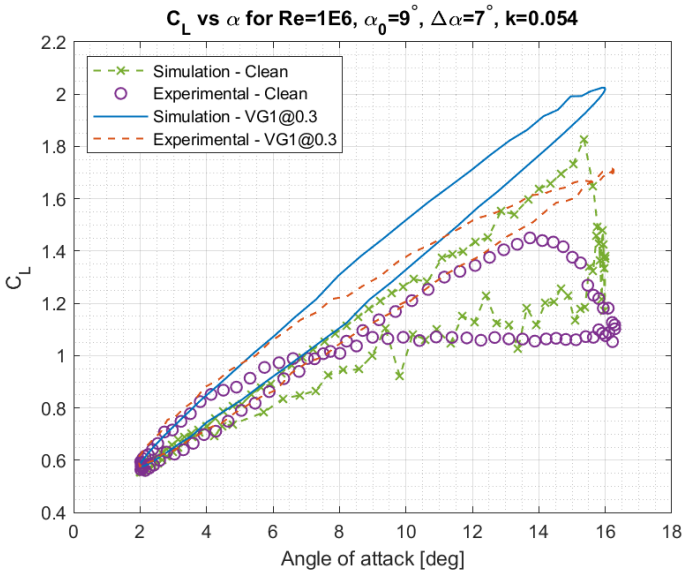

Figure 7.8: Effect of VG addition to C_L vs α curve for $\alpha_0 = 9°$,$\Delta\alpha = 7°$,and $\kappa = 0.054$

To begin the analysis, a case is chosen as a starting point with $\alpha_0 = 9°$,$\Delta\alpha = 7°$,and $\kappa = 0.054$. Illustrated in Figure 7.8, the plot shows the lift coefficient against the angle of attack for the airfoil in the aforementioned unsteady motion. With angles reaching beyond the clean airfoil stall point, the experimental data shows that VG1 successfully delays the stall and prevents a sharp drop in the lift at the higher angles of attack. A fully attached flow would suggest a curve identical to an airfoil oscillation around $\alpha = 0°$; however, the data indicates a slight reduction in the lift on the downwards motion. The simulation indicates similar phenomena as the real-life data, and the resultant lift curve is more representative of ideal conditions. The decrease in slope and lift towards the higher angles of attack would suggest a partial airfoil stall in the experimental data. The simulation indicates fully attached flow, as the VG induces sufficient mixing to keep the C_f above zero over the airfoil for the entire unsteady movement. The simulation results obtained in the validation show that the model could predict the approximate angle of maximum C_L, with a more gradual reattachment of the flow than the experimental data would suggest. Despite this, the double-wake model predicted a higher C_L than experimental data would indicate for the entire upwards motion, along with $C_{L_{\max}}$. Therefore, the overprediction in the lift for the VG1 case could be attributed to the same error as was present previously. The proclivity for the flow to remain attached is a direct result of the VG increasing the friction coefficient, preventing flow separation even at higher angles

of attack. The validation of the steady case suggested a similar trend through the rapid onset of a stall that happened later than seen in the experiment. An alteration to the VG source-term function could improve this behavior and potentially remove the source of error.

7.2.2. EFFECT OF VG DIMENSIONS

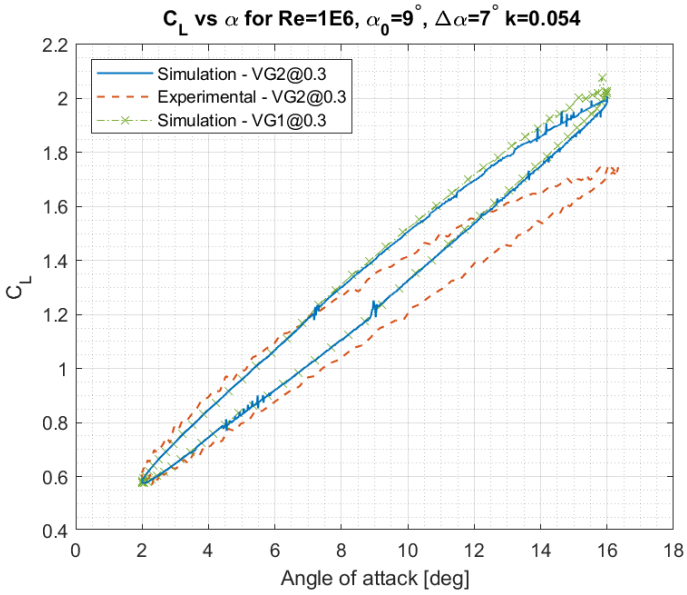

Figure 7.9: Effect of VG2 addition to C_L vs α curve for $\alpha_0 = 9°$,$\Delta\alpha = 7°$,and $\kappa = 0.054$

The simulation repeats for the same pitching and flow conditions with a smaller VG2 setup; the hysteresis loop of the double-wake model results and experimental data are compared in Figure 7.9. While not plotted in this figure, the experimental lift coefficient curve for VG2 is identical to that of the VG1 configuration. The lack of a difference agrees with the findings of the steady validation, where a reduction in VG size did not limit its performance significantly and achieved comparable increases in $C_{L_{\max}}$ and angle of stall α_S. The double-wake results show a similar trend to the steady results, where the reduction of VG size results in a slight drop in the lift coefficient. As the impact of the VG is less impactful on the boundary layer, the upper side of the airfoil becomes more prone to partial flow separation at the initial downwards movement. The reduction in the lift is unsubstantiated by the experimental data, suggesting an error in the VG-induced mixing magnitude. In VGFOIL, the vortex generator dimensions were part of multivariable analysis for calibration, but their effect on separation was not; The lack of accurate separation prediction in XFOIL likely caused this disparity in the results.

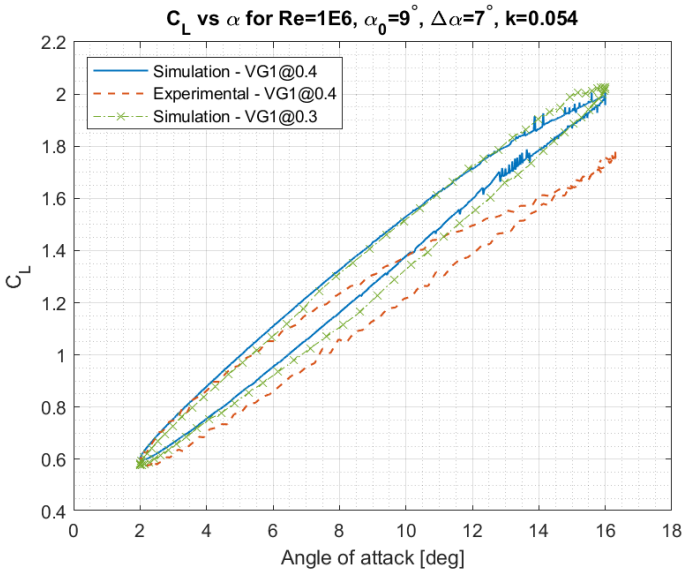

Figure 7.10: Effect of VG1 placed at $(x/c) = 0.4$ to the C_L vs α curve for $\alpha_0 = 9°$,$\Delta\alpha = 7°$,and $\kappa = 0.054$

7.2.3. EFFECT OF VG STREAMWISE LOCATION

Besides changing the VG dimensions, the model's performance can depend on streamwise location. As introduced in Section 3.2, the ideal placement of a VG on an airfoil depends on the situation and desired outcome. The variables taken into account span from the VG parameters, such as type or dimensions, to the clean performance of the airfoil. It generally trends that smaller VGs submerged in the boundary layer perform better towards the leading edge, whereas larger VGs such as the one in the simulation fare better beyond a given aft position. Figure 7.7 shows little difference between the lift curves of an airfoil with VGs placed at either $(x/c) = 0.3$ or $(x/c) = 0.4$, mirrored by the double-wake simulation results. The marginal differences between the two curves result from an offset in the C_P curve stemming from a difference in the boundary layer solution.

Figure 7.11 shows the lift curve for the airfoil with a VG placed at $(x/c) = 0.2$. With a vortex generator sized approximately to the height of the boundary layer, the experimental data illustrates the reduction in its effectiveness at delaying stall. While this difference exists, the simulation results go further beyond this point. At first glance, these results appear to be erratic and unusable; however, looking deeper into the data gives insight into the edge cases which interfere with optimal model performance.

Currently, the model cannot predict fully attached flow separating and reattaching over a downwards pitching motion, resulting from the VG and transition point interaction. If an airfoil pitching down with fully attached flow is input to the flow reattachment algorithm, the stall point remains locked to the trailing edge. Flow reattaching due to the transition point moving up likely indicates non-optimal VG module behavior. In order to obtain the most credible results possible, it is necessary to make adjustments to the

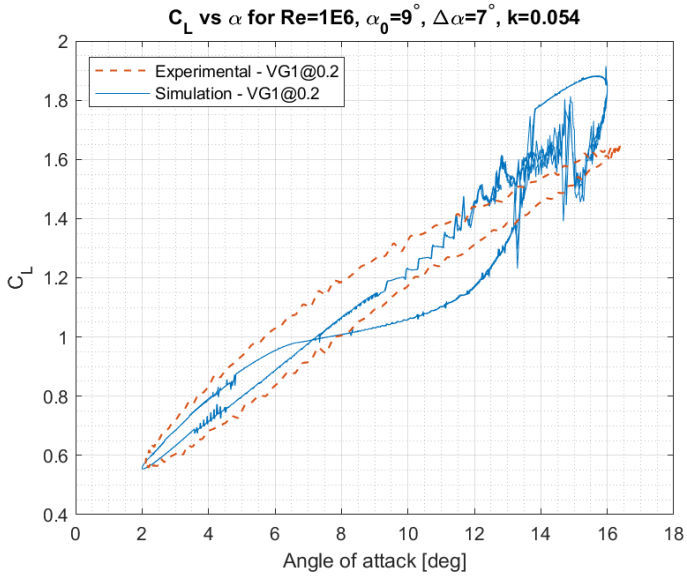

Figure 7.11: Erroneous solution for the effect of VG1 placed at $(x/c) = 0.2$ to the C_L vs α curve for $\alpha_0 = 9°$,$\Delta\alpha = 7°$,and $\kappa = 0.054$

base vortex-panel code to account for this. The existing reattachment function forces the separation point to move towards the trailing edge to avoid instability.

7

AMENDMENTS TO THE CODE TO EXPAND ITS FUNCTIONALITY

The forced movement aft of the separation point is amended by conditionally allowing the separation point to move upwards in the reattachment phase; this allows the boundary layer to quickly reach convergence if the separation point is far enough from the trailing edge, with the resulting curve shown in Figure 7.12.

The results with a changed reattachment criterion show increased parity with the experimental data. The simulation roughly preserves the characteristic oval shape; however, an early flow separation on the pitch-up motion remains. A vortex generator is most effective when it can increase the mixing of the flow at precisely the required magnitude to prevent C_f from going below zero. While going above this required value increases drag and tends to lower performance, failing to introduce sufficient mixing to prevent separation is much more impactful. Excluding input parameters, boundary layer variables solely determine the impact of the VG mixing function in the current model. While the location of the maximum magnitude occurs slightly beyond the point of free transition, a VG imparting less mixing on the flow can prevent separation more effectively. To understand why the flow is separating during the pitch-up motion, one must compare the effect of streamwise VG placement on the coefficient of friction on the suction side before separation. Figure 7.13 shows a plot of C_f for the current pitching case at an angle of $\alpha = 10°$ on a pitch-up motion.

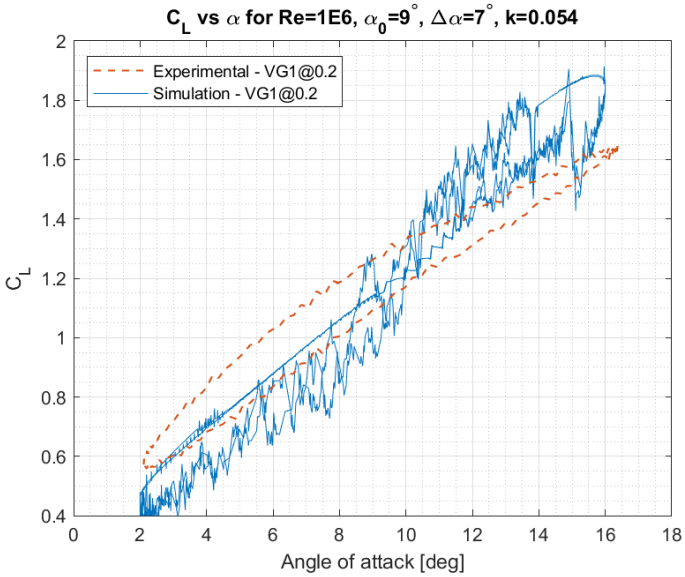

Figure 7.12: Separation and reattachment on pitch-down with VG1 placed at $(x/c) = 0.2$ to the C_L vs α curve for $\alpha_0 = 9°$,$\Delta\alpha = 7°$,and $\kappa = 0.054$

Referring to the C_f curve corresponding to the $(x/c) = 0.2$ VG location, it is clear that the VG-induced mixing is severely limited. The VG is far enough up the airfoil to trigger laminar/turbulent transition in this situation. The sharp increase in mixing by the VG bypasses the gradual increase in C_f resulting from a forced transition, reducing the total rise in C_f. The total impact of transition and the VG contrasts the curves corresponding to VGs at $(x/c) = 0.3$ and $(x/c) = 0.4$, where a transition occurs before the VG location, preventing a stall. Partial separation over the suction side continues throughout the upwards pitching motion resulting in a lift reduction. As the angle of attack increases, the location of free transition moves forward and beyond the VG location. The VG effectiveness increased upon the movement of the transition point away from the VG location, inducing a higher C_f. The flow subsequently transitions from partial stall to fully attached at the highest angle of attack. When the airfoil swings back to pitch down, the free transition point moves back down the airfoil and induces separation again. Nonetheless, as the boundary layer has to separate and reattach during the pitch-down motion, the results cannot be considered realistic, and adjustments to the VG interaction with transition must be applied.

Further inspection reveals a potential solution to the source of error. The simulation logs indicate that the VG module provides a wrong result when initializing the source term at the transition location. A wrong result results in the VG source-term strength being zero, a result of an error; This error results in total exclusion of VG influence when its location is fore of free transition. Due to the changes in boundary layer variables at the transition point, Swafford's velocity profile equations are unable to evaluate the velocity at the VG

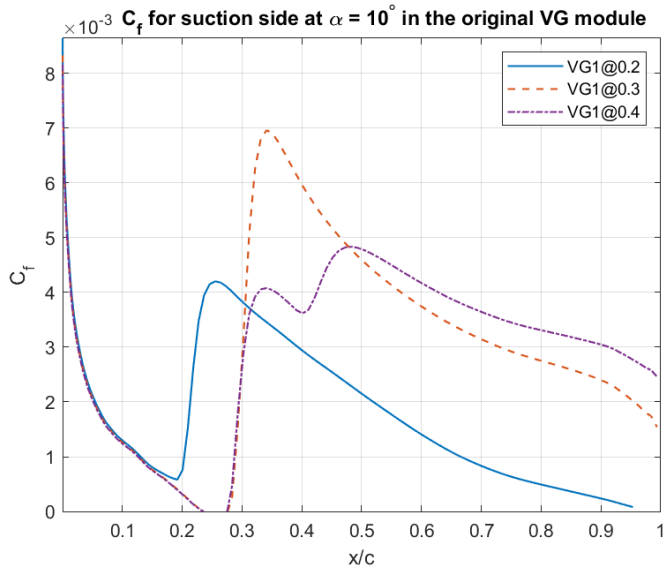

Figure 7.13: Comparison of C_f values for an airfoil pitching upward in the unsteady motion of $\alpha_0 = 9°$,$\Delta\alpha = 7°$,and $\kappa = 0.054$

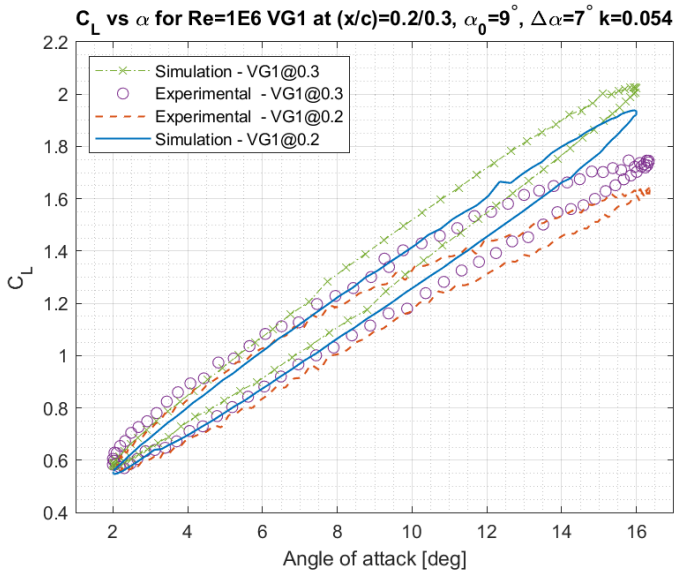

Figure 7.14: Performance of the code amendments to the VG module with VG1 at $(x/c) = 0.2$ in the C_L vs α curve for $\alpha_0 = 9°$,$\Delta\alpha = 7°$,and $\kappa = 0.054$

(U_{VG}), consequently nullifying the VG-mixing term. However, as the solution progresses a

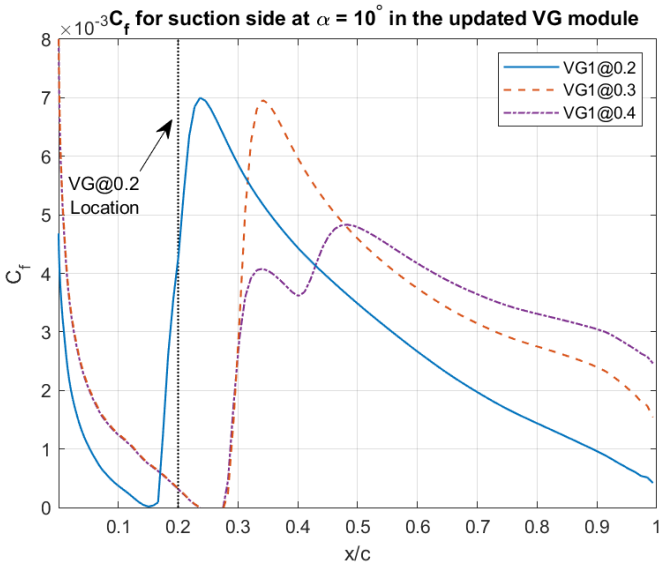

Figure 7.15: Comparison of C_f values with the code amendments for an airfoil pitching upward in the unsteady motion of $\alpha_0 = 9°, \Delta\alpha = 7°$,and $\kappa = 0.054$

few nodes further, the values of θ, δ^*, and u_e normalize sufficiently to result in a solution. The tail end of the VG-induced mixing can then be applied from that point onwards, keeping the center of the exponential function at the location of the VG. The resulting hysteresis loop, including these changes, is plotted in Figure 7.14. The results obtained have a noticeable improvement over the previous two iterations, and the simulation results for $(x/c) = 0.2$ exhibit a similar trend of reduced lift seen in the experimental data.

By progressing further from transition, the magnitude of the source-term reduces slightly. Furthermore, while the final values of the lift coefficient agree with the experimental data, in this case, the boundary layer solution changed significantly. Figure 7.15 shows a plot of the C_f distribution for the same case, a pitch-up motion at $\alpha = 10°$. Whereas the $(x/c) = 0.2$ configuration previously showed the smallest C_f increase, it now reaches the same value as the $(x/c) = 0.3$ configuration. However, the changes in the flow due to the induced mixing result in the free transition point moving a few nodes ahead of the VG location indicated by the dashed line. The movement of the transition point brings the validity of the simulation results into question. Allowing the VG source-term calculation and its shear-stress impact to occur later in the boundary are knowingly flawed assumptions, expecting some degree of error. However, given that the model achieves a solution in which the movement of the transition point allows the VG to activate naturally, one could argue that those assumptions only serve to encourage simulation convergence, seeing as they no longer apply to the plotted case. The agreement of the converged results with the trends in the experimental data supports this argument. Without this amendment to the code, the results for any case in which the vortex generator forces transition are invalid, as the VG module does not activate for a range of angles. Therefore,

it was reasoned that the benefit of obtaining potentially flawed results outweighs the drawbacks of no results at all.

7.2.4. EFFECT OF NEGATIVE ANGLES

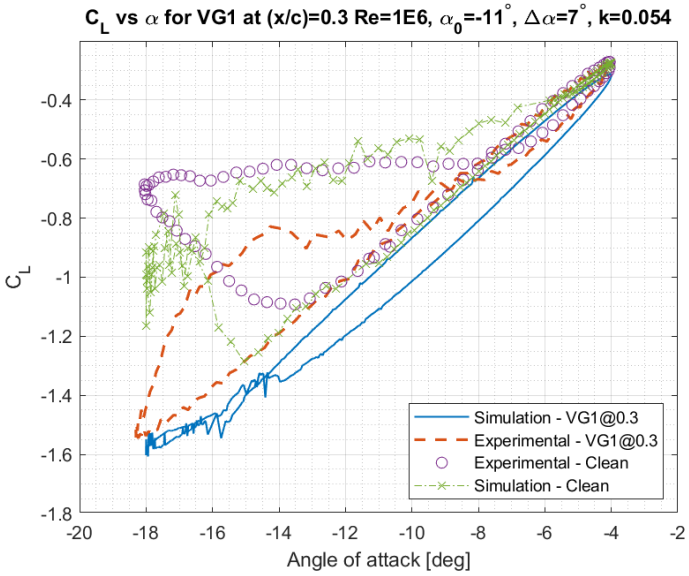

Figure 7.16: Effect of VG1 placed at $(x/c) = 0.3$ to the C_L vs α curve for $\alpha_0 = -11°$,$\Delta\alpha = 7°$,and $\kappa = 0.054$

7

The validation performed for the clean DU17DBD25 airfoil found better agreement with experimental data in the negative angle of attack range. The increased performance is mainly attributed to the significant geometrical upper section curvature resulting from the positive camber and the thickness of the airfoil. On the other hand, the lower section is flatter and more akin to the NACA0015 shape, whose validation found increased parity of the double-wake simulation results and the experimental data. Figure 7.16 shows the lift curve for an unsteady pitching motion around $\alpha_0 = -11$. The slopes of the two curves are very similar for the negative angles of lower magnitude; however, separation does not occur fully as in the experimental data. Similar to the pitching cases in the positive angle range, the VG module calculates a strong impact of the VG on mixing resulting from the overpredicted exponential function source-term. The reduced slope towards the extreme angles suggests partial separation, although of a lower influence than the real-life case would suggest.

Moving the vortex generator more aft leads to the curves plotted in Figure 7.17. Compared to VG1 at $(x/c) = 0.3$, the VG1 placed at $(x/c) = 0.4$ is much less effective at preventing separation, and the airfoil experiences stall throughout the majority of its pitching upwards. The result, however, is an improvement over the clean airfoil as it reaches a higher magnitude of $C_{L_{\max}}$. As expected of VGs, the flow separates much quicker, followed by earlier reattachment. The simulation results appear to mirror every one of the changes

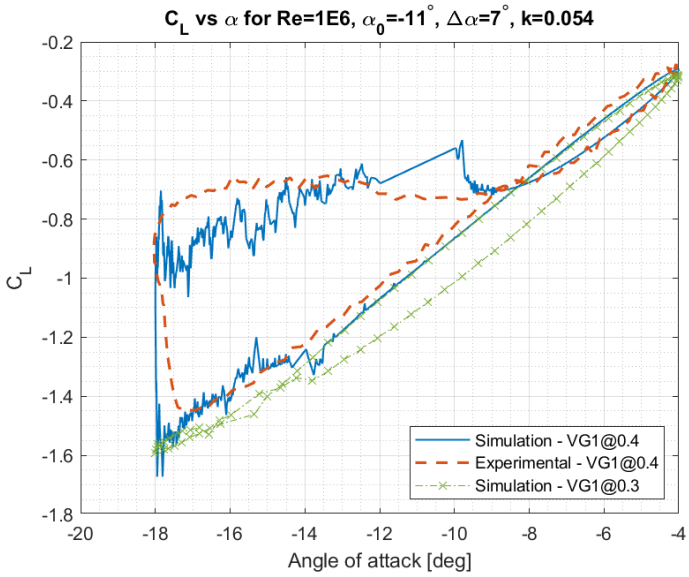

Figure 7.17: Effect of VG1 placed at $(x/c) = 0.4$ to the C_L vs α curve for $\alpha_0 = -11°$,$\Delta\alpha = 7°$,and $\kappa = 0.054$

seen in the experimental data. The onset of separation begins towards the higher angles of attack, and the flow fully separates at the beginning of the upward motion. The separation regions are almost identical, and the reattachment of the boundary layer coincides well with the experimental data. While the results suggested reduced effectiveness of the VG, a better prediction of the lift confirms that the model can perform better when the perturbation is limited.

7.2.5. EFFECT OF PITCHING UNSTEADINESS

Confirming that the VG module gives consistent results requires a simulation of the airfoil for a motion of lower unsteadiness with the same parameters. A comparison between the simulation results and experimental data is plotted in Figure 7.18 to clarify. The experimental data shows the curve of lower unsteadiness reaching a lower C_L at the lowest angle and higher C_L at $\alpha = 16°$ and a more negligible difference between the pitch-up and pitch-down motions. There is no apparent difference in VG performance, and the simulation results differ in the same way. As the boundary layer of the viscous-inviscid model is programmed to be steady, this behavior of the vortex generator in the model is as expected. The relative difference between the two curves indicates that the model captures the influence of unsteadiness despite the relative error between the simulation and experimental data.

7.2.6. EFFECT OF FORCED TRANSITION

The previous section ran and analyzed the model for airfoils with a free transition. While there are cases in which the vortex generator is insufficient in size to promote transition,

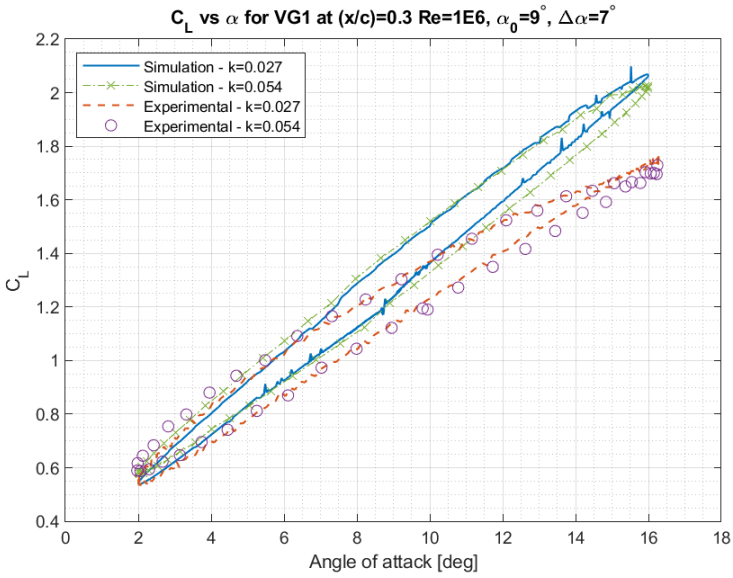

Figure 7.18: Comparison of C_L vs α curve for $\kappa = 0.027$,$\kappa = 0.054$ with VG1 placed at $(x/c) = 0.3$ and $\alpha_0 = -11°$,$\Delta\alpha = 7°$

the model assumes that for the scope of its typical applications, a transition would be triggered at the VG if it had not occurred already. In the case of forced transition, the boundary layer equations switch from laminar to turbulent at the point of transition, $(x/c) = 0.05$. While the initial validation showed a lower capability to predict the lift for airfoils undergoing forced leading edge transition, more consistent results are likely due to the noted increase in VGs accuracy the further it is from transition.

Figure 7.19 shows the C_L curve for the reference pitching case compared with experimental data and simulation results for free transition. In the preliminary validation of the clean configuration of the DU17DBD25 airfoil, forced transition cases followed a general trend of reduced accuracy of the model. As the validation of the thinner, non-cambered NACA0015 in forced transition showed good adherence to the experimental data, it followed that the geometry of the DU17DBD25 was the likely cause of this difference. In the experimental data with VG1 at $(x/c) = 0.3$, the forced transition interferes with the optimal performance of the VG, and flow separates on the pitch-down motion; however, the double-wake simulation for the forced transition case found no separation. While the double-wake model results for free transition show an almost identical curve to the forced transition case, a drop in the lift coefficient is present towards the larger angles of attack. The reduction in C_L is consistent with the clean validation, where a forced transition caused a similar trend in airfoil performance. These results indicate that the VG module works independently of free/forced flow, and the overprediction of lift found for positive angles in the base validation, as well as the proclivity for the flow to stay attached, carry over to this case and can thus be accounted for in the future.

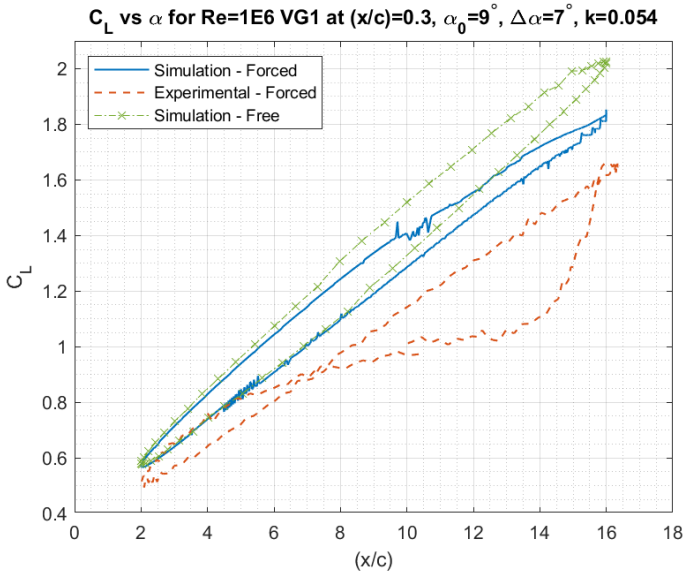

Figure 7.19: Effect of VG1 placed at $(x/c) = 0.3$ to the C_L vs α curve with forced transition and $\alpha_0 = 9°$,$\Delta\alpha = 7°$,and $\kappa = 0.054$

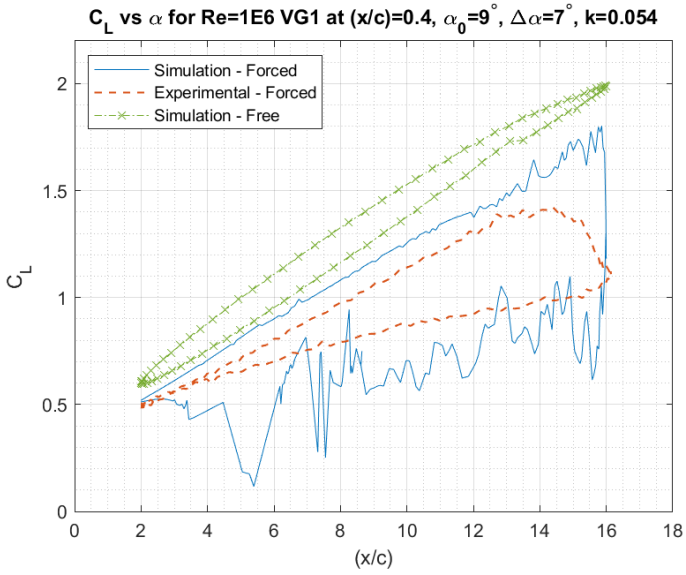

Figure 7.20: Effect of VG1 placed at $(x/c) = 0.4$ to the C_L vs α curve with forced transition and $\alpha_0 = 9°$,$\Delta\alpha = 7°$,and $\kappa = 0.054$

Moving the VG to $(x/c) = 0.4$ with the same pitching case results in the C_L vs. α curve

plotted in Figure 7.20. The experimental data shows further reduction in the VG's capability to prevent separation, and the airfoil begins stalling past $\alpha = 12°$ even on the pitch upwards. The flow remains separated for most of the movement and does not reattach for the entire pitch-down motion. The model appears to yield better adherence to the data with the location of the VG further aft, compounding the argument made earlier. The distance of the VG from the transition point is considerable, and the model can simulate the diminished magnitude of VG-induced mixing more accurately. Furthermore, excluding the overprediction of lift and more sudden separation found in the base case, the results mirror the difficulty for the flow to reattach, signified by the sharp drops in the $\alpha = 4 - 8°$ range. These results lend further credence to the idea that the model works optimally when the VG source-term is smaller.

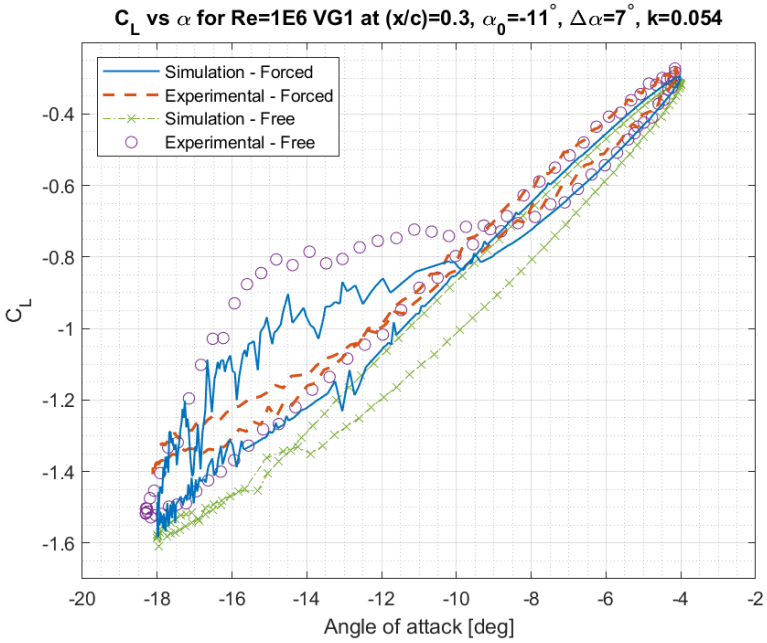

Figure 7.21: Effect of VG1 placed at $(x/c) = 0.3$ to the C_L vs α curve with forced transition and $\alpha_0 = -11°$,$\Delta\alpha = 7°$,and $\kappa = 0.054$

Finally, the results would suggest that the model works for both the negative angles and forced transition. In order to confirm, the hysteresis loop for lift is plotted in Figure 7.21. The experimental data shows a decrease in VG effectiveness with a forced transition at the leading edge. The double-wake simulation results for the positive angles show a marginal decrease in lift slope relative to the one found in the clean validation; however, this effect is more pronounced at the more negative angles. The experimental data for an airfoil with a forced transition suggests a reduced effect of stall near the extreme angles. Contrary to this, the simulation shows a significant drop in VG effectiveness, reducing the $C_{L_{\max}}$ and resulting in a partial flow separation. This corresponds well with the previous

results for forced transition cases, where the drop in VG effectiveness resulted from the increased distance from the VG to the transition point. While the VG module captures this reduced effectiveness, the double-wake model struggles to predict increased proclivity for flow attachment, leading to a disparity in the results. However, these results suggest an increased prediction accuracy of VG-induced mixing with a leading edge forced transition.

7.3. MODEL PERFORMANCE

One can summarize the performance of the VG implementation on the double-wake vortex-panel model by examining its adherence to the critical objectives. The general goal of this work was to achieve a working code that was able to take the complex flow interaction between vortex generators and the boundary layer into account. While the model's most prominent benefit and intention are for the code to be useful in an engineering environment of novel airfoil design, the thesis focuses on the basic implementation. Creating an entire design tool is considered beyond the scope of the current research; instead, this thesis aims to showcase its future capabilities by justifying the applicability of its results in simple cases.

Looking at the widely used software of today, XFOIL is considered the baseline for accuracy, speed, and quality in basic airfoil simulation. The tool's versatility outweighs the limitations of the assumptions in the solution method. However, as knowledge in aerospace engineering has expanded, so have the applications of the technology evolved beyond simple airfoil simulation. Over the past years, there have been numerous attempts to update these methods to modern standards and with increasing complexity without sacrificing speed. Within wind energy, in particular, an enormous potential for research into new airfoil designs exists due to the different desired characteristics at optimal performance, such as structural capability. The inclusion of the vortex generator, as seen in VGFOIL[3], is thus a giant leap in expanding the realm of possibilities for airfoil design. The double-wake vortex-panel method idea, proposed by Katz[19], developed by Riziotis[16] and Voutsinas[21], and the current version of the code created by Zanon[1], is an attempt to improve the performance of the XFOIL solution method through better separated-flow calculation. While these methods showed good adherence to experimental results, combining them allows for considerably more complexity in simulation.

As the double-wake model better captures stall characteristics of airfoils at high angles of attack, the inclusion of VGs is beneficial to predict their effect better on the promotion of attachment and improvement of airfoil performance. The base model has been validated and applied with no significant modifications to the solution method. Thus no improvement can be expected for the cases of clean airfoils. However, there is a possibility to improve over VGFOIL, as both models can simulate airfoils with VGs in steady conditions. For the unsteady cases with VGs, the model can only be compared to experimental data and evaluated for the relative impact of the VGs on the lift.

The clean configuration validation showed a disparity in the overprediction of lift for the positive angles of attack, also present in the cases with vortex generators. However, it is clear from the results that the VGs impart a change in the flow that is consistent with

the experimental data and expected from the BL parameters. Figure 7.22 presents the magnitude of this change in the unsteady double-wake model results compared to the experimental data; the graph corrects for the error in the base model by presenting the lift coefficient as a ratio of the clean and VG cases. The curves show very similar behavior in the plot, and the validation consistently showed that despite any absolute errors seen in the graph, the impact of the VG relative to the base model was always in the right direction and often had the correct magnitude as well.

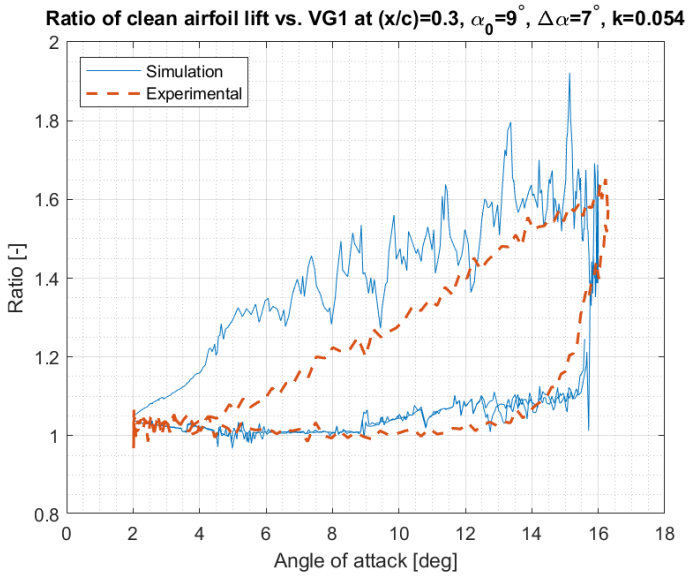

Figure 7.22: Highlighting the impact of adding VG1 as a ratio of lift

Besides the errors resulting from the double-wake model, a few issues remain in the current state of the code, which it inherited from the VG module. The shape of the hysteresis loops and the lift prediction accuracy, in general, are consistently a direct result of the ability to predict separation on the airfoil. In numerous cases where experimental data pointed towards a partial separation of the flow, the C_f spiked by the VG would remain positive for the entire chord, and separation would thus not occur. While this is a sign that the code works in general, the magnitude of this change was often much more extensive than expected. As the coefficient of friction is not an experimentally measurable variable, the validation cannot confirm the exact nature of the error. The flow remaining too strongly attached means a loss in detail and accuracy, especially in edge cases where separation only occurs briefly. The clearest example in the results occurred with forced transition, where the double-wake model fails to predict dynamic stall over the pitch-down motion, as shown in Figure 7.19.

While the model achieves positive indications across the board, several variables improve performance and limit cases in which the model behaves obscurely. VG design theory suggests that conventional vortex generators used to delay stall are most effective at some

point aft of transition. The mixing induced by the VG is highest immediately following the transition point, from which the magnitude scales down further aft in the chord. Although the validation results confirm this trend, the model achieves better parity to the experimental data when the VG-induced mixing is more negligible. The validation saw increased parity of the results with the VG placed at $(x/c) = 0.4$ and with a forced leading edge transition. This hypothesis is further corroborated by the increased accuracy of results from the VG2 configuration, with its lower $C_{L_{\max}}$, mirroring the data more closely. These trends indicate that the VG term is unbalanced while also agreeing with the conclusion of the preliminary validation, which showed better results with a lower Reynolds number.

8

CONCLUSION

As innovations in wind energy have been progressing at a record pace, experimental data and models of increasing complexity are relied upon more often for accurate simulations. With the average wind turbine blade increasing in length every year, the cyclical stresses caused by dynamic stall require experimentally-tested vortex generators to limit this phenomenon. This project aimed to create a low fidelity unsteady viscous-inviscid model capable of simulating dynamic stall, with the purpose of its prevention through the application of vortex generators. This model would facilitate airfoil design through earlier indications of VG performance in separation prevention. In order to build such a tool, existing viscous-inviscid models and their basis in physics were discussed in Chapter 2. While these models all share a similar basic formulation, with differences in assumptions and boundary conditions, the double-wake concept showed potential through its increased accuracy in simulating stalled conditions. An improved calculation over the separation region is crucial, as accurate results for a clean airfoil case could serve as a base for the VG to prevent it. For this, Chapter 3 investigates the applications of VGs, their designs, and the boundary layer changes that they impart on the flow. With the lifting force causing a vortex normal to the airfoil plane, consideration for other alternatives for simulation in a two-dimensional space follows. The optimal choice resides in the VGFOIL implementation, which utilizes an exponential mixing function to recreate the impact of the vortex.

The starting point of this project is the existing double-wake vortex-panel method developed by Alessandro Zanon[1], which had the original purpose of Vertical-Axis Wind Turbine simulation. The model was designed to simulate the flow over three moving and rotating airfoils and was created a decade ago, at the time of writing. This required changes in the inputs to the model and a rebuild of many functions to make them work with newer versions of MATLAB in the interest of long-term viability. While the model had been validated and used to collect results, the program's state was unknown; thus, a validation for the same case as detailed in the associated paper followed. The validation consisted of a NACA0015 in a steady case and an unsteady pitching motion undergoing

dynamic stall to confirm its separation prediction capabilities. First, the inviscid model showed consistency with the XFOIL data; seeing as XFOIL has been used widely and validated thoroughly, the validation confirms that the inviscid model is working correctly. Enabling the boundary layer and looking at the results for fully attached flow for $\alpha = 2$–$10°$, the results deviate from XFOIL slightly and show closer parity with the experimental data. A simplification in wake discretization causes a thicker BL, resulting in a lower C_L. In the double-wake model validation, the results vary considerably depending on the timestep chosen. The investigation into the reasons through an analysis of the associated variables led to a relation for choosing timestep based on inflow speed and average panel size. The double-wake model showed much better performance for predicting the drop-off in lift due to stall in the steady results, mirroring the experimental data almost perfectly. The unsteady results for the pitching case were able to capture the sharp drop in the lift at the maximum angle, proving the model's ability to capture dynamic stall. While a larger timestep gave more negligible scattering in the results, the timestep given by the relation followed the experimental data much closer.

The initial validation agreed with the original author's results and an ability to predict lift for stalled conditions in steady and unsteady NACA00015. With the essential function of the model validated, the thesis moves on to obtain a dataset that is useful for vortex generator implementation validation, finding it in a recently published experiment for a DU17DBD25 airfoil[4]. This experimental dataset contains force data for steady conditions and unsteady pitching cases with free and forced transition and varying VG parameters such as chordwise location and dimensions. With a new airfoil geometry, a second validation is performed to assess the baseline error of the model in simulating the airfoil in clean conditions. The negative slope on the top side of the airfoil is susceptible to a large pressure gradient, leading to significantly higher sensitivity to the separation position. Unnoticed in the initial validation, the higher sensitivity leads to more movement in the stall position, interfering with the unsteady lift calculation and increasing the noise in the results. A timestep sensitivity analysis repeats for this airfoil and its influence on the noise in the data; the resulting optimal choice of timestep agrees with the previously proposed relation. Several methods reduce the noise effectively —filtering, time-averaged lift, and scatter plotting— with the simplest practical method being the exclusion of data following a stall position change. The steady results agreed with the experimental data well, with underprediction in the near-stall region and overprediction in a deep stall. The results also show an improvement over XFOIL, indicating increased accuracy of the double-wake formulation. The unsteady results also show good agreement with the experimental data, capturing the phenomena sufficiently well. The double-wake model overpredicts the lift slope for the positive angles of attack, an error that reduces when the unsteadiness is smaller. For the negative angles of attack, the model could better predict the shape of the hysteresis loop, attributed to the more favorable flatter shape of the DU17DBD25 airfoil. With a forced transition, the data indicated stalled conditions for most of the motion, leading to a considerable drop in the airfoil's lift coefficient at high angles of attack, a phenomenon that the model struggled to capture.

As the double-wake base model was confirmed to function sufficiently accurately, the implementation of VGs in the program is discussed in Chapter 6. The method of simulating

VGs is taken from VGFOIL[3], where a semi-empirical formula derived from theory and statistical analysis describes the mixing induced by a VG at any BL location. The input variables consist of the VG height h^*_{VG}, VG length l^*_{VG}, VG angle of attack β_{VG}, and the flow velocity at the VG U_{VG}. The implementation of these formulas to the current code follows the changes made in VGFOIL. Transition is forced at the location of the VG if it does not happen earlier, the VG source-term is calculated once per iteration after transition, and the function is added to the equilibrium shear stress term $C_{\tau eq}$. In order to verify that the VG module works as intended, the model runs for a steady airfoil at $\alpha = 14°$. Whereas the base model predicts flow separation at $(x/c) = 0.5$, the inclusion of the VG increases the C_f and the flow remains attached. A reduction in the size of the VG reduces the jump in C_f, confirming correct behavior.

Understanding the errors resulting from the base double-wake model and verifying the correct implementation of the VG module from the original code, the model runs for a wide variety of VG cases. As this project aims to evaluate whether VGs added to a double-wake code can give insight into their effectiveness, the evaluation must disregard the errors of the base viscous-inviscid code. Isolating the VG module's performance requires the assessment method to compare the trends in simulation results from single parameter changes. Differences in results in the correct direction, despite the magnitude, prove the model can capture the phenomena, and further development in its implementation would lead to improvements in its simulation capabilities. For the steady results, a larger VG correctly increased the stall angle and maximum C_L; however, the magnitude was a significant overestimation. The model featured a later but sharper stall, indicating an error in the separation criterion affected by the VG. A decrease in VG dimensions resulted in better performance with an earlier stall and better agreement with experimental data, indicating an inconsistency between the VG dimensions and the separation criterion. For the unsteady results a reference simulation of $\alpha_0 = 9°, \Delta\alpha = 7, \kappa = 0.054$, with $VG1$ at $(x/c) = 0.3$, and free transition was chosen. The results showed fully attached flow for the entire pitching motion, avoiding the dynamic stall seen in the simulation without VGs, a trend identical to the experimental data. After correcting the results for the over-prediction seen in the base model, the relative impact of the VG gives high expectations for model performance. Testing the model for negative angles of attack shows similarly accurate results. Changes in the simulation to the VG size, chordwise location, free/forced transition, and pitching unsteadiness follow the same trends seen in the experimental data. While the general shape of the C_L vs. α curve is captured well in all cases, several variables influence the accuracy of the results. The double-wake model performed better in cases where the VG was located further away from transition, where the C_f had finished increasing naturally. The analysis of the results also found the opposite, where VG-induced transition would lead to phenomena such as separation and reattachment on the same pitching motion. This phenomenon proved to result from an error in the interaction between the VG and the transition point, which was subsequently corrected through an amendment to the VG module. While this amendment allowed the model to obtain results in cases where it previously couldn't, it resulted in the movement of the transition point, bringing the validity of the method into question. Nonetheless, the results adhere to the experimental data well, so the amendment is left in place.

The model performance is evaluated in Section 7.3, which discusses the strengths and limitations of the VG implementation to the double-wake model in detail. Overall, the model gives significantly accurate results to claim sufficient proof of concept. While the existing limitation of the double-wake vortex-panel method and the VG source-term modeling method remains, the model can be helpful in a preliminary evaluation of an airfoil's capability to prevent stall with VGs. The relative changes in the results from the inputs to the VG module also allow for limited analysis of desired VG location and initial sizing.

9

RECOMMENDATIONS FOR FUTURE RESEARCH

The results obtained in the previous chapter, with the complete code with vortex generators, show sufficient adherence to experimental data to claim the model's validity. Despite this, there are several identified limitations in implementing the model. While these errors are significant to the results presented in this paper, this chapter addresses the potential methods for reducing or avoiding them as a whole. Although the analysis of the results identified several errors, the model also makes assumptions that simplify physical boundary conditions. This project integrated two different ideas to achieve a double-wake panel method capable of simulating VGs; thus, the assumptions made in each of the precursor theories carry over to the current version of the code.

9.1. SOURCE-TERM CALIBRATION FOR THE CURRENT MODEL

The validation process found the VG mixing function's magnitude to be the largest source of error. Therefore, optimizing the VG source-term strength would significantly improve the results. The C_f data obtained from the simulations showed the influence of the VG preventing separation, even when the experimental data indicated a deep stall. Therefore, it is likely that the semi-empirically obtained VG source-term function is the origin of the errors concerning this phenomenon. The current model approaches the stall calculation directly, with a different vorticity distribution between the stall point and the trailing edge, substantially affecting the airfoil lift. However, the authors of VGFOIL calibrated the VG source-term on XFOIL, a model based on a single-wake boundary layer. This calibration aimed to minimize the error in steady maximum lift and the stall angle, both aspects being critically different in the double-wake model. Thus it is not surprising that a disparity exists in the separation behavior of the airfoil, as it is an aspect of the solution that is absent in the development of the VG relations. Fixing the problem requires reapplying the method presented by Tavernier et al. in their paper[3]. Repeating the calibration for

the current model would reduce the errors in the separation behavior.

9.2. QUASI-STEADY RELATION FOR VG MIXING BASED ON DYNAMIC INFLOW

While Zanon et al.[1] designed the base double-wake vortex-panel method to simulate VAWTs in unsteady flow, the viscous boundary layer remained steady as the inviscid solution captured the unsteadiness of the flow. Whereas Riziotis and Voutsinas[16] proposed an unsteady boundary layer, the author of the base double-wake model chose a quasi-steady boundary layer formulation seen in XFOIL[23]. While there are some potential drawbacks to having a steady formulation, it is beneficial for the sake of this program, as the VG module uses the same steady BL equations. Nonetheless, the vortex generators submerged in the boundary layer would experience the same unsteadiness as the airfoil. While the airfoil has a thickness and more complex geometry, the flat plate of a vortex generator has more room for simplification. Although the boundary layer is unsteady, it should be possible to achieve quasi-steadiness by applying Wagner's inflow function, discussed in more detail in Subsection 3.3.1. However, the goal would be to keep track of the changing velocity over the VG in the boundary layer and use dynamic inflow to capture the quasi-steady lift. As the mixing of the airfoil directly relates to the lift through the vorticity shed at the trailing edge, the quasi-steady relation can be used to adjust the magnitude of the VG source-term, which accounts for this mixing.

9.3. VG-INDUCED TRANSITION CRITERIA FOR BROADER APPLICABILITY

A critical measure of the lift prediction capabilities of the current model with VGs is the separation criterion. The cases in which the model gave the best results were when the VG would accurately influence the C_f. While the main error arises from the magnitude of this term, a reduction in VG dimensions resulted in increased accuracy. The model also presented difficulties in simulating a VG placed at $(x/c) = 0.2$, where the movement of the transition point could cause separation and reattachment on the same pitch-up or pitch-down motion. This phenomenon came primarily due to assumed forced transition at the VG location, limiting its impact on the boundary layer. A bypass transition criterion would ensure accurate results for a broader range of cases, especially with VG placement close to the leading edge. The original idea came from Kerho and Kramer[2], who included a relation for this criterion considering theoretical applications. However, as the current model assumes wind turbine applications, where VG height is proportional to the boundary layer, the necessity for such a term is limited. Nonetheless, future iterations of this model should include this criterion for increased versatility and broader applicability.

9.4. INCORRECT DRAG COEFFICIENT RESULTS

In the current thesis, the results have been discussed purely by considering the lift coefficient, with the drag being considered only for a small part of steady clean validation. As

the model stands, the values for tangential forces underestimate the total drag in both the base double-wake model and the result of the VG-induced mixing. Confidence in the accuracy of tangential forces is lower than those in the normal direction, leading to reduced dependence of these values to calculate airfoil performance. Thus, this also limits calculation of lift-over-drag ratios and airfoil efficiency. The accuracy of the model is therefore limited; however, the model can still be applied to domains where drag calculations can occur at a later stage in the design process. While wind turbine applications require high lift-over-drag ratio, an optimal lift coefficient guides the magnitude of this value, and parasitic drag from the VG is consistent for its shape. When necessary, higher fidelity simulations and experimental research estimate total drag. While the model is of sufficient quality as it stands, an improvement in the drag calculation would broaden the applicability of its method. While the validation did not evaluate the C_f thoroughly, the prediction of separation delay by the VG indicates that the relative values seem to be correct. Possible methods of improving this would be to find a statistical relationship to the expected error and adjust the drag values accordingly.

A

SWAFFORD'S VELOCITY PROFILE AT VG

$$U_{\mathrm{VG}} = \frac{u^+}{u_e^+} \cdot U_{edge} \tag{A.1}$$

$$u^+ = \frac{\mathrm{S}}{0.09} \cdot \tan^{-1}\left(0.09 \cdot y^+\right) + \left(u_e^+ - \frac{\mathrm{S}\pi}{0.18}\right) \tanh^{\frac{1}{2}}\left(a \cdot \left(\frac{H_{\mathrm{VG}}}{\theta_{\mathrm{VG}}}\right)^b\right) \tag{A.2}$$

$$a = \frac{\tanh^{-1}\left(g(2)^2\right)}{2^b} \tag{A.3}$$

$$b = \frac{\log\left(\frac{\tanh^{-1}(g(2)^2)}{\tanh^{-1}(g(5)^2)}\right)}{\log\left(\frac{2}{5}\right)} \tag{A.4}$$

$$g(2) = \frac{\frac{u}{u_e}(2) - \frac{\mathrm{S}}{0.09 * u_e^+} \cdot \tan^{-1}\left(\frac{0.18 \cdot \mathrm{Re}_{\theta_{\mathrm{VG}}}}{u_e^+}\right)}{1 - \frac{\mathrm{S}\pi}{0.18 u_e^+}} \tag{A.5}$$

$$g(5) = \frac{\frac{u}{u_e}(5) - \frac{\mathrm{S}}{0.09 * u_e^+} \cdot \tan^{-1}\left(\frac{0.45 \cdot \mathrm{Re}_{\theta_{\mathrm{VG}}}}{u_e^+}\right)}{1 - \frac{\mathrm{S}\pi}{0.18 u_e^+}} \tag{A.6}$$

$$\frac{u}{u_e}(2) = \frac{\tanh^{-1}\left(\frac{8.5 - H_{\mathrm{VG}}}{7.5} - 0.364\right)}{1.95} \tag{A.7}$$

$$\frac{u}{u_e}(5) = 0.155 + \frac{0.795}{0.51 \cdot (H_{\mathrm{VG}} - 1.95)} \tag{A.8}$$

$$\mathrm{S} = \frac{C_f}{|C_f|} \tag{A.9}$$

$$u_e^+ = \left(\frac{2}{|C_f|}\right)^{0.5} \tag{A.10}$$

$$C_f = \left(\frac{0.3 \cdot e^{-1.33H}}{\log_{10}\left(\mathrm{Re}_{\theta_{\mathrm{VG}}}\right)^{1.74+0.31H}} + 0.00011 \cdot \left(\tanh\left(4 - \frac{H}{0.875}\right) - 1\right)\right) \tag{A.11}$$

NOMENCLATURE

Acronyms

BL	Boundary Layer
CFD	Computational Fluid Dynamic
DNS	Direct Numerical Simulation
LES	Large Eddy Simulation
LTT	Low turbulence tunnel
VG(s)	Vortex generator(s)
VG1/VG2	First and second VG configuration
VII	Viscous-Inviscid Interaction

Greek Symbols

α	angle of attack
α_0	mean angle of attack for unsteady pitching
α_S	angle of attack at which the airfoil stalls
δ	boundary layer thickness -
$\Delta\alpha$	amplitude of unsteady pitching
δ^*	displacement thickness - $\int_0^\delta \left(1-\left(\rho u/\rho_e u_e\right)\right) \mathrm{d}\eta$
δ^{**}	density thickness - $\int_0^\delta \left(u/u_e\right)\left(1-\left(\rho/\rho_e\right)\right) \mathrm{d}\eta$
Γ	Circulation
γ	strength of the vorticity panel
κ or k	reduced frequency - $\Omega c/\left(2U_\infty\right)$
λ_{VG}	decay rate of VG exponential term

τ	tangent unit vector
μ	dynamic viscosity
ν	kinematic viscosity
Ω	angular velocity
ω	vorticity
ρ	air density
σ	strength of a source panel
$\sigma_{0_{VG}}$	magnitude of VG exponential term
Θ	potential of the flow
θ	momentum thickness - $\int_0^\delta \left(\rho u/\rho_e u_e\right)\left(1-(u/u_e)\right)\mathrm{d}\eta$
θ^*	kinetic energy thickness - $\int_0^\delta \left(\rho u/\rho_e u_e\right)\left(1-\left(u^2/u_e^2\right)\right)\mathrm{d}\eta$
Θ_n	momentum transport in the normal direction - $1/\left(\rho_e u_e^2\right)\int_0^\delta \left(\rho_e u_e v_e - \rho u v\right)\mathrm{d}\eta$

Roman Symbols

β_{VG}	vortex generator angle of attack
c	chord length
C_D	dissipation coefficient - $1/\left(\rho_e u_e^3\right)\int_0^\delta \tau(\partial u/\partial\eta)\mathrm{d}\eta$
C_D	drag coefficient
C_f	skin friction coefficient - $2\tau_{\text{wall}}/\left(\rho_e u_e^2\right)$
C_L	lift coefficient
C_P	pressure coefficient
$C_{\tau_{\text{EQ}}}$	equilibrium shear stress coefficient
C_τ	shear stress coefficient - $\tau_{\max}/\left(\rho_e u_e^2\right)$
dt	timestep (in simulation)
H	shape parameter - δ^*/θ
h	height of an object

H^* kinetic energy shape parameter - θ^*/θ

h^*_{crit} critical roughness height

h^*_{VG} height of a vortex generator normalized to chord length

H^{**} density shape parameter - δ^{**}/θ

H_k kinematic shape parameter - $\int [1-(u/u_e)]\, d\eta / \int (u/u_e)\,[1-(u/u_e)]\, d\eta$

l/L length of an object

l^*_{VG} length of a vortex generator normalized to chord length

n normal unit vector

N_p Number of panels on the airfoil surface

N_v Number of vortex blobs

q velocity in the absolute frame of reference

t time

tV/c timestep normalized by inflow velocity to chord lengths per second

u/U tangential velocity in the boundary layer

w/W normal velocity in the boundary layer

$w_{transp.}$ transpiration velocity

x/c x-coordinate normalized to a unit chord length

Ma Mach Number

Re Reynolds number

Re_θ momentum thickness Reynolds number

Subscripts

$+,-$ upper and lower sides of the airfoil

1 refers to the attached part of the flow

2 refers to the separated part of the flow

τ denotes the tangential component of a vector

θ	coordinates in angular reference frame
B	refers to the body of the airfoil
e	edge of the boundary layer
f	refers to the 'Equivalent inviscid flow'
i	refers to the i-th panel on the airfoil surface
n	denotes the normal component of a vector
p	potential flow
s	refers to the wake at the separation point
w	refers to the wake at the trailing edge
max	maximum value of a variable
min	minimum value of a variable
sp	position of separation point
VG	refers to a property of a vortex generator

BIBLIOGRAPHY

[1] A. Zanon, P. Giannattasio, and C. Ferreira. "A vortex panel model for the simulation of the wake flow past a vertical axis wind turbine in dynamic stall". In: *Wind Energy* 16 (2013), pp. 661–680.

[2] M. Kerho and B. Kramer. "Enhanced Airfoil Design Incorporating Boundary Layer Mixing Devices". In: 2003.

[3] D. de Tavernier, D. Baldacchino, and C. Ferreira. "An integral boundary layer engineering model for vortex generators implemented in XFOIL". In: *Wind Energy* 21 (2018), pp. 906–921.

[4] D. D. Tavernier et al. "Controlling dynamic stall using vortex generators on a wind turbine airfoil". In: *Renewable Energy* 172 (2021), pp. 1194–1211.

[5] T. Burton et al. "Wind Energy Handbook". In: 2001.

[6] Brian Ohrbeck Hansen, M. Courtney, and N. Mortensen. "Wind Resource Assessment – Østerild National Test Centre for Large Wind Turbines". In: 2014.

[7] A. Peña et al. "Ten Years of Boundary-Layer and Wind-Power Meteorology at Høvsøre, Denmark". In: *Boundary-Layer Meteorology* 158 (2015), pp. 1–26.

[8] H.D. Taylor. *The elimination of diffuser separation by vortex generators*. Technical Report. United Aircraft Corporation, June 1947.

[9] J. Leishman. "Challenges in modelling the unsteady aerodynamics of wind turbines". In: *Wind Energy* 5 (2002), pp. 85–132.

[10] L. Carr. "Progress in analysis and prediction of dynamic stall". In: *Journal of Aircraft* 25 (1988), pp. 6–17.

[11] M. Kramer. "Increase in the maximum lift of an airplane wing due to a sudden increase in its effective angle of attack resulting from a gust". In: 1932.

[12] L. Carr, K. Mcalister, and W. J. Mccroskey. "Analysis of the development of dynamic stall based on oscillating airfoil experiments". In: 1977.

[13] D. Shipley et al. "Evidence that aerodynamic effects, including dynamic stall, dictate HAWT structural loads and power generation in highly transient time frames". In: 1994.

[14] A. Choudhry et al. "Effects of Wake Interaction on Downstream Wind Turbines". In: *Wind Engineering* 38 (2014), pp. 535–547.

[15] J. Katz and A. Plotkin. "Low-Speed Aerodynamics". In: 1991.

[16] V. Riziotis and S. Voutsinas. "Dynamic stall modelling on airfoils based on strong viscous inviscid interaction coupling". In: *International Journal for Numerical Methods in Fluids* 56 (2008), pp. 185–208.

[17] B. Basu and G. J. Hancock. “The unsteady motion of a two-dimensional aerofoil in incompressible inviscid flow”. In: *Journal of Fluid Mechanics* 87 (1978), pp. 159–178.

[18] T. Sarpkaya. “An inviscid model of two-dimensional vortex shedding for transient and asymptotically steady separated flow over an inclined plate”. In: *Journal of Fluid Mechanics* 68 (1975), pp. 109–128.

[19] J. Katz. “A discrete vortex method for the non-steady separated flow over an airfoil”. In: *Journal of Fluid Mechanics* 102 (1981), pp. 315–328.

[20] M. Vezza and R. Galbraith. “An inviscid model of unsteady aerofoil flow with fixed upper surface separation”. In: *International Journal for Numerical Methods in Fluids* 5 (1985), pp. 577–592.

[21] S. Voutsinas and V. Riziotis. “A viscous-inviscid interaction model for dynamic stall simulations on airfoils”. In: 1999.

[22] L. Marion, Néstor Ramos-García, and J. Sørensen. “Inviscid double wake model for stalled airfoils”. In: 2014.

[23] M. Drela and M. Giles. “Viscous-inviscid analysis of transonic and low Reynolds number airfoils”. In: *AIAA Journal* 25 (1987), pp. 1347–1355.

[24] B. Thwaites. “Approximate Calculation of the Laminar Boundary Layer”. In: *Aeronautical Quarterly* (1949). DOI: doi:10.1017/S0001925900000184.

[25] M. Drela. “XFOIL: An Analysis and Design System for Low Reynolds Number Airfoils”. In: 1989.

[26] M. Drela. “Two-dimensional transonic aerodynamic design and analysis using the Euler equations”. In: 1986.

[27] T. Swafford. “Analytical Approximation of Two-Dimensional Separated Turbulent Boundary-Layer Velocity Profiles”. In: *AIAA Journal* 21 (1983), pp. 923–926.

[28] J. Green, David J. Weeks, and J. W. F. Brooman. “Prediction of turbulent boundary layers and wakes in compressible flow by a lag-entrainment method”. In: 1973.

[29] R.P.J.O.M. Van Rooij. *Modification of the boundary layer calculation in RFOIL for improved airfoil stall prediction*. Sept. 1996.

[30] W. Sheng, R. Galbraith, and F. Coton. “Return from airfoil stall during ramp-down pitching motions”. In: *Journal of Aircraft* 44 (2007), pp. 1856–1864.

[31] J. L. Ingen. “A suggested semi-empirical method for the calculation of the boundary layer transition region”. In: 1956.

[32] T. Cebeci. “Stability and Transition: Theory and Application”. In: 2004.

[33] P. S. Klebanoff, W. G. Cleveland, and K. Tidstrom. “ON THE EVOLUTION OF A TURBULENT BOUNDARY LAYER INDUCED BY A THREE-DIMENSIONAL ROUGHNESS ELEMENT”. In: *Journal of Fluid Mechanics* 237 (1992), pp. 101–187.

[34] F. Ergin and E. B. White. “Unsteady and Transitional Flows Behind Roughness Elements”. In: *AIAA Journal* 44 (2006), pp. 2504–2514.

[35] N. Rott. “Unsteady viscous flow in the vicinity of a stagnation point”. In: *Quarterly of Applied Mathematics* 13 (1956), pp. 444–451.

[36] W. R. Sears. “Some Recent Developments in Airfoil Theory”. In: *Journal of the Aeronautical Sciences* 23 (1956), pp. 490–499.

[37] F. Moore. “On the separation of the unsteady laminar boundary layer”. In: 1958.

[38] Mohamed Gad-el-Hak. “Separation Control”. In: *Flow Control: Passive, Active, and Reactive Flow Management*. Cambridge University Press, 2000, pp. 150–188. DOI: 10.1017/CBO9780511529535.010.

[39] R. A. Despard and J. A. Miller. “Separation in oscillating laminar boundary-layer flows”. In: *Journal of Fluid Mechanics* 47.1 (1971), pp. 21–31. DOI: 10.1017/S0022112071000909.

[40] M. Lighthill. “On displacement thickness”. In: *Journal of Fluid Mechanics* 4 (1958), pp. 383–392.

[41] S. Goldstein. “ON LAMINAR BOUNDARY-LAYER FLOW NEAR A POSITION OF SEPARATION”. In: *Quarterly Journal of Mechanics and Applied Mathematics* 1 (1948), pp. 43–69.

[42] Ludwig Prandtl. “Über Flüssigkeitsbewegung bei sehr kleiner Reibung”. In: (1904), pp. 484–491.

[43] J. Ackeret, A. Betz, and O. Schrenk. “Experiments with an airfoil from which the boundary layer is removed by suction”. In.

[44] M. Amitay et al. “Aerodynamic Flow Control over an Unconventional Airfoil Using Synthetic Jet Actuators”. In: *AIAA Journal* 39 (2001), pp. 361–370.

[45] A. L. Pape et al. “Dynamic Stall Control Using Deployable Leading-Edge Vortex Generators”. In: *AIAA Journal* 50 (2011), pp. 2135–2145.

[46] L. Maestrello and L. Ting. “Analysis of active control by surface heating”. In: *AIAA Journal* 22 (1984), pp. 1038–1045.

[47] G. B. Schubauer and W. G. Spangenberg. “Forced mixing in boundary layers”. In: *Journal of Fluid Mechanics* 8 (1960), pp. 10–32.

[48] H. H. Pearcey. “INTRODUCTION TO SHOCK-INDUCED SEPARATION AND ITS PREVENTION BY DESIGN AND BOUNDARY LAYER CONTROL”. In: 1961.

[49] G. Godard and M. Stanislas. “Control of a decelerating boundary layer. Part 1: Optimization of passive vortex generators”. In: *Aerospace Science and Technology* 10 (2006), pp. 181–191.

[50] J. Lin et al. “Separation control on high-lift airfoils via micro-vortex generators”. In: *Journal of Aircraft* 31 (1994), pp. 1317–1323.

[51] J. Lin. “Review of research on low-profile vortex generators to control boundary-layer separation”. In: *Progress in Aerospace Sciences* 38 (2002), pp. 389–420.

[52] W. Pauley and J. Eaton. “Experimental study of the development of longitudinal vortex pairs embedded in a turbulent boundary layer”. In: *AIAA Journal* 26 (1987), pp. 816–823.

[53] D. Baldacchino. “Vortex Generators for Flow Separation Control: Wind Turbine Applications”. In: 2019.

[54] M. Drela. “Flight Vehicle Aerodynamics”. In: 2014.

[55] M. Bragg and G. Gregorek. “Experimental Study of Airfoil Performance with Vortex Generators”. In: *Journal of Aircraft* 24 (1987), pp. 305–309.

[56] J. Lin, F. G. Howard, and G. Selby. “Exploratory study of vortex-generating devices for turbulent flow separation control”. In: 1991.

[57] M. Kerho et al. “Vortex generators used to control laminar separation bubbles”. In: *Journal of Aircraft* 30 (1993), pp. 315–319.

[58] L. Jenkins, S. Gorton, and S. Anders. “FLOW CONTROL DEVICE EVALUATION FOR AN INTERNAL FLOW WITH AN ADVERSE PRESSURE GRADIENT”. In: 2002.

[59] L. Carr and K. Mcalister. “The effect of a leading-edge slat on the dynamic stall of an oscillating airfoil”. In: 1983.

[60] A. Choudhry, M. Arjomandi, and Richard M. Kelso. “Methods to control dynamic stall for wind turbine applications”. In: *Renewable Energy* 86 (2016), pp. 26–37.

[61] H. Mai et al. “Dynamic stall control by leading edge vortex generators”. In: *Journal of The American Helicopter Society* 53 (2006), p. 26.

[62] J. Jones. “The Calculation of the Paths of Vortices from a System of Vortex Generators, and a Comparison with Experiment”. In: 1955.

[63] D. G. Gould. “The use of vortex generators to delay boundary layer separation: theoretical discussion supported by tests on a CF-100 aircraft”. In: *National Aeronautical Establishment (Canada)* 86 (1956), pp. 26–37.

[64] B. J. Wendt and Tom J. Biesiadny. “Initial Circulation and Peak Vorticity Behavior of Vortices Shed From Airfoil Vortex Generators”. In: 2001.

[65] B. J. Wendt and B. A. Reichert. “The modelling of symmetric airfoil vortex generators”. In: 1996.

[66] J. C. Dudek. “An Empirical Model for Vane-Type Vortex Generators in a Navier-Stokes Code”. In: 2013.

[67] D. J. Poole et al. “An Aerodynamic Model for Vane-Type Vortex Generators”. In: 2016.

[68] H. Glauert. *The elements of aerofoil and airscrew theory*. Cambridge University Press, 1983.

[69] E. Polhamus. “Application of the leading-edge-suction analogy of vortex lift to the drag due to lift of sharp-edge delta wings”. In: 1968.

[70] M. Hansen et al. “Validation of a Model for Estimating the Strength of a Vortex Created from the Bound Circulation of a Vortex Generator”. In: *Energies* 12 (2019), p. 2781.

[71] R. Westphal, J. Eaton, and W. Pauley. “Interaction Between a Vortex and a Turbulent Boundary Layer in a Streamwise Pressure Gradient”. In: 1987.

[72] Bruce J. Wendt, B. A. Reichert, and J. D. Foster. “The decay of longitudinal vortices shed from airfoil vortex generators”. In: 1995.

[73] P. Ashill, J. Fulker, and K. Hackett. “A review of recent developments in flow control”. In: *Aeronautical Journal* 109 (2005), pp. 205–232.

[74] Ola Lögdberg, J. Fransson, and P. Alfredsson. “Streamwise evolution of longitudinal vortices in a turbulent boundary layer”. In: *Journal of Fluid Mechanics* 623 (2009), pp. 27–58.

[75] M. Manolesos and S. Voutsinas. “Experimental investigation of the flow past passive vortex generators on an airfoil experiencing three-dimensional separation”. In: *Journal of Wind Engineering and Industrial Aerodynamics* 142 (2015), pp. 130–148.

[76] L. Ericsson and J. Reding. “Fluid mechanics of dynamic stall part I. Unsteady flow concepts”. In: *Journal of Fluids and Structures* 2 (1988), pp. 1–33.

[77] L. Ericsson and J. Reding. “Fluid mechanics of dynamic stall part II. Prediction of full scale characteristics”. In: *Journal of Fluids and Structures* 2 (1988), pp. 113–143.

[78] Herbert Wagner. “About the origin of the dynamic lift of wings”. In: *ZAMM - Journal of Applied Mathematics and Mechanics / Journal for Applied Mathematics and Mechanics* 5.1 (1925), pp. 17–35. DOI: https://doi.org/10.1002/zamm.19250050103. eprint: https://onlinelibrary.wiley.com/doi/pdf/10.1002/zamm.19250050103. URL: https://onlinelibrary.wiley.com/doi/abs/10.1002/zamm.19250050103.

[79] Chengyong Zhu et al. “Dynamic stall control of the wind turbine airfoil via single-row and double-row passive vortex generators”. In: *Energy* 189 (2019), p. 116272.

[80] Erich E Bender, Bernard H Anderson, and Patrick J Yagle. “Vortex generator modeling for Navier-Stokes codes”. In: *American Soc. of Mechanical Engineers FEDSM99-6929 New York* (1999).

[81] A. Jirásek. “Vortex-Generator Model and Its Application to Flow Control”. In: *Journal of Aircraft* 42 (2004), pp. 1486–1491.

[82] Adam Jirasek. *A modified vortex generator model and its application to complex aerodynamic flows*. Division of Aeronautics, FFA, FOI-Swedish Defence Research Agency, 2004.

[83] Olle Törnblom and A. Johansson. “A Reynolds stress closure description of separation control with vortex generators in a plane asymmetric diffuser”. In: *Physics of Fluids* 19 (2007), p. 115108.

[84] E. Daniele et al. “An extension of a strong viscous–inviscid coupling method for modeling the effects of vortex generators”. In: *Wind Engineering* 43 (2019), pp. 175–189.

[85] H. Shan et al. “Numerical study of passive and active flow separation control over a NACA0012 airfoil”. In: *Computers Fluids* 37 (2008), pp. 975–992.

[86] R. Galbraith et al. “Collected Data for Tests on NACA 0015 Aerofoil with Chord of Length 0.275m. G.U. Aero Report 9209”. In: 1992.

[87] *Low turbulence tunnel*. URL: https://www.tudelft.nl/lr/organisatie/afdelingen/aerodynamics-wind-energy-flight-performance-and-propulsion/facilities/low-speed-wind-tunnels/low-turbulence-tunnel.

[88] Daniel Baldacchino et al. “Experimental parameter study for passive vortex generators on a 30% thick airfoil”. In: *Wind Energy* 21.9 (2018), pp. 745–765. DOI: https://doi.org/10.1002/we.2191.

[89] M. Drela. “Integral boundary layer formulation for blunt trailing edges”. In: 1989.